

The spring phytoplankton bloom and vertical velocities in the stratified and
deep convecting Labrador Sea, as observed by Seagliders

Eleanor Frajka-Williams

A dissertation submitted in partial fulfillment of
the requirements for the degree of

Doctor of Philosophy

University of Washington

2009

Program Authorized to Offer Degree: Department of Oceanography

University of Washington
Graduate School

This is to certify that I have examined this copy of a doctoral dissertation by

Eleanor Frajka-Williams

and have found that it is complete and satisfactory in all respects,
and that any and all revisions required by the final
examining committee have been made.

Chair of the Supervisory Committee:

Peter Rhines

Reading Committee:

Peter Rhines

Eric D'Asaro

Charles Eriksen

Date:

In presenting this dissertation in partial fulfillment of the requirements for the Doctoral degree at the University of Washington, I agree that the Library shall make its copies freely available for inspection. I further agree that extensive copying of this dissertation is allowable only for scholarly purposes, consistent with "fair use" as prescribed in the U.S. Copyright Law. Requests for copying or reproduction of this dissertation may be referred to ProQuest Information Learning, 300 North Zeeb Road, Ann Arbor, MI 48106-1346, 1-800-521-0600, to whom the author has granted "the right to reproduce and sell (a) copies of the manuscript in microform and/or (b) printed copies of the manuscript made from microform."

Signature_____

Date_____

University of Washington

Abstract

The spring phytoplankton bloom and vertical velocities in the stratified and deep convecting Labrador Sea, as observed by Seagliders

by Eleanor Frajka-Williams

Chair of the Supervisory Committee:

Professor Peter Rhines
Departments of Oceanography and Atmospheric Sciences

The Labrador Sea is a critical region in the world's ocean: a region where the effects of climate change are seen quickly and strikingly, and where dynamic processes that affect climate change are observed. A recent effect of climate change is the increase of freshwater to high latitudes, as Arctic pack ice and Greenland glaciers melt at accelerating rates. In times of rapid climate change, it is more important than ever to understand the influence these changes have on the status quo of ecosystems and physical processes. The focus of this thesis is to examine the current state of the Labrador Sea biological and physical system through *in situ* Seaglider and surface satellite observations. The influence of physical processes, including increased freshwater runoff, on the biological system is the subject of chapters 2 and 3. The deep convective process, one of the downwelling branches of the global oceanic overturning circulation is the subject of chapters 4 and 5. Seaglider is capable of making novel measurements of vertical water velocity to better than 1 cm s^{-1} accuracy. Using these measurements along with hydrographic observations, we describe deep convection during the 2004-05 winter. Besides the scientific merits of the results shown here, this thesis also demonstrates the ability of Seaglider to observe bio-optical properties and vertical velocities, two relatively newer observations in the oceanography literature.

TABLE OF CONTENTS

List of Figures	iii
Chapter 1: Introduction	1
Chapter 2: Physical controls and mesoscale variability in the Labrador Sea spring phytoplankton bloom observed by Seaglider	3
2.1 Introduction	3
2.2 Data sources & processing	5
2.3 Basin-scale hydrography and productivity	10
2.4 Mesoscale biological and physical features	12
2.5 Conclusion	18
2.6 Figures	20
Chapter 3: Physical controls on the interannual variability of the Labrador Sea spring phytoplankton bloom using Sea-viewing Wide Field of view Sensor (SeaWiFS)	35
3.1 Summary	35
3.2 Introduction	35
3.3 Data	38
3.4 Methods & Results: Climatology of the Bloom	39
3.5 Methods & Results: Interannual Variability	43
3.6 Conclusions	47
3.7 Figures	50
Chapter 4: Determining vertical water velocities from Seaglider	59

4.1	Introduction	59
4.2	Glider flight model	60
4.3	Flight parameters	62
4.4	Sensitivity of w to parameters	63
4.5	Optimization	65
4.6	Results	68
4.7	Discussion	69
4.8	Figures	71
Chapter 5:	Vertical velocities in the stratified and deep convecting Labrador Sea from Seaglider, 2004-05	83
5.1	Introduction	83
5.2	Data and Processing	85
5.3	Interannual trends in convection, 2003-2008	88
5.4	Glider Observations, 2004-05	91
5.5	Vertical velocities measured by Seaglider	95
5.6	Conclusions	105
5.7	Figures	106
Chapter 6:	Conclusions	129

LIST OF FIGURES

2.1	Map of glider track and mean eddy kinetic energy, salinity and velocities from climatology.	21
2.2	Calibration figure for Seaglider oxygen, compared to shipboard oxygen from an AR7W cruise	22
2.3	Scatterplots of seaglider fluorescence vs. bloom intensity for different regions . . .	23
2.4	Fluorescence quenching observed by seaglider, displayed as a ratio between fluorescence and backscatter	24
2.5	SeaWiFs surface chlorophyll compared to glider-estimated chlorophyll: maps and annual cycles	25
2.6	Entire record of seaglider hydrography, fluorescence and time series of bloom intensity	26
2.7	Auto-correlations between seaglider measurements of mixed-layer hydrographic and biological properties	27
2.8	Annual cycle of dissolved oxygen at 40 m, from two gliders	28
2.9	Spatial map of glider observations of 4 fresh lenses and surface velocities	29
2.10	Swaths of seaglider hydrography, oxygen and fluorescence in the north bloom region	30
2.11	Vertical profiles of Seaglider hydrography and bio-optical properties in the four productive regions	31
2.12	Mean vertical profiles of salinity and fluorescence in and at the edges of fresh lenses	32
2.13	Buoyancy anomaly to 250 m for the north bloom and central Labrador Sea bloom regions	32
2.14	Waterfall plot of fluorescence in thin layers on isopycnal coordinates	33
2.15	Salinity and fluorescence at the Labrador shelf-break front	34

3.1	Map of domain bathymetry and climatological eddy-kinetic-energy, surface salinities and mean currents	50
3.2	Bloom magnitude and phase from SeaWiFS 1998-2007	51
3.3	Annual cycle of SeaWiFS chlorophyll in the north and central Labrador Sea regions	52
3.4	Predicted bloom start day (phase) in the Labrador Sea using Sverdrup's critical depth theory, climatological mixed layer depths and PAR	53
3.5	Maps of May buoyancy anomaly to 500 m from World Ocean Atlas 2005	53
3.6	Maps of the April-May spring bloom, for each year 1998-2008 from SeaWiFS . . .	54
3.7	Homogenous correlation maps of the first two EOFs of SeaWiFS chlorophyll, 1998-2008	55
3.8	Map of regions used to create annual indices of the bloom and physical processes .	55
3.9	Interannual cycles of the bloom in the north and central Labrador Sea regions . . .	56
3.10	Annual indices of the bloom and physical processes in the north region	57
3.11	Linear regressions between the bloom and physical indices	58
3.1	Correlation coefficients between bloom and physical indices for the north and central Labrador Sea	58
4.1	Flow chart of Seaglider data processing	72
4.2	Effect of roll maneuvers on vertical velocity estimates	73
4.3	Regressing for lift and drag over the first 50 dives, then for abs-compress and vbd-bias for dives 1-663.	74
4.4	Effect of each flight parameter on individual vertical velocity profiles	75
4.5	Diagram of force balance on the Seaglider, during a dive (a) and during a climb (b). Forces are lift (L), drag (D), and buoyancy (B). The glider velocity is U and W in the x - and z -directions, and θ is the glide angle.	75
4.6	Choice of minimization, tested for cycles 241-340, sg014.	76
4.7	Gridding vs binning data to create mean profiles.	77
4.8	Offset between ensemble means of dive and climb vertical velocity profiles for the entire mission	78

4.9	WKB-scaling of w_{rms} in the stratified ocean, sg015	79
4.10	Scatterplots of sg015 w_{rms} on heat flux (a) and wind speed (b) for lagged daily averages.	79
4.11	Frequency spectrum and buoyancy frequency, sg014	80
4.12	Stability of pitch relationship to pitch control, for sg014 and sg015	81
4.13	Effect of pitch correction procedure on mean profiles of vertical velocity, tested on sg014 and sg015	82
5.1	Map of gliders sg014 and sg015 tracks, heat fluxes and convection resistance . . .	107
5.2	Argo-Seaglider hydrography comparison	108
5.3	Cumulative heat content from NCEP, 2002-2008. 2002-2007 was restratifying, until 2008 when cooling was particularly intense.	109
5.4	Evolution of LSW from 2003-2008, from Argo profiles	109
5.5	Maximum pycnostad thickness in the convection region in April, 2003-2008, from Argo	110
5.6	Salinity, temperature, potential density and vertical velocity for sg014	111
5.7	Salinity, temperature, potential density and vertical velocity for sg015	112
5.8	Profiles of potential temperature (a) and salinity (b) during deep convection, sg015 and sg014	113
5.9	Waterfall plot of salinity, temperature and vertical velocity during convection, sg015	114
5.10	Waterfall plot of potential temperature, salinity and vertical velocity during convection, sg014	115
5.11	Heat content from sg014 and sg015, and Argo float 4900611	116
5.12	RMS-vertical velocity and decorrelation length scales for sg014	117
5.13	Lag autocorrelation of vertical velocity profiles from the stratified and unstratified regions, sg014	118
5.14	GM76 vertical velocity spectrum in wavenumber-frequency space	119
5.15	Vertical velocity spectra and N histogram from sg014	120
5.16	Salinity time series and velocity spectra from the K1 mooring	121

5.17	WKB-scaling of w_{rms} in the stratified ocean, sg015	122
5.18	WKB-scaling of w_{rms} in the stratified ocean, sg015	122
5.19	Mean profile, variance and skewness during convection, sg014.	123
5.20	Scales and magnitudes of vertical velocities in the surface mixed layer, from sg015	124
5.21	Lag correlation between w_{rms} and heat flux (dotted line) and winds (solid line) for sg015, January 1-February 20, 2005 (51 days). Peaks were found for a lag of about 0.6 days (heat flux) and 0.7 days (winds). Correlation coefficients are above 0.5. . .	125
5.22	Scatterplots of sg015 w_{rms} on heat flux (a) and wind speed (b) for time series lagged by 0.6 days (a) and 0.7 days (b).	125
5.23	Buoyancy frequency (a), WKB-scaled vertical velocities (b) and wind speed (c) for the entire mission, top 500 m, sg015.	126
5.24	Mean profiles of velocity variance and buoyancy frequency, aligned by mixed layer depth, sg015	126
5.25	Average profiles of (a) salinity, (b) potential temperature, (c) N^2 and (d) vertical velocity during active convection in the Labrador Sea (gray) and inside the Irminger Ring (black), sg015.	127
5.26	WKB scaling of vertical velocity during convection and the stratified eddy, sg015 .	128

ACKNOWLEDGMENTS

I would like to thank all the members of my committee—without the separate support and input from Eric D’Asaro, Ramsey Harcourt, Charlie Eriksen, Eric Kunze, and most especially my advisor Peter Rhines—this work would not have come together as successfully. Many thanks to Peter for his support, limitless ideas and continuous enthusiasm, and encouraging me to work on many aspects of this data set.

Thanks to Luanne Thompson, Susan Lozier, Victoria Coles, and Kate Duttro, who have been able to advise me on life as a scientist. Thanks to Kathie Kelly, Tom Sanford, and Bruce Frost, whose excellent courses have influenced the shape of this thesis. Thanks also to Jonathan Lilly, Sunke Schmidt, Paul Myers, Brandon Sackmann, Bill Fredericks, Cecilia Perralta-Ferriz, Eric Rehm, Amanda Gray, Jesse Anderson, Nick Beard, Kim Martini, Beth Curry, Annie Wong and Sally Warner.

Financial support for Eleanor during this work was provided by National Defense Science and Engineering Graduate Fellowship (NDSEG) and National Science Foundation (NSF) graduate research fellowships.

Above all, I thank my husband Tamás for his tireless support, patience and understanding, and my daughter Emese for the perspective she has given me, and the many hugs at the end of each day.

Chapter 1

INTRODUCTION

The Labrador Sea is a complex and unique region in the world. It is one of 3 sites of deep convection in the North Atlantic, the other two being the Mediterranean and Greenland-Iceland-Norwegian (GIN) Seas. Deep convection is a potential driver of the meridional overturning circulation (MOC), the primary overturning circulation in the Atlantic, and an important element of the climate system. The process of deep convection is spatially and temporally inhomogenous, with strong interannual variability and results from extreme surface buoyancy forcing during winter storms over the North Atlantic. As a result, it is difficult to observe, and the dynamics controlling deep convection are not well-understood. The Labrador Sea is also a region which is subject to feeling the effects of climate change. In particular, increased Arctic and Greenland ice melting will impact the freshwater distribution in the Labrador Sea. This has implications for the high-latitudes biological system as well as the process of deep convection.

The annual cycle in the Labrador Sea begins in the fall, with increasing surface buoyancy fluxes and frequency of storms. Extreme heat loss to the atmosphere and favorable preconditioning resulting in deep convection and Labrador Sea Water formation. Eventually, lateral buoyancy fluxes exceed surface fluxes, effectively ending convection and rapidly restratifying the region. Renewed stratification and increased irradiance permit the spring phytoplankton bloom, a period of intense primary production. The spring bloom is the base of the food web in the North Atlantic; higher trophic levels including North Atlantic fisheries depend on the annual spring blooms. Perturbations in timing or magnitude of the bloom will disrupt the food web.

Five Seagliders executed multi-month missions, collecting several thousand profiles of hydrography at relatively high horizontal and temporal resolution along the glider track (one profile to 1000 m approximately every 4 hours and 3 km). Two gliders were additional equipped with bio-

optical sensors which returned fluorescence, optical backscatter and dissolved oxygen concentrations in the upper 300 m of the ocean. Seagliders are also capable of estimating vertical water velocity at their location, and important diagnostic of deep convection.

Using these Seagliders and several auxiliary datasets, I investigated deep convection convection and the spring bloom. Satellite ocean color (SeaWiFS, 1998-2008), sea surface altimetry (TOPEX/Poseidon and Jason-1), meteorological reanalysis products (NCEP Reanalysis II, 1998-2006), climatologies of hydrography (World Ocean Atlas 2005) and mean dynamic ocean topography (Maximenko and Niiler, 2004; Niiler et al., 2003) give spatially coarse but broad coverage. *In situ* hydrographic data from Argo floats (2002-2006) and K1 mooring data are spatially sparse, but increase spatial sampling and long time series resolution, respectively.

The major themes of my thesis are the impact of freshwater on the spring bloom, the strength of high resolution glider hydrography, and observations of eddies in the bloom and during deep convection. This also constitutes the first usage of Seaglider vertical velocities to observe internal waves and deep convection.

Chapter 2

PHYSICAL CONTROLS AND MESOSCALE VARIABILITY IN THE LABRADOR SEA SPRING PHYTOPLANKTON BLOOM OBSERVED BY SEAGLIDER

2.1 Introduction

Seaglider transects of the Labrador Sea have established that advection of a low-salinity cap in the separation of the subpolar gyre from the West Greenland boundary current exerts strong control over deep convection and deep water production (Eriksen and Rhines, 2008). Here and in the next chapter, we argue that the same freshwater cap controls the dominant phytoplankton and zooplankton production of the western subpolar Atlantic. With global warming increasing the supply of surface freshwater, both physical circulation and biological productivity of the region are likely to be affected.

The Labrador Sea is the western branch of the subpolar gyre of the North Atlantic (Fig. 2.1a). Here the biological system is subject to nutrient replenishment by some of the deepest mixing in the northern hemisphere, as well as influences of mesoscale processes. The general circulation within the Labrador Sea is cyclonic, characterized by doming isopycnals and layers of distinct water masses in the boundary currents (McCartney and Talley, 1982; Yashayaev, 2007). The surface of the boundary currents and the shelves are capped with very fresh, very cold water of Arctic origins. Extending from 200 to 800 m deep, encircling the Labrador Sea, is warm, saline Irminger Sea Water of subtropical origin. Labrador Sea Water formed during deep convection fills the central Labrador Sea from near the surface to 2500 m depth. Farther below lie Northeast Atlantic Deep Water and Denmark Strait Overflow Water which, together with Labrador Sea Water, make up North Atlantic Deep Water. Boundary currents are concentrated on the Greenland and Labrador slopes. Offshore advection around the northern edge of the Labrador basin occurs in two or more diffuse branches (Fig. 2.1b). Deep waters are forced offshore by the shoaling topography, near the 3000-m isobath.

This boundary current separation is visible as an eddy-kinetic-energy maximum (Fig. 2.1b). Further outflow from the Greenland slope occurs near the 1000-m isobath. Within this offshore advection are found Irminger Rings, coherent mesoscale eddies that are characterized by the fresh shelf waters at the surface and Irminger Sea Water at intermediate depths.

The 1997 Labrador Sea spring bloom was observed by Head et al. (2000) from shipboard observations. They found two distinct bloom regions: the north bloom, which had ended by their sampling period (May-June), and the central Labrador Sea bloom, which was active. Their study also found low surface nitrate concentrations following the north bloom ($< 3\mu\text{M}$ to $< 1\mu\text{M}$ in places). They used their observations to relate the bloom to zooplankton activity, and found that the timing of life cycles of the most abundant copepod, *Calanus finmarchicus*, corresponded to the time of the peak bloom, and that the north bloom region had the highest copepod biomass. Two other works on Labrador Sea spring blooms focus on bloom timing, one using SeaWiFS ocean color and a numerical model (Wu et al., 2008) and the other using SeaWiFS and hydrography (next chapter). These studies have the advantage of a long, daily time series (1998-2003 and 1998-2008), but lack *in situ* observations to make a direct connection with water-column stratification or dynamics.

Recent studies in biophysical interactions have focused on small scale processes that may vertically mix nutrients, increasing the surface supply for new production (see review by Klein and Lapeyre, 2009). Motivation for these studies is based on the idea that simple basin-wide diapycnal upwelling does not supply enough nutrients to support the observed productivity. Transient mesoscale effects which may increase surface nutrient supply include the doming of isopycnals by eddies—bending the nutricline into the euphotic zone at the base of the eddy (McGillicuddy et al., 1998). However, even mesoscale processes may be insufficient to support observed production. A recent numerical study which included mesoscale but not submesoscale processes increased the surface nutrient supply substantially, but was still 30% too low when globally-averaged (McGillicuddy et al., 2003). Submesoscale processes, on the order of 1 to 10 km scale, at the fronts surrounding eddies or in narrow but long filaments may be responsible for exceedingly large vertical currents (on the order of 100 m/day) and associated nutrient transport (Mahadevan et al., 2008). The scale of these features stretches current observational and numerical limits. While Seaglider data are insufficient to resolve the submesoscale, high-resolution *in situ* observations of physical and biological quantities may help identify processes that influence productivity, perhaps by supplying the miss-

ing nutrients. While production in the subpolar gyres is primarily supported by nutrients upwelled during deep wintertime mixing (Lévy, 2005), mesoscale processes are still active and potentially increase net primary productivity.

In this chapter, we use the Seaglider, a long-range (6 months) autonomous underwater instrument able to resolve mesoscale features in hydrography and bio-optics to 1000 m depth. Over 500 profiles of hydrography and bio-optics are available from the spring and summer of 2005 in the Labrador Sea (Fig. 2.1). We will show the influence of stratification and basin-scale circulation, as well as small scale processes in three regions of the Labrador Sea, on the spring bloom and later productivity.

2.2 Data sources & processing

2.2.1 Seaglider

The Seaglider is an autonomous underwater vehicle developed at the University of Washington (Eriksen et al., 2001). It navigates using dead reckoning and Global Positioning System (GPS) locators, receives instructions and transmits data via the Iridium satellite system after each dive-climb cycle. Profiles are made to 1000-m depth with an approximately 1:3 vertical to horizontal slope. Relative to aspect ratios of physical features in the Labrador Sea (e.g. a 100 m mixed layer depth divided by a largest Rossby radius of 10s of kilometers, or the related Prandtl ratio, f/N where f is the Coriolis frequency and N the buoyancy frequency), a 1:3 slope is effectively vertical. The glider typically surfaces 6 km relative to the depth-averaged current from where it began its dive. On its sawtooth trajectory, the glider sample-spacing averages 3 km, but near the surface and 1000 m turnaround points, sampling is irregular, ranging from 100s of meters to 6 km. During a single dive-climb cycle, sampling is done at variable time intervals, ranging from approximately every 0.6 m in the top 150 m, incrementally reducing to 2.4 m from 250-1000 m.

In this observational program, 5 Seagliders were deployed between October 2003 and August 2005. Seaglider S/N 16, hereafter sg016, the focus of this chapter, was deployed 5 April 2005 from Nuuk, West Greenland (64.2°N, 51.8°W, Fig. 2.1). Moving at approximately 20 cm s⁻¹ and buffeted by eddies, it followed a westward track along 64°N and then 900 km south along 58°W, reaching the Labrador shelf around 20 June (Fig. 2.1). Along this track, the Seaglider measured temperature

and conductivity (Sea-Bird Electronics (SBE) custom sensor), pressure (Paine Corporation 211-75-710-05 1500PSIA), fluorescence and optical backscatter (WETlabs custom ECO-BB2F puck), and dissolved oxygen (SBE 43F Clark-type oxygen electrode). Depth-averaged horizontal velocities are calculated from Seaglider measurements, using a flight model based on Seaglider hydrodynamics and surface positions between two consecutive surfacings with typical error of about 1 cm s^{-1} . Data calibration details are given below.

Salinity

To conserve power and extend the range of the Seaglider, the SBE conductivity cell is unpumped. The measurement relies on glider motion through the water to passively flush the conductivity cell. The rate of flushing depends on glider attitude and speed, which depend on buoyancy. We estimate this flushing speed based on the Seaglider flight model (Eriksen et al., 2001) and use it to apply thermal inertia corrections to the conductivity data following Lueck (1990). Relaxation constants are determined by minimizing the along-isopycnal difference between salinities of successive climb-dive near the surface or dive-climb at depth. This processing reduces differences in salinity but, because of uncertainty in the flight model and likely effects of small-scale turbulent motions around the glider sensors, it does not remove all spike and hysteresis artifacts. Remaining spikes are removed (salinities below 30 and above 36) and resulting data are binned to 2 m resolution.

Potential density was then calculated using corrected salinities, in order to determine mixed-layer depths. Density profiles were first smoothed with a 20 m moving depth boxcar. Mixed-layer depths were calculated as the first depth where density in the 20 m bin exceeds the surface 20 m bin by at least 0.1 kg m^{-3} (Lilly et al., 2003), an adequate threshold for the strong spring and summer pycnoclines in the Labrador Sea.

Dissolved oxygen

The oxygen electrode sensor has been known to drift with time and use [a decrease of $10\text{-}20 \mu\text{mol L}^{-1}$ per 100 days (Nicholson et al., 2008)]. For this reason, it is most often calibrated by comparing measurements to *in situ* bottle samples. The sensor used here was calibrated within 6 months of deployment, but oxygen concentrations were measured well below normal for this region—subsaturated by

30% instead of 6% as observed by Körtzinger et al. (2008). We calibrated sg016 oxygen against oxygen measurements from a repeat hydrographic section across the Labrador Sea known in *World Ocean Circulation Experiment* (WOCE) terminology as AR7W (Fig. 2.2a). AR7W measurements were made with a rosette-mounted oxygen electrode that was then calibrated against bottle samples using Winkler titration. Thirteen pairs of glider-AR7W profiles were found within 50 km and 2 weeks of each other (Fig. 2.2b-c). While these measurements were serendipitously close in space and time, estimates of oxygen decorrelation scales (described below in §3) are shorter than 50 km, and blooms can peak and decline within 2 weeks. Natural variability in the AR7W oxygen profiles was 10-15 $\mu\text{mol L}^{-1}$ and up to 30 $\mu\text{mol L}^{-1}$ for gliders near 300 m. We calculated the root-mean-square error between calibrated Seaglider oxygen and AR7W data for 6188 points of comparison, to be 15.6 $\mu\text{mol L}^{-1}$. In the absence of additional data available for calibration and reasonable factory-calibrated measurements, we used factory-calibrated oxygen from a second glider sg015, which travelled along nearly the same track as sg016 six months earlier, to complete the annual cycle. Corrected data show surface saturation near equilibrium in the early spring, before the first observations of elevated fluorescence, which quickly reached supersaturation of 5-10% in regions with elevated fluorescence.

Fluorescence and optical backscatter

Fluorescence and optical backscatter relate to biological activity, though conversions between them to chlorophyll, phytoplankton biomass or other parameters of interest are non-unique. Fluorescence (F) is a proxy for the concentration of chlorophyll a , which fluoresces over a range of wavelengths centered near 683 nm. The Seaglider WETlabs puck excites chlorophyll using a blue LED and detects near-infrared fluorescence at 700 nm, but with a wide enough band to pick up fluorescence at 682 nm (Perry et al., 2008). The WETlabs puck measures scattering at red and blue wavelengths, 700 and 470 nm [particulate backscatter coefficients $b_{bp}(700)$ and $b_{bp}(470)$].

In the absence of other measurements, fluorescence is often taken to reflect biomass (carbon) though this is not always the case. Carbon-to-chlorophyll ratios are affected by photoacclimation, phytoplankton size, species assemblage, and pigment composition (Cullen, 1982). Even within one region, the relationship between fluorescence and chlorophyll measurements may vary. Lutz et al.

(2003) found that the relationship between fluorescence and water sample estimates of chlorophyll in the Labrador Sea changed over the course of a few months. Recent bio-optics literature focus on the measurement of particulate optical backscatter which may correspond better phytoplankton biomass in the open ocean, though the measurement can respond to other substances as well (Fennel and Boss, 2003; Behrenfeld and Boss, 2003).

For our purposes, we have converted fluorescence and optical backscatter volts into a “bloom intensity” index with units of chlorophyll concentration using an algorithm described below in §2.2.2. All figures and numbers in the text use F^* and b_{bp}^* , the bloom intensity index calculated from fluorescence and backscatter. Seaglider estimates of fluorescence and backscatter correlate well ($r^2 = 0.69$, Fig. 2.3). There is more spread in the scatter near the surface (top 10 m, Fig. 2.3a) on the Labrador slope (squares). Here, surface fluorescence-to-backscatter ratios vary much more than at 20-30 m (Fig. 2.3b). At 50-60 m depth (Fig. 2.3c), only the northern region (triangles) exhibits large values and the correlation is tight.

This variability in the fluorescence-to-backscatter ratio ($F:b_{bp}$) appears as a diurnal cycle in the surface layer (Fig. 2.4a). This is indicative of fluorescence quenching, a reduction in fluorescence quantum yield, often observed during the daytime (Sackmann et al., 2008). The vertical extent of quenching decreases with depth (Fig. 2.4b-c): backscatter is nearly uniform in the mixed layer, while fluorescence has a subsurface peak in the mixed layer which decreases nearer the surface. Quenching is reduced at depth because of light attenuation by water and particles (such as phytoplankton cells). The diurnal cycle is strongest in the surface layer, ranging from $F:b_{bp}$ peak-to-trough amplitude of 3 mg m^{-3} vs 1 mg m^{-3} at depth. The black filled hatched area is instantaneous PAR (iPAR), calculated as in Sackmann et al. (2008) so that the integral of each day’s iPAR equals the daily value given by SeaWiFS satellites, by fitting a half-sine from sunrise to sunset. Maximal quenching in the Labrador slope region, that is, the lowest values of $F:b_{bp}$, occur on average 0.3 hrs after the peak in iPAR. (On 1000 m deep dives, the Seaglider only surfaced every ~ 8 hrs so some aliasing is expected.) The ratios show quenching in the daytime surface by 70% relative to deep fluorescence to backscatter ratios, similar to values found by Sackmann et al. (2008) off the Washington coast. Because of our confidence in surface backscatter correlating with fluorescence, we will use backscatter in regions where quenching is in effect.

2.2.2 *Satellite ocean color and Seaglider bloom intensity indices*

Though the Seaglider offers the strength of colocated physical and biological measurements, space-time aliasing can hinder interpretation of the data. We use satellite ocean color to place Seaglider data in the large-scale bloom patterns of the Labrador Sea. We used a daily, mapped 9 km resolution SeaWiFS chlorophyll-*a* product (Feldman and McClain, 2006). (For visualization only, in Fig. 2.5, we used the merged SeaWiFS and MODIS (MODerate-resolution Imaging Spectrometer) product, at 8-day, 4-km resolution, which had better spatial coverage but is considered an evaluation product only.)

Comparing SeaWiFS chlorophyll with *in situ* fluorescence, Perry et al. (2008) found that Seaglider fluorescence estimates of chlorophyll were three times as large as concurrent SeaWiFS estimates off the Washington coast. This is not altogether surprising since the SeaWiFS algorithm is still undergoing revision to make it more accurate regionally. Furthermore, SeaWiFS measurements are a 9-km by 9-km spatial average while Seaglider estimates are point measurements. Boss et al. (2008) found that APEX float measurements of fluorescence in the Labrador Sea agreed well with satellite estimates over a 3-year period. While the relationship between *in situ* fluorescence and SeaWiFS chlorophyll is complicated and not yet fully resolved, we have used SeaWiFS chlorophyll to convert fluorescence to chlorophyll concentration. In the absence of bottle estimates of chlorophyll-*a*, we relate Seaglider fluorescence and optical backscatter to SeaWiFS chlorophyll by creating a bloom index of intensity. While this procedure does not guarantee quantitative accuracy, it makes possible direct comparisons between data sources.

To calculate the bloom intensity index, we averaged Seaglider fluorescence and backscatter counts in the top 10 m, and created a SeaWiFS time series of chlorophyll by averaging measurements within ± 2 days and $\pm 0.5^\circ$ of each glider surface position. The methodology is similar to that in Sackmann (2007). We regressed the average backscatter against the SeaWiFS time series, and used the coefficients to convert backscatter counts into units of chlorophyll [mg m^{-3}]. The process for fluorescence was similar, except that we only compared SeaWiFS chlorophyll with fluorescence measurements made between 5 pm and 5 am UTC, to reduce the effect of quenching. We transform the full fluorescence and backscatter data sets similarly. Hereafter, we will refer to the SeaWiFS product as chlorophyll concentration and Seaglider as fluorescence, backscatter or bloom intensity.

2.3 Basin-scale hydrography and productivity

The Labrador Sea may be divided into three distinct zones of hydrography and productivity. (1) The north Labrador Sea, above 60°N and east of the Labrador shelf, has the earliest, most intense bloom. This region is also the location of the highest biomass of *Calanus finmarchicus*, the most abundant copepod in the region, and of the offshore-flowing branch of the West Greenland Current. (2) The central Labrador Sea is a site of deep convection with wintertime mixed layer depths ranging from 1000 to 2500 m. The spring bloom here occurs after deep convection has ended. (3) The Labrador shelves are ice-covered well into the spring, and have a quick ice-melt bloom followed by a second surface bloom. The Labrador Current on the shelf is extremely fresh ($S < 32$) and separated from the central Labrador Sea by an intense shelf-break front.

Sg016 travelled over 2000 km from April to August, 2005, describing the hydrography (Fig. 2.6) and crossing the three productive zones at various stages in their annual cycles (Fig. 2.5). Labrador Sea climatological surface chlorophyll, 2005 surface chlorophyll, and glider timing relative to the local blooms for occupation of the three zones are shown in Fig. 2.5. Sg016 salinity, temperature, bottom depth, fluorescence and a time series of surface bloom intensity for the entire glider section are in Fig. 2.6. From this record, north Labrador Sea hydrography is similar to deep West Greenland Current water because of the offshore flow of freshwater from deep boundary currents. This region has a fresh surface and warm, salty subsurface layer (Fig. 2.6: North). The central Labrador Sea bloom occurs in a warm layer above a deep homogenous layer (Fig. 2.6: central LS). The influence of these physical characteristics on productivity will be described further in later sections.

The 2005 spring and summer were different than climatology in that the north bloom was weaker than usual (Fig. 2.5a and d). The 2005 central Labrador Sea bloom and decline were similar in magnitude to climatology (Fig. 2.5b, c, e, f). The glider crossed through the north region during the local peak bloom and decline (see Fig. 2.5g). Continuing southward along 58°W, it skirted the western edge of the central Labrador Sea and encountered a secondary bloom near 58°N on the Labrador slope (Fig. 2.5h). During this time, it also crossed onto the Labrador shelf twice. On the shelf, it observed a thin, subsurface phytoplankton layer (Fig. 2.5c). Upon leaving the shelf a second time, the glider measured a persistent productive region at the Labrador shelf-break front after the local bloom had declined (Fig. 2.5i).

Glider bloom intensity in the top 20 m covaries with SeaWiFS surface chlorophyll (Fig. 2.6e) though Seaglider fluorescence is more variable, in part because of the spatial averaging intrinsic to SeaWiFS measurements. While the north bloom was less intense than the central Labrador Sea bloom, as estimated by bloom intensity near the surface, depth-integrated chlorophyll estimates are similar in the two regions: with a mean \pm standard deviation of $71.4 \pm 37.5 \text{ mg m}^{-2}$ in the north (for 151 profiles), and $71.1 \pm 22.0 \text{ mg m}^{-2}$ in the central Labrador Sea bloom (for 139 profiles). These compare well with *in situ* estimates by Cota et al. (2003), who found integrated chlorophyll concentrations of $99 \pm 55 \text{ mg m}^{-2}$ in May-June 1997 (76 profiles), while wintertime values were $47 \pm 38 \text{ mg m}^{-2}$ (74 profiles).

Decorrelation length scales for mixed-layer average properties are all less than 100 km, and closer to 5-20 km (Fig. 2.7a-c). Mixed-layer concentrations of fluorescence and oxygen are very variable, while salinity and temperature have lower frequency/wavenumber changes (Fig. 2.7a). This is quantifiable by calculating autocorrelations for mixed layer properties, shown in Fig. 2.7b and c. The two regions shown here are the north bloom, from 400-650 km, which is characterized by fresh eddy-like features of 15-30 km scale (described in the next section) and the early central Labrador Sea bloom, which is in a relatively homogenous, gradually warming mixed layer. In both regions, biological variables (fluorescence and oxygen) decorrelate more rapidly than salinity and temperature. Contrasting the two regions, the north bloom temperature and salinity decay more quickly than the central Labrador Sea. This is a consequence of the glider passing through the eddy-like structures, which have characteristic scales of 15-30 km (described further below).

Drifter studies of correlation scales in physical (temperature) and biological (chlorophyll) variables have shown that the phytoplankton distribution is strongly affected by physical processes (Abbott and Letelier, 1998), however at longer time scales, biological processes appear to dominate. Also in the California Current system, Denman and Abbott (1994) found rapid decorrelation (after 1 day) at length scales of 12.5-25 km while at larger scales it was 7-20 days. While the decorrelation scales calculated here were described as decorrelation length scales, sg016 was moving in space and time. Moving at typically 18 km a day, it is aliasing a spatial decorrelation with the temporal decorrelation. Hence the spatial interpretation here applies particularly to regions where properties are changing slowly. Overall, short decorrelation scales show the strong heterogeneity in biological properties within the mixed layer, emphasizing the need for high-resolution measurements like

those by Seaglider.

Surface oxygen, an indicator of time-integrated net production modulated by physical mixing, also covaries with fluorescence bloom intensity. Fig. 2.8 shows Seaglider oxygen for October 2004 through August 2005 averaged in the top 40 m. Wintertime values are lower, and subsaturated by 10%, likely because of deep mixing of surface waters with relatively oxygen-depleted deeper water. In the spring bloom, oxygen becomes supersaturated by 5-10% at the end of April, and again at the later observations of high productivity. The annual cycle compares well with measurements by Körtzinger et al. (2008) on a mooring in the southwest Labrador Sea (56.5°N, 52.6°W) during the same time range. They found wintertime saturation were about 6% undersaturated, because of convective mixing with subsaturated deep water, and spring blooms up to 10% supersaturated. In later sections, we have used oxygen saturation relative to fluorescence to comment on the likely time-history of productivity.

2.4 Mesoscale biological and physical features

2.4.1 North bloom & mesoscale eddies

As mentioned above, the north region has the highest eddy kinetic energy in the Labrador Sea. Seaglider observations of high fluorescence appear to be located within and around several mesoscale eddies that had originated in the West Greenland Current. As the glider was making observations, it was deflected by strong horizontal currents into the path shown in Fig. 2.9. The glider can typically correct for currents up to 20 cm s⁻¹, but it experienced currents up to 40 cm s⁻¹ (Fig. 2.9). Comparing track deflections and altimetry, it appears as though, near 58°W and 63°N, the glider encountered a cyclonic-anticyclonic eddy dipole. Sea surface heights were depressed then elevated (not shown), resulting in alternating surface geostrophic currents along an altimeter track (Fig. 2.9b, black line and arrows). Coincident with the anticyclone were very low mixed-layer salinities (Fig. 2.9a, lens 4). Here, we refer to the features as fresh “lenses” if their hydrographic properties match those of Irminger Rings but sea surface height data showing the velocity structure is lacking. Without such evidence, it is possible that the features are instead thin filaments of water, retaining the watermass properties but not the dynamic structure of a vortex eddy.

Fresh lenses were identified by applying a threshold salinity gradient along the glider track

(Fig. 2.9a). Two of them appear sequentially in the glider data but, in this mapped view, clearly are the same physical feature (lenses 2a and 2b). The 4 distinct fresh lenses have core salinities less than 34.2 and temperatures less than 2°C (Fig. 2.10b, c). At 400-800 m, these lenses also have warm, salty cores of Irminger Sea Water (Fig. 2.6a, b), indicating that they originated in boundary currents. Their hydrography is consistent with Irminger Rings, coherent vortex eddies that may or may not have a fresh surface layer, but do have a warm, salty layer with $\theta \approx 3.59 - 4.75^\circ \text{C}$ (Lilly et al., 2003; Rykova, 2006). Along the Seaglider track, the fresh lenses are up to 30 km wide (Fig. 2.10). While we do not know the orientation of the glider through an eddy, this is consistent with typical scales of Irminger Rings 15-30 km across (Lilly and Rhines, 2002; Prater, 2002; Rykova, 2006; Hátún et al., 2007).

Generally, high fluorescence was confined to the low-salinity surface layer of the eddies (Fig. 2.6a, d). The low-salinity layers result in a shallower mixed-layer depth which, for the first time in this record, brings the mixed layer depth above Sverdrup's critical depth (Sverdrup, 1953), a condition required for a spring bloom (not shown). This demonstrates the importance of buoyant freshwater layers associated with the offshore advection of the boundary currents and eddy flow. In the first three lenses, fluorescence, backscatter and dissolved oxygen are uniform in the mixed layer ($\approx 3 - 4 \text{mg m}^{-3}$, and oxygen supersaturated), then decay in the 20 m below (Fig. 2.11). The fourth lens has supersaturated oxygen in the mixed layer though fluorescence has returned to background values. Oxygen-to-fluorescence ratios can indicate different stages in the life-cycle of a bloom (Nicholson et al., 2008). As a bloom develops, oxygen and fluorescence increase. Once the bloom peaks and decays, fluorescence decreases but oxygen supersaturation remains, until consumed by respiration or reduced by gas exchange and physical mixing. This suggests that anticyclone lens 4 had recently experienced a phytoplankton bloom. That the glider did not observe high fluorescence in lens 4 may be due to the decline of the local bloom, as evidenced by the annual cycle of SeaWiFS chlorophyll in Fig. 2.5g.

For lenses 1, 2a and 2b, observed during the local peak bloom while fluorescence was still elevated (Fig. 2.5g), we separated glider profiles into those taken within the fresh core of the lenses and those between the fresh cores. Averaging these vertical profiles together, we compared salinity and fluorescence bloom intensity (Fig. 2.12). By construction, the salinity inside the lenses is lower (by about 0.15), while the fluorescence bloom intensity is higher at the edges of fresh lenses (by

about 0.5 mg m^{-3}). There is overlap between variance in the fluorescence profiles, shown by the shaded areas (1 standard deviation at each depth level). The wide range in fluorescence is partially explained by the bloom decaying in time, as can be seen by comparing fluorescence levels in lens 2a with 2b (Fig. 2.11a, last column). The vertical profile of fluorescence from lens 2a is higher than from 2b (about 4 days later) by about 0.4 mg m^{-3} .

Discussion. Eddies can have several effects on productivity and measurements of chlorophyll: strong haline stratification of the eddies stabilizes the surface layer, creating shallow (20-50 m) mixed layers; horizontal advection of nutrients from the eddy-formation region (Lévy, 2003); vertical velocities associated with eddy-pumping or eddy-wind effects may increase the nutrient supply to the surface, bringing deeper, nutrient-rich waters into the euphotic zone (McGillicuddy et al., 1998; Siegel et al., 1999; McGillicuddy et al., 2007; Mahadevan et al., 2008); or, eddies may simply stir laterally a pre-existing patch of chlorophyll, resulting in high-wavenumbers but no additional production. For a recent review of mesoscale and submesoscale mechanisms for vertical mixing, see (Klein and Lapeyre, 2009).

From Seaglider observations, we found high fluorescence within and at the edges of eddies. Since nutrient data in the region are poor, we cannot address whether the eddy is horizontally advecting high-nutrient water from the Greenland shelf to the open north Labrador Sea. The haline stratification does result in shallower mixed-layer depths than water further from the eddies. If it were not for the higher fluorescence at the eddy edges than their centers, it would be possible that stratification is the only influence these eddies have on the phytoplankton productivity. However, the higher fluorescence at edges suggests the possible role of edge effects—either simple eddy-wind effects described in McGillicuddy et al. (2007) who observed high fluorescence concentrated in the edges of a subtropical North Atlantic eddy or the nonlinear Ekman effect outlined in Mahadevan et al. (2008).

2.4.2 Central Labrador Sea & thermal warming

The central Labrador Sea bloom was observed between June 11 and July 12, 2005, along 58°W on the Labrador slope. Along this track, from mid-May to June, the surface waters gradually warmed from less than 3° to greater than 5°C (Fig. 2.6b). Comparing the time series of sea surface tem-

perature from Advanced Microwave Scanning Radiometer - Earth Observing System (AMSR-E) through cloud observations (not shown), most of the change in temperature that the glider observed was due to the annual cycle of sea surface temperature, rather than the glider traveling southward through a gradient in temperature (Wentz and Meissner, 2004). In contrast, the gradual salinification of surface waters (from 34.5 to 34.7) was most likely due to a gradient in sea surface salinities.

Like the north bloom, the central Labrador Sea bloom was concentrated in the mixed layer (top 40 m), with a decay over the next 30 m to near background levels (Fig. 2.11b). Fluorescence and backscatter values are nearly uniform in the mixed layer (3-4 mg m^{-3} bloom intensity), consistent with a surface concentrated bloom in an actively mixing layer.

Discussion. Following 1000-2500 m deep winter mixing, surface nutrient levels are expected to be high. This contrasts with the north bloom, where wintertime mixed layers are confined to the upper 200-300 m. A primary difference between the north and central Labrador Sea is the source of stratification: warm or fresh. In the central Labrador Sea, thermal warming was key to stratifying the surface layer, while the north bloom was strongly haline-stratified. The balance of haline vs thermal stratification is best shown by comparing buoyancy anomaly in the two regions between the surface and a reference depth. While the central Labrador Sea is both thermal- and haline-stratified (warm and fresh), the north bloom is stratified in spite of destabilizingly cold surface waters (very cold and very fresh) (Fig. 2.13). Maps of buoyancy anomaly to 500 m show that this difference is consistent between the north and central Labrador Sea—indeed, the entire subpolar North Atlantic (Bailey et al., 2005).

Thin layer in Labrador Current

In the pycnocline on the Labrador shelf, the glider observed a 5-m thin layer of high fluorescence and backscatter (up to 1500 fluorescence counts, or 10 mg m^{-3} of chlorophyll in bloom intensity). This subsurface fluorescence maximum is not visible in SeaWiFS chlorophyll (Fig. 2.5), nor does it appear in the time series of glider bloom intensity index, which was calculated in the top 20 m to compare with SeaWiFs. The glider observed the thin layer in two locations, both on the Labrador shelf: the first excursion onto the shelf was at 56.4°N, 57.8°W on June 22, 2005, and the second at 54.8-55.1°N, 54.1-54.6°W on July 15-16, 2005. Both times were after the local surface bloom,

which occurs in late May to early June (Fig. 2.5i).

The thin layer was visible in fluorescence, oxygen and backscatter profiles (Fig. 2.11c), and can be seen in the swath of fluorescence from the entire section (Fig. 2.6d, circled in red). From the profiles, it is clear that the thin layer is located within the surface pycnocline. Oxygen is also elevated, but peaks more shallowly than does fluorescence by about 5 m, and still within the pycnocline (Fig. 2.11c).

The thin layer is at distinct isopycnals in the two excursions onto the shelf. All profiles from the two occupations of the Labrador shelf and showing a thin layer are in Fig. 2.14 row 3, fluorescence in isopycnal space. The layer varied from 15 to 30 m depth but, in the first encounter with the shelf (1500 m along track, Fig. 2.6), it was at the 1027-1027.5 kg m^{-3} isopycnal, and at the second encounter (1900 km along track), it was at the 1025.5-1026.5 kg m^{-3} isopycnal (Fig. 2.14). The earlier, more northerly observations are at a deeper isopycnal than the later observations but both thin layers were approximately 5 m thick.

Discussion. Subsurface chlorophyll maxima were identified in the earliest profiles of chlorophyll. Mechanisms for their creation are reviewed by Cullen (1982), including subsurface chlorophyll maxima that are not representative of maxima in biomass, maxima created by density gradients alone, maxima resulting from depth-differential grazing of zooplankton, sinking and aggregation, or the intersection of the nitracline and euphotic zone. The term thin layer has been used more recently by Franks (1991) to refer to microscale layers of phytoplankton on the order of 10s of centimeters. Mechanisms for the creation of a subsurface layer include the sinking of a productive layer out of the photic zone or physical shearing of an initially thicker layer (Deksheniaks et al., 2001; Alldredge et al., 2002; Stacey et al., 2007; Ryan et al., 2008; Birch et al., 2008).

On the eastern shelf of Greenland, thin layers were found that were not limited by surface nutrients, i.e. not at the intersection of the euphotic zone and nitracline (Waniek et al., 2005). The authors suggested that the thin layer results from a sinking layer of biomass or pressure from grazing zooplankton. Nitrate observations on the central Labrador shelf in late May 1997 showed high surface nitrate levels (5-7 μM) (Head et al., 2000). On the more southerly Labrador shelf (52°N in early June), surface nitrate was below 1 μM in the top 10 m but 5 μM at 25 m. If nitrate distributions were similar in 2005, then the Seaglider-observed thin layer could be in the intersection of the pycnocline and nitracline.

On the other hand, if the two glider excursions onto the shelf observed a contiguous thin layer feature within the Labrador current, then surface intensified shearing of an initially thick layer of plankton would explain the observed upstream measurements being at a deeper isopycnal than the downstream measurements. Progressive shearing of an initially thick patch would result in thinning with time as well, however, which was not observed (both layers being about 5 m). Still, it is possible that the thin layer had achieved a steady-state balance between shearing and diffusion, resulting in a constant final thickness (Birch et al., 2008).

Finally, including the oxygen record as well, the peak of oxygen at a shallower depth than the fluorescence peak suggests a progressive sinking of the productive layer. Oxygen levels reflect time-integrated net productivity, suggesting that production was higher in the shallower layer. High fluorescence in the lower layer without accompanying high oxygen could indicate that the thin layer is progressively deepening during the glider observations. Since the glider did not collect nutrient data, we can not speculate as to whether the sinking was due to nutrient control, zooplankton predation or aggregation at a level of neutral density for the phytoplankton.

Shelf-break front productivity

As the glider left the Labrador shelf for the second time, it created a high-resolution swath of hydrography and bio-optics in the shelf-break front, seen in the entire Seaglider section (Fig. 2.6) and in salinity and fluorescence alone (Fig. 2.15). At the front is a 20 m thick high fluorescence layer, sandwiched between the 34.35-34.45 isohalines below the mixed layer from 30-50 m deep but varying with the depth of the front. Both fluorescence and backscatter are elevated (Fig. 2.11), though fluorescence decays more rapidly with depth than does backscatter. Oxygen peaks above fluorescence by a few meters, and decays even more rapidly than does fluorescence.

In contrast to the thin layer within the Labrador Current, the shelf-break front productive layer outcrops several hundred kilometers from the shelf, at the 1000-m isobath. This outcrop is visible in SeaWiFS ocean color as a narrow along-slope region of elevated chlorophyll, lasting well after the primary Labrador slope and central blooms (Fig. 2.5f, i). On the northern section, the front is steeper, aligning with the 34 outcropping isohaline.

Discussion. Fronts can be both sites of high productivity through upwelling of nutrients and

sites of downwelling of biomass, contributing to the biological pump (Franks, 1992; Flierl and Davis, 1993; Spall and Richards, 2000; Allen et al., 2005). This front is also a watermass boundary separating the deep boundary currents and Labrador shelf current. While Seaglider did not collect nutrient data, historical observations by Head et al. (2000) showed variations in nitrate concentration around the shelf-break front. At 55°N, they found depleted nutrients near the surface in early June while, on either side, surface nitrate was 2-6 μM higher. This is in contrast with the expectation that the front supplies additional nutrients to the surface, unless productivity is also elevated to a point that nutrients are depleted very quickly. Here, observations of deep fluorescence along the frontal isopycnals suggest some downwelling of biomass, while the persistent fluorescence even after the surface bloom has decayed may suggest additional nutrient sources. Oxygen peaks above fluorescence and backscatter by a few meters, and decays more rapidly, possibly because shallower phytoplankton may be more productive, having access to more light.

2.5 Conclusion

Sg016 crossed the Labrador Sea during the spring and summer of 2005, making coincident high-resolution measurements of salinity, temperature, fluorescence, optical backscatter and oxygen along a sawtooth path. Along the transect, it crossed several distinct biogeographical regimes. The north Labrador Sea bloom is early and intense, producing the greatest quantity and biomass of zooplankton in the region (Head et al., 2000; Frajka-Williams and Rhines, 2008), a consequence of surface low-salinity water advected from the Greenland boundary current as eddies plus background mean flow. The central Labrador Sea blooms once thermal warming has stratified the surface layer after deep convection.

In the north Labrador Sea, where the deep boundary currents traverse the northern edge of the Labrador basin, the glider observed high fluorescence and oxygen saturation within and at the edges of fresh surface lenses associated with Irminger Rings, with mixed layer depths about 40-50 m, shallower than surrounding water. The first effect of these eddies, as part of the mean offshore advection of low-salinity water, is to increase surface stratification which allows the early northern bloom. While eddies at this latitude are only 15-30 km in diameter, high horizontal resolution Seaglider profiles were able to describe their structure and biological influence. Velocities $> 30 \text{ cm s}^{-1}$

prevented sg016 from crossing directly through the eddy, but it was able to distinguish between properties within and between the eddies, showing that fluorescence was elevated at eddy fronts. This finding, combined with eddy concentration explaining a fraction of interannual bloom variability (Frajka-Williams and Rhines, 2008) suggests that eddies are also responsible for increasing the supply of nutrients in the surface layers of the ocean.

The central Labrador Sea bloom was observed along its western edge on the Labrador slope. This bloom occurred once the region had been thermally stratified and, in 2005, had a higher surface chlorophyll concentration than the north bloom (which is typically the larger bloom). However, Seaglider estimates of depth-integrated chlorophyll are similar between the two regions: $71.4 \pm 37.5 \text{ mg m}^{-2}$ in the north, and $71.1 \pm 22.0 \text{ mg m}^{-2}$ in the central Labrador Sea bloom.

Two subsurface high fluorescence layers were observed on the Labrador shelf: a thin layer within the equatorward Labrador shelf current and at the Labrador shelf-break front. In the very fresh, cold Labrador Current, sg016 found a layer of high fluorescence at the base of a thermally-warmed mixed layer. This thin layer had chlorophyll values of up to 10 mgm^{-3} and, while only 5 m thick, was persistent. Seaglider made two excursions onto the shelf, roughly 1 month apart, finding that the thin layer present at denser isopycnals upstream (north) and less dense isopycnals downstream (south). Phasing of oxygen and fluorescence (oxygen peaks shallower than fluorescence) suggests a deepening of the productive region through the pycnocline, possibly also through the nutricline as surface nutrients are depleted.

The Labrador shelf-break front was home to a second subsurface layer of high fluorescence, backscatter and oxygen. This layer was sandwiched within isopycnals defining the front, and outcropped at the 1000-m isobath, where it was visible in SeaWiFS ocean color. The deep occurrence of high fluorescence is suggestive of a downwelling of biomass, while the persistence of fluorescence after the surface bloom had decayed may suggest an upwelling of nutrients.

While our understanding of the link between physical processes and biological productivity was limited by the absence of nutrient data, high-resolution data in horizontal and vertical space from sg016 allowed an unprecedented view of *in situ* physical-biological connections in the Labrador Sea. Calculations of decorrelation length scales showed that biological variables decorrelated on scales of 20-30 km, emphasizing the need for high-resolution observations. This study complements the larger-scale, longer term observations by satellite (Wu et al., 2008; Frajka-Williams and Rhines,

2008) by illuminating mesoscale physical and biological features that may be responsible for large-scale bloom patterns.

Acknowledgements

This work was performed with support from an NSF Physical Oceanography grant. Eleanor Frajka-Williams was supported by an NSF graduate research fellowship for a part of this work. The manuscript was much improved by comments from anonymous reviewers. Helpful discussions were had with Eric D'Asaro, Steve Emerson, Bruce Frost, Amanda Gray, Eric Kunze, Jonathan Lilly, David Nicholson, Eric Rehm and Brandon Sackmann. Many thanks to the people who gathered or provided data used here including the Seaglider teams, Igor Yashayaev, SeaWiFS data team, Mathieu Ouellet, and DFO BioChem database.

2.6 Figures

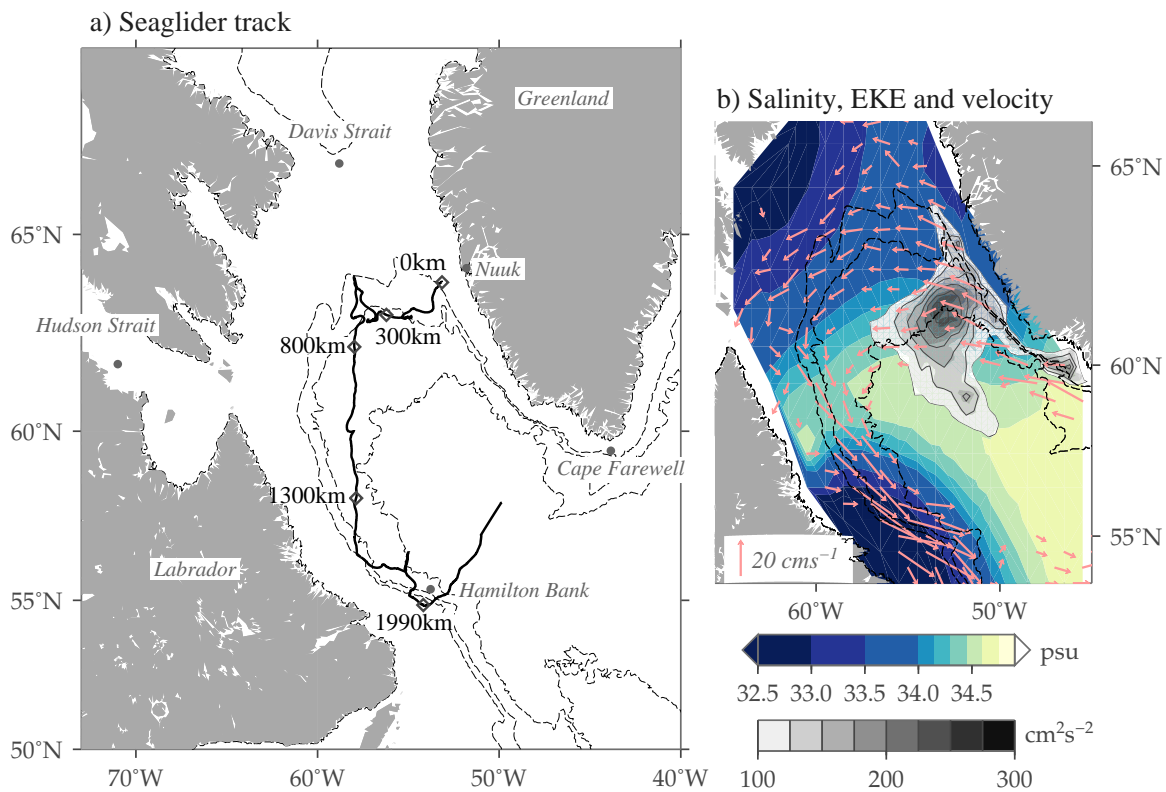


Figure 2.1: The Labrador Sea is situated between Labrador in Canada and Greenland. (a) The glider track in the Labrador Sea and (b) climatological sea surface salinity, eddy kinetic energy and mean surface currents. Landmasses, locations and bathymetric contours at 1000 m intervals are marked. Distance along the glider track is marked in kilometers, indicated by diamonds along the track. Sea surface salinity is from the World Ocean Atlas 2005, March (blue colormap); eddy kinetic energy is from the Aviso velocity anomaly product (1992-2007, grayscale colormap) and mean currents from the Aviso mean velocity product (1992-2007, pink arrows). The altimeter products were produced by Ssalto/Duacs and distributed by Aviso, with support from Cnes (<http://www.aviso.oceanobs.com/duacs/>)

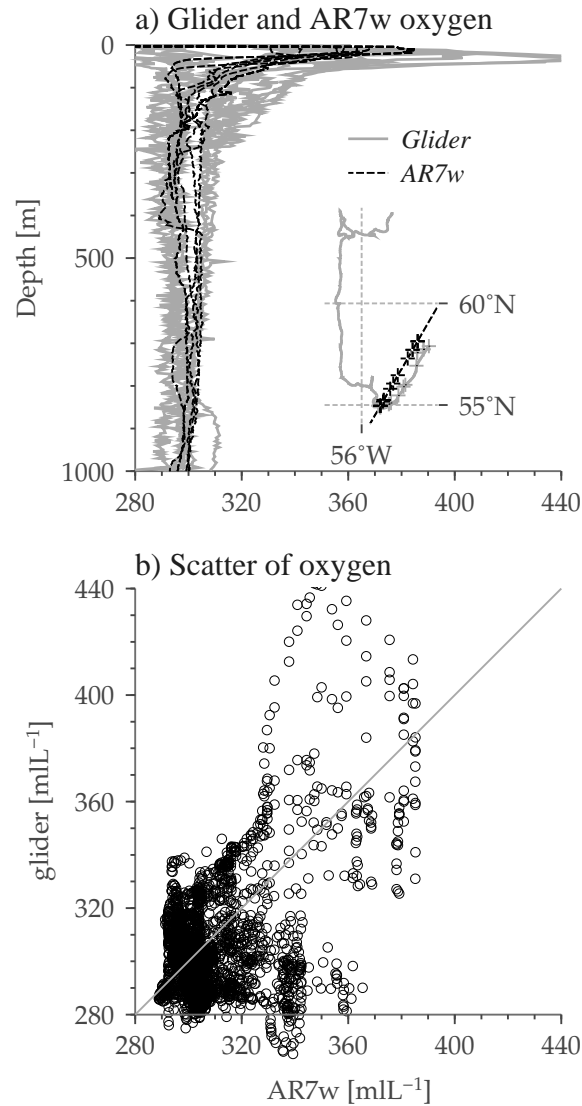


Figure 2.2: Seaglider oxygen electrode measurements calibrated against measurements taken during the AR7W repeat hydrography section. (a) Calibrated Seaglider (gray, solid) and ship cruise measurement profiles (black, dashed) are paired based on minimal distance in time and space (within 50 km and 2 weeks). Profile locations are shown at crosses on the inset map—black is the AR7W cruise, gray is the glider track. (b) Scatterplot of glider oxygen against AR7W oxygen, with $r^2 = 0.31$ for a linear fit between the two and rms-difference of $19 \mu\text{mol L}^{-1}$. Each point represents a pair of measurements from a cruise profile and glider profile, from the same depth. The largest divergences between Seaglider and ship measurements are in the surface layer.

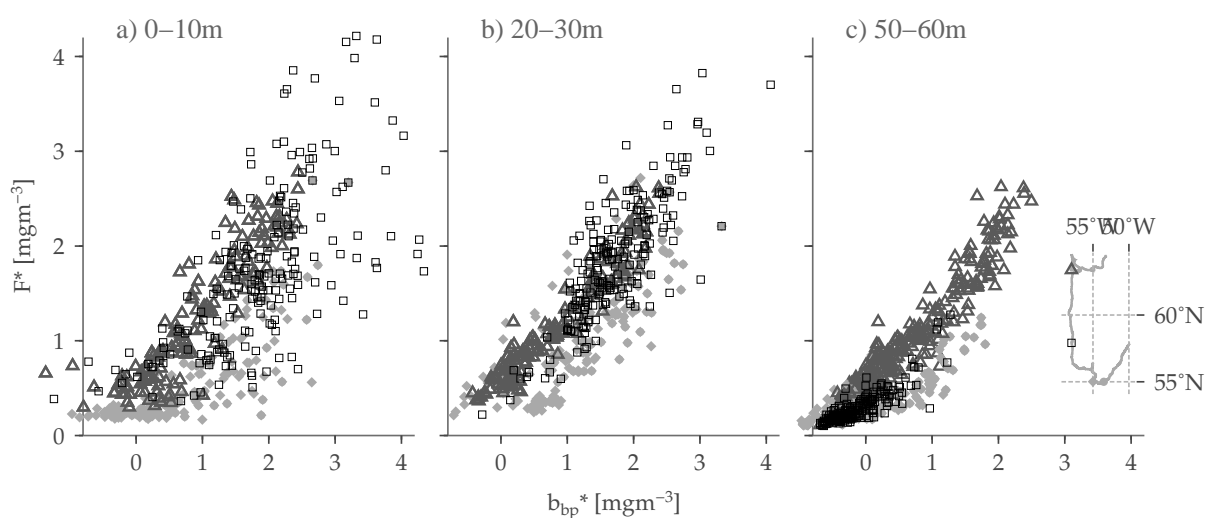


Figure 2.3: Scatterplots of fluorescence bloom intensity (F^*) vs. b_{bp} bloom intensity (b_{bp}^*) for profiles from 4 productive regions, the north slope, central Labrador Sea, Labrador shelf thin layer and shelf-break front (indicated by symbols along the track in the inset map). The first two regions (black triangle and black square) are mixed-layer blooms while the second two are subsurface (gray diamond and circle). Observations were binned by depth: (a) 0-10 m, (b) 20-30 m, (c) 50-60 m. At the surface (a), F^* and b_{bp}^* are high, with large spread (loose correlation) especially in the Labrador slope region (\square). In deeper bins, the relationship between F^* and b_{bp}^* is tighter. By 50-60 m (c), only the north bloom (\triangle) has high values.

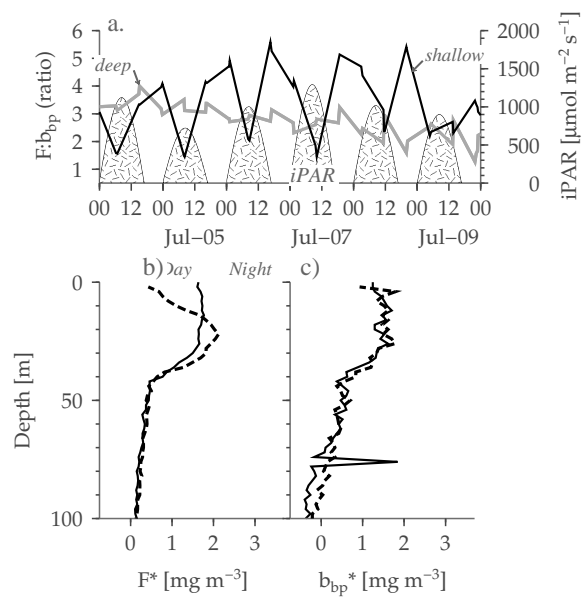


Figure 2.4: a) Near-surface (0-10 m, black line) and deeper (20-30 m, gray line) values of fluorescence-to-backscatter ratio $F:b_{bp}$, and SeaWiFS $iPAR$ (instantaneous incident light, hatched regions, described in §2.2) for July 4-9, 2005. Lower surface $F:b_{bp}$ ratios are observed during the day (higher $iPAR$), indicative of fluorescence quenching. (b) Day and night vertical profiles of F^* and b_{bp}^* show the depth range over which fluorescence is quenched (0-30 m), while b_{bp}^* is relatively constant in the surface layer.

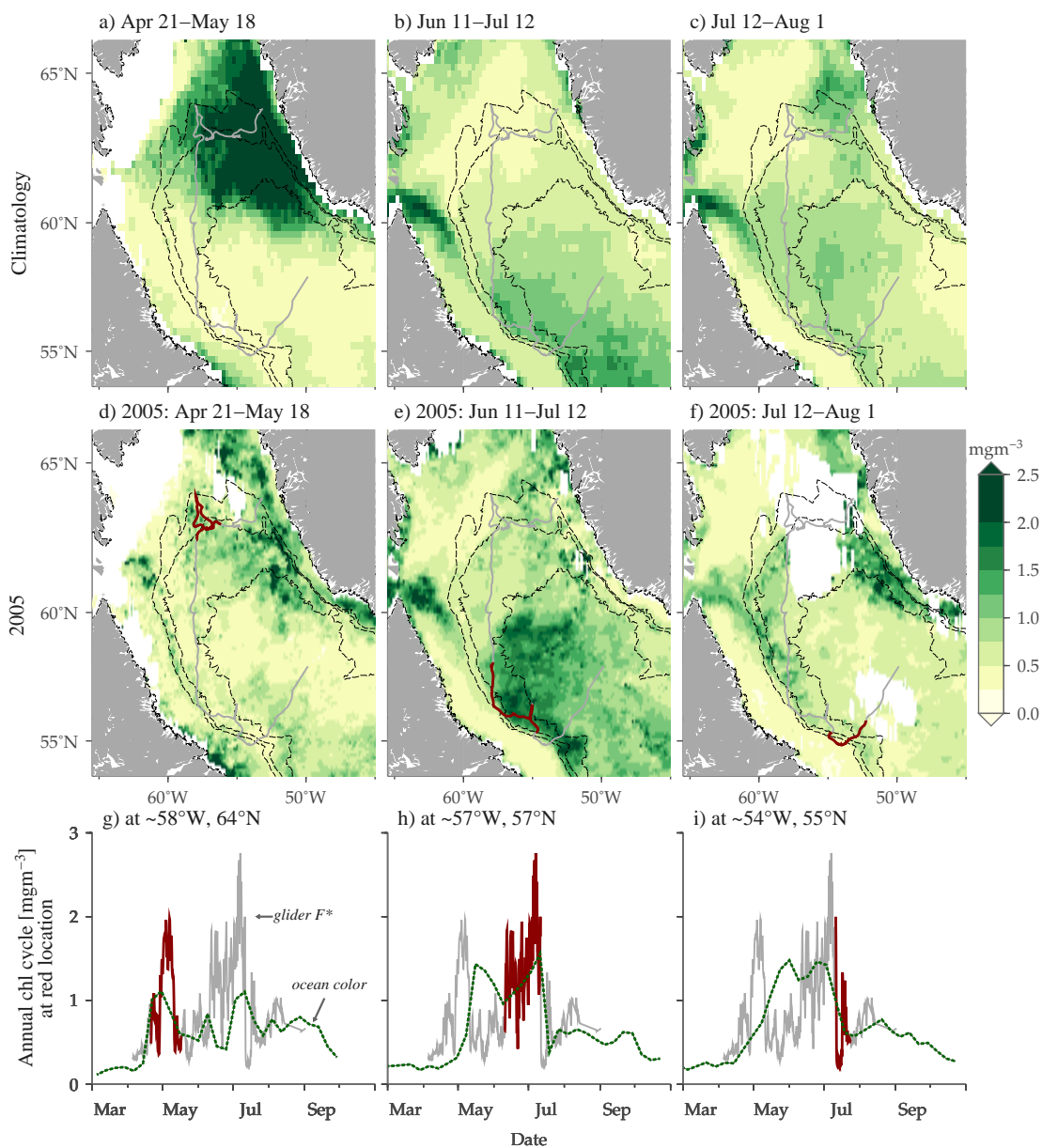


Figure 2.5: Comparison of climatological and 2005 surface chlorophyll (rows 1: a-c and 2: d-f, with glider track marked in gray), and glider chlorophyll measurements in the top 20 m with SeaWiFS chlorophyll annual cycle (row 3: g-i). The three time periods for each column are roughly one-month long and correspond to the glider location highlighted in red in row 2. In this way, the spatial pattern of chlorophyll while the glider made a single track of measurements is revealed. For the annual cycles in row 3, SeaWiFS chlorophyll (green) is from the location in row 2, allowing a direct comparison between Seaglider measurements and SeaWiFS where the Seaglider chlorophyll is highlighted in red. Row 3 shows when the Seaglider measured chlorophyll relative to the local bloom timing. From (g) the glider observations during this region and time were during the local peak and decline of the bloom. From (h) the glider observed a secondary peak for this region. From (i) the glider made observations after the local peak bloom had declined.

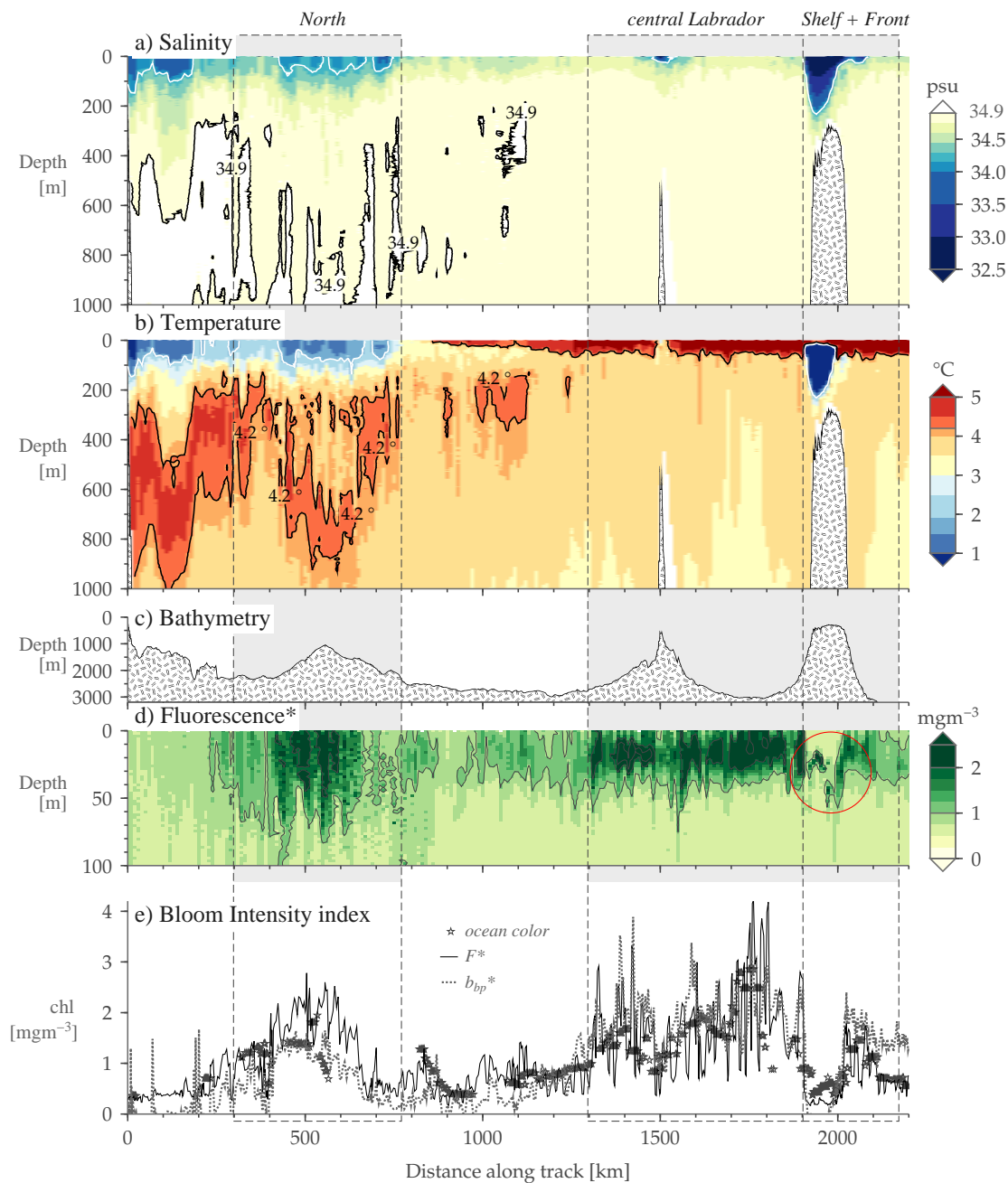


Figure 2.6: The entire section of Seaglider salinity (a) and potential temperature (b) to 1000 m, underlying bathymetry along the track (c), fluorescence bloom intensity to 100 m (d) and bloom intensity indices (e). High-fluorescence regions along the track are highlighted in gray: the north bloom (300-800 km), central Labrador (1300-1900 km) and Labrador shelf and front (1900-2000 km). The north bloom has a watermass signature similar to the West Greenland Current (fresh surface, and subsurface core of warm, salty Irminger Sea Water). The central Labrador has a warm surface layer. The Labrador shelf is very cold and fresh. (d) The thin layer on the Labrador shelf is circled in red on the fluorescence panel. (e) Ocean color within 2 days and 0.5 degrees of the glider surfacing locations are included on the plot of F^* and b_{bp}^* .

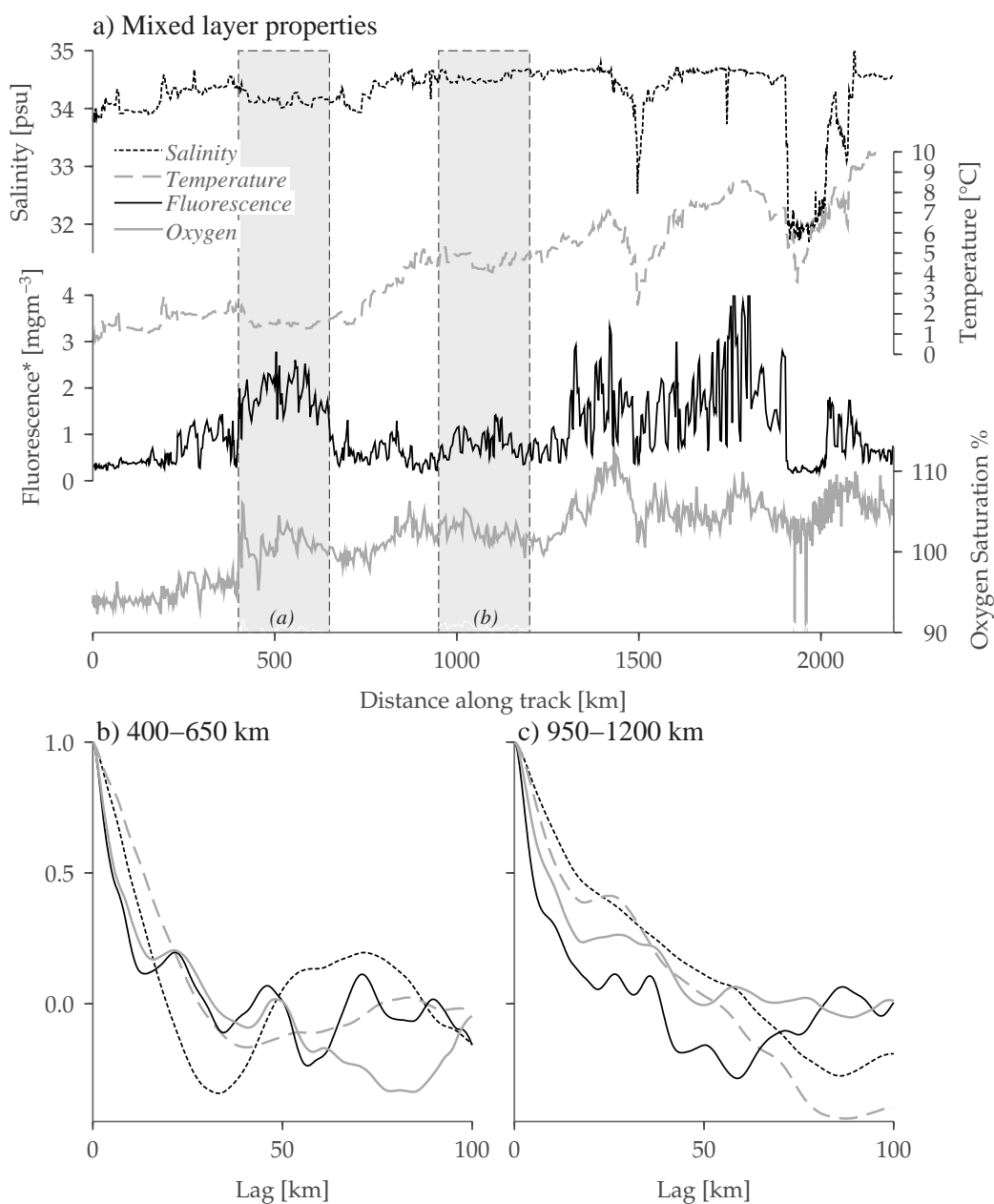


Figure 2.7: Auto-correlations between mixed-layer properties. Panel (a) shows the mixed-layer salinity, temperature, fluorescence and oxygen saturation for the entire Seaglider 16 record. Panels (b) and (c) are lag correlations as a function of distance along track for each variable, within two regions (shaded in panel (a)), the north Labrador bloom and part of the early central Labrador bloom. In the north bloom, where mesoscale eddies of diameter ≈ 20 km were present, all properties decorrelated more quickly. In the central Labrador Sea, biological properties decorrelate much more rapidly than salinity or temperature. Temperature in particular was affected by seasonal warming so that, later in the season, decorrelation length scales increase to 100 km (not shown).

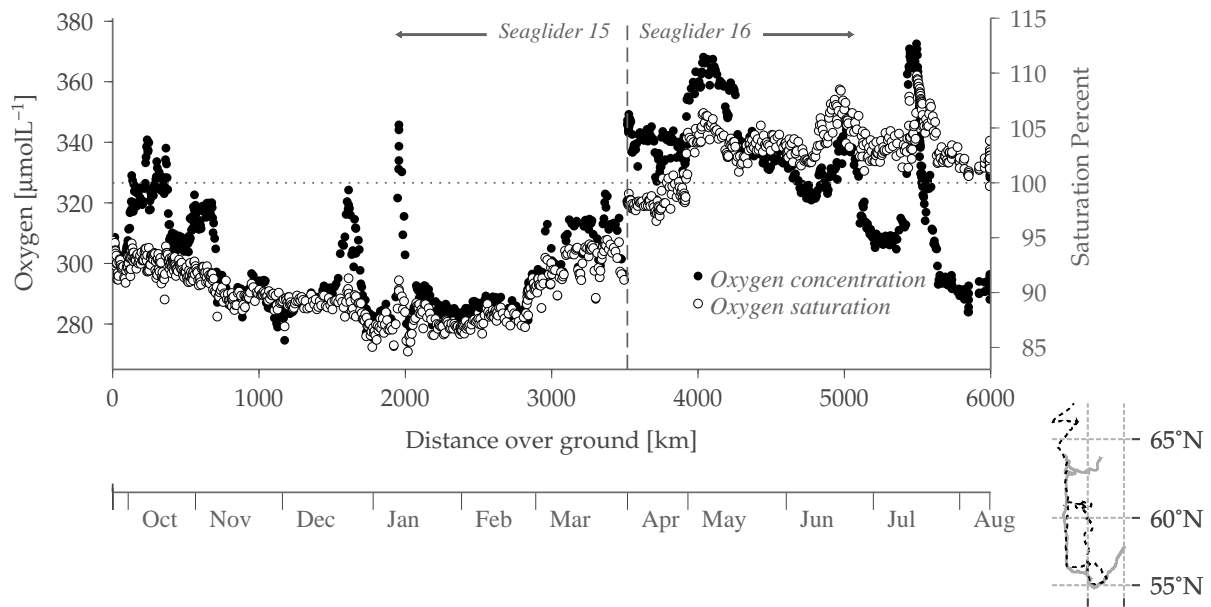


Figure 2.8: Surface (0-40 m) time/space series of oxygen concentration and saturation measured by Seaglider 15 (October 2004-March 2005, dashed track in inset map) and Seaglider 16 (April - August 2005, solid track in inset map). In the winter Labrador Sea, productivity is absent or very low due to low light levels. During deep convection (January through March), surface waters are mixed with oxygen-depleted waters below, decreasing saturation to 10% subsaturated. During the spring bloom, oxygen levels soar, becoming supersaturated by 5-10% at the end of April, and remaining supersaturated through the end of the record (mid-August). Though supersaturated everywhere in spring, oxygen concentrations decrease from April to August due to warming.

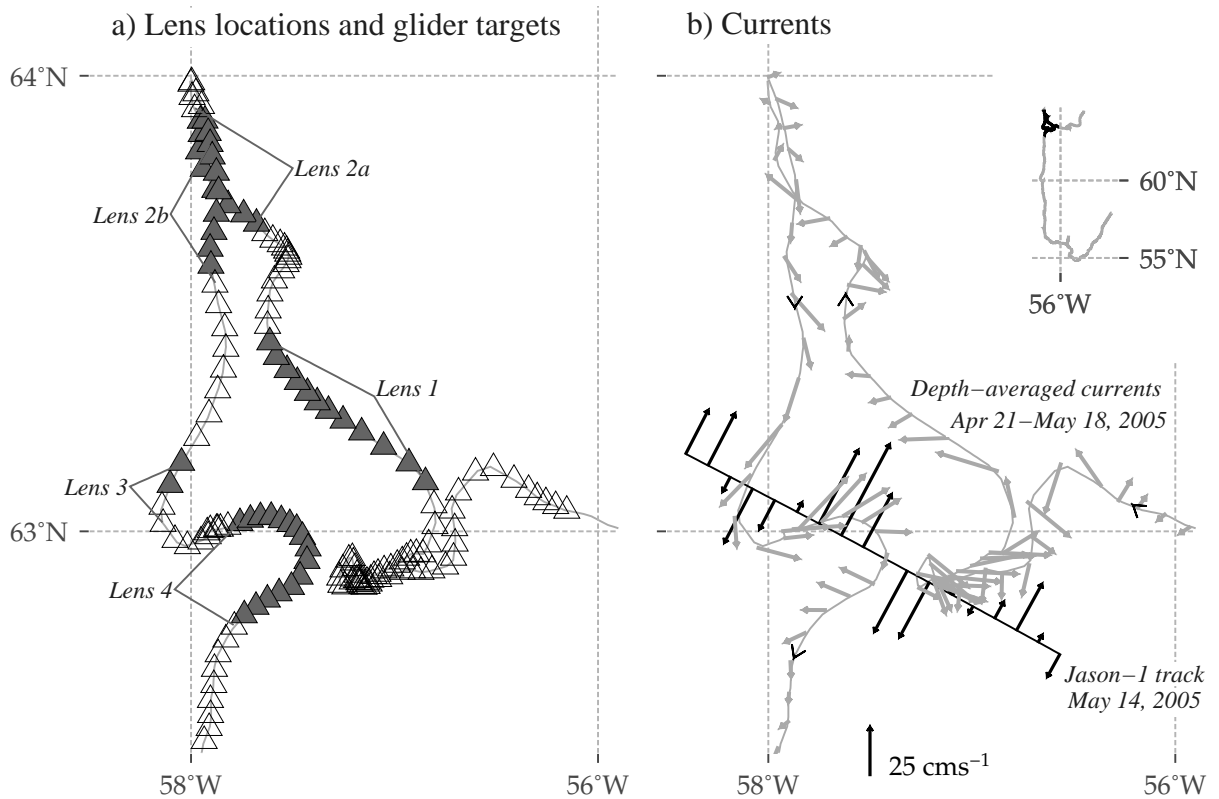


Figure 2.9: Spatial map of glider observations of 4 fresh lenses and surface velocities. (a) Each profile is marked by a circle. Gray triangles are within fresh lenses, open triangles are outside lenses. From this map, lens 2a and 2b are the same physical feature. (b) Glider-estimated 0-1000 m depth-averaged currents (gray arrows) and surface geostrophic velocities from an along-track-gridded altimetry section (black arrows) show the anticyclonic lens 4. Glider direction of travel is shown by the small black arrowheads along the track. Along this survey, the glider was deflected from straight lines to the west, northwest then south directions by ocean currents.

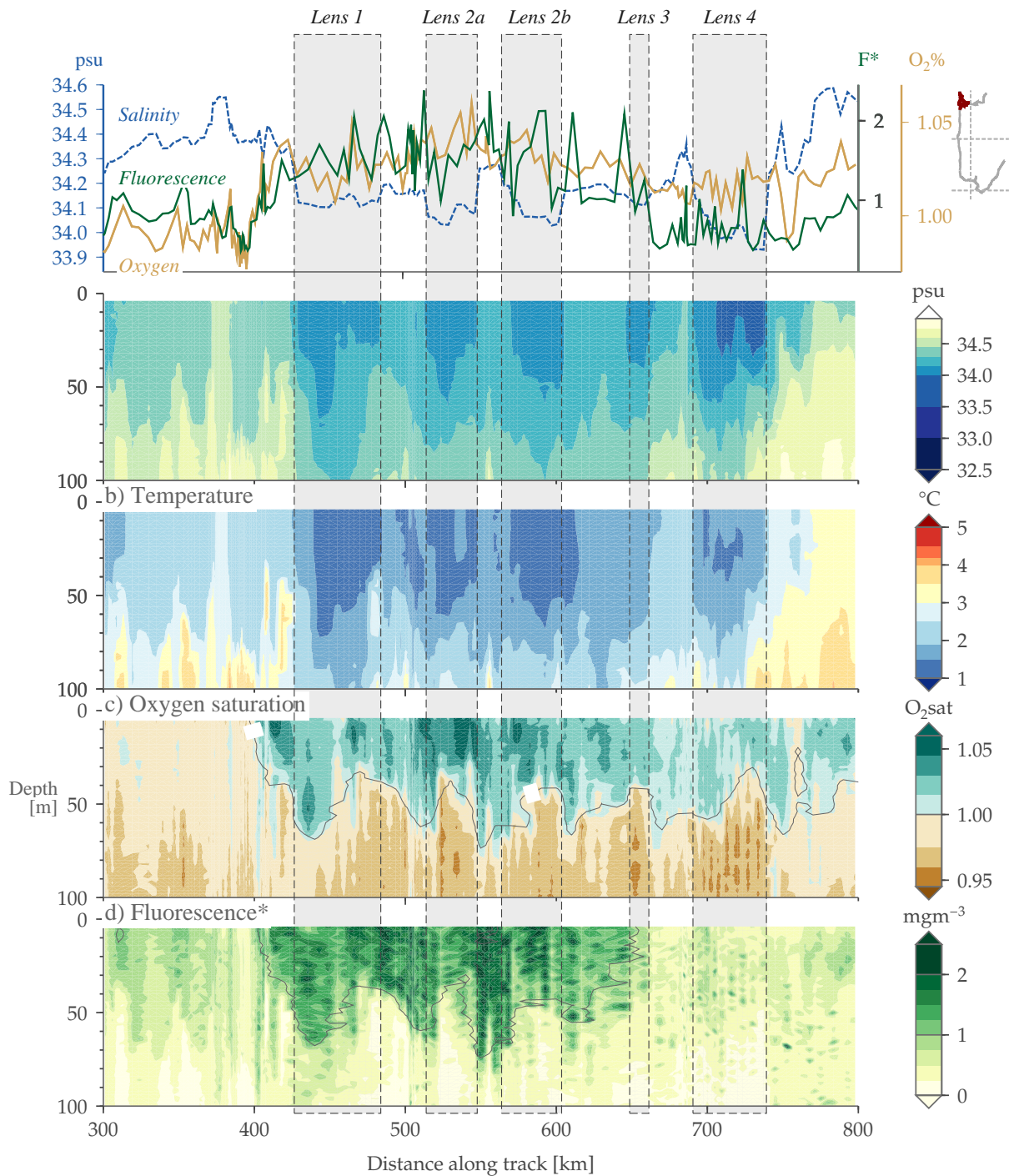


Figure 2.10: Hydrography and biological data from Seaglider in the north bloom: salinity (b), potential temperature (c), oxygen saturation (d), and fluorescence bloom intensity, F* (e). Highlighted in gray are five observations of four fresh and cold lenses. Higher F* and oxygen saturation values are seen in lenses 1 and 2. Additionally, oxygen is elevated in lenses 3 and 4. (a) While F* is higher in the lens region than the 100 km at the beginning of this plot, some of the highest F* values are observed at the edges of lenses 1 and 2a, and lenses 2a and 2b.

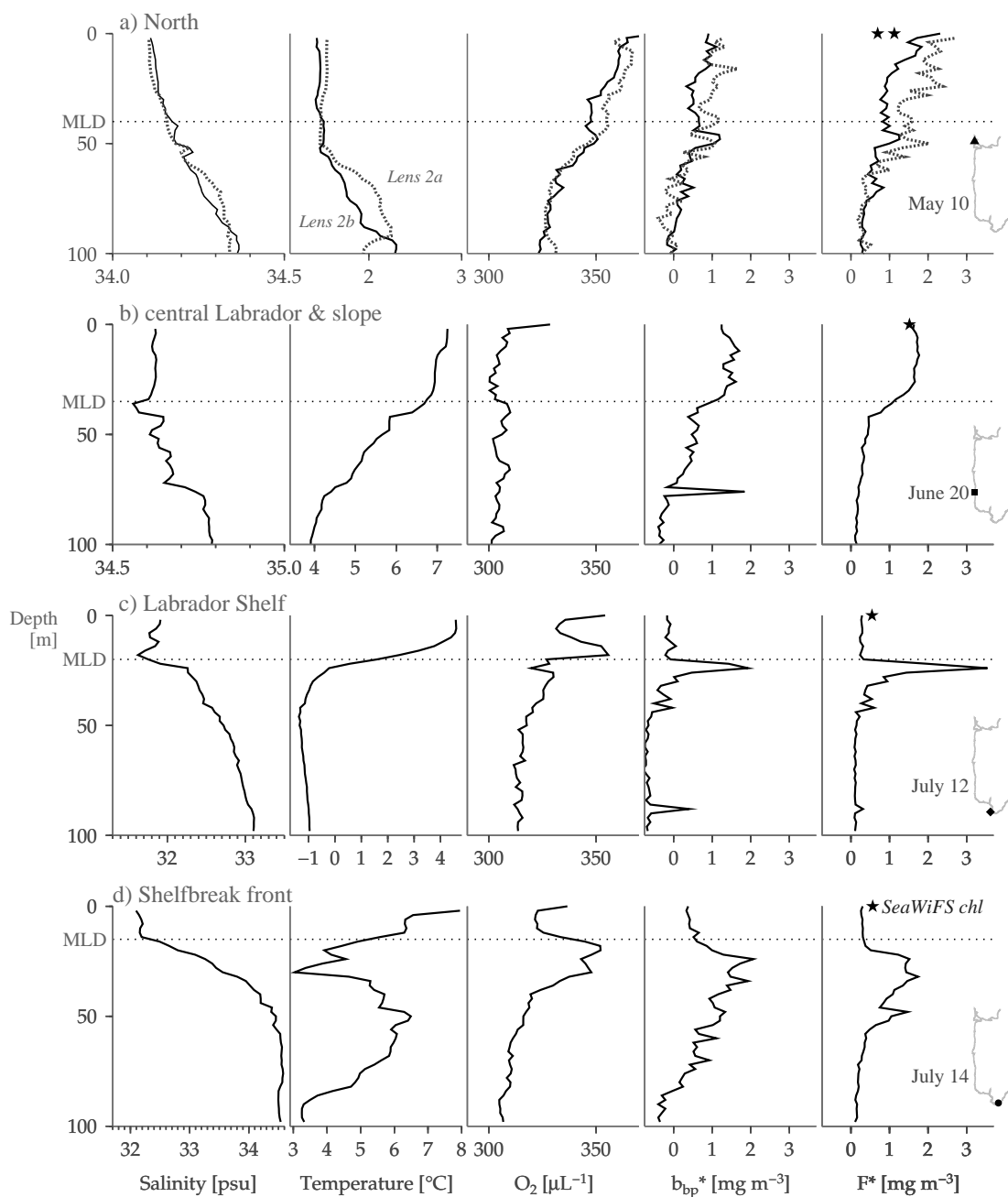


Figure 2.11: Vertical profiles of salinity (column 1), potential temperature (column 2), dissolved oxygen (column 3), backscatter-derived bloom intensity (column 4) and fluorescence-derived bloom intensity (column 5) for the four productive regions: north slope (row 1), Labrador slope (row 2), Labrador shelf and thin layer (row 3) and shelf-break front (row 4). Mixed-layer depths are indicated by the dotted lines. Inset plots show the glider track, profile position and the date the profile was taken. For the north slope, profiles are in lens 2a (dotted) and 2b (solid), to show the similarity of properties there. SeaWiFS chlorophyll estimates at the time and location nearest the glider profile are shown at the surface in the fluorescence plot (column 5) as black stars.

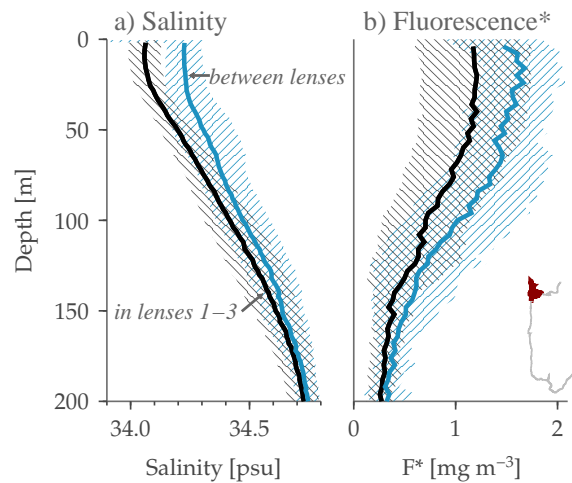


Figure 2.12: Mean vertical profiles of (a) salinity and (b) fluorescence bloom intensity inside (black) and at the edges of (blue-gray) lenses 1-3 in the north region. Lower salinities are in the lenses by definition, while higher average F^* values are at the edges of the lenses. Shaded regions around the profiles indicate one standard deviation.

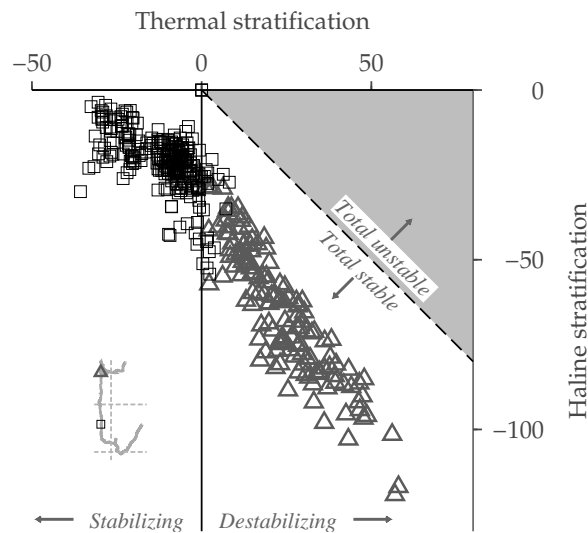


Figure 2.13: Buoyancy anomaly to 250 m due to salinity and temperature shows the relative contributions of haline and thermal stratification. Negative buoyancy anomaly is stabilizing, positive destabilizing. Total buoyancy anomaly is indicated by the distance of a point from the dashed line labeled “Total unstable/total stable”. Triangles are for the north bloom region while squares are the central Labrador. In the north region, salinity stabilizes in the presence of very cold, otherwise destabilizing surface temperatures. In the central Labrador, both temperature and salinity are stabilizing.

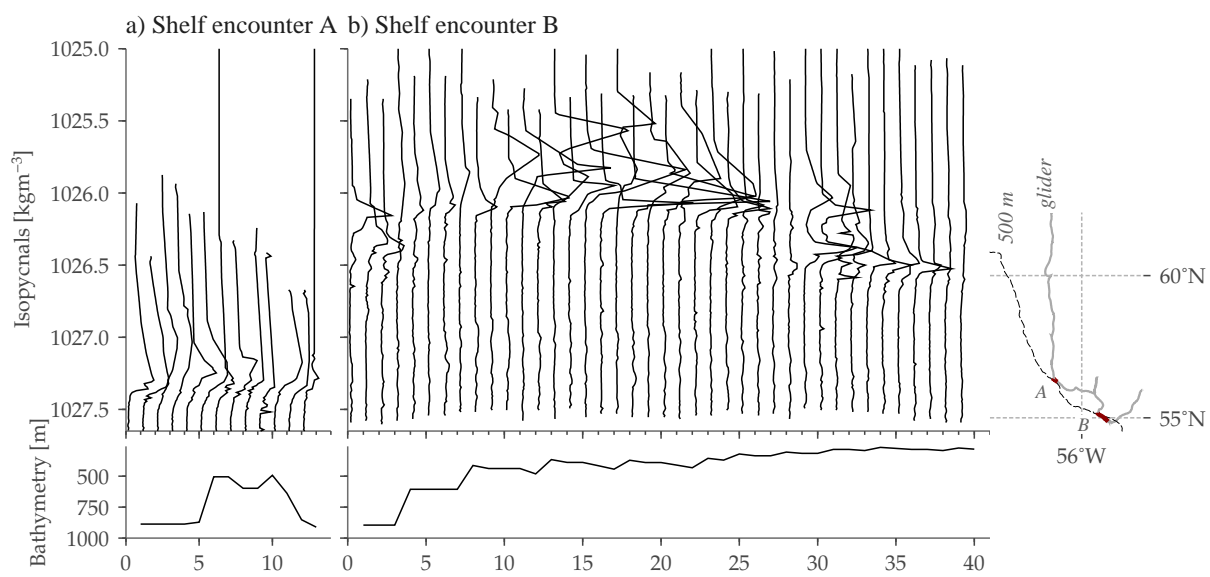


Figure 2.14: Fluorescence bloom intensity on isopycnals during the first shelf crossing (a) and second shelf crossing (b). The lower panels show the bottom depth beneath each glider profile. The inset map shows the glider track, the 500 m isobath and the two excursions onto the shelf.

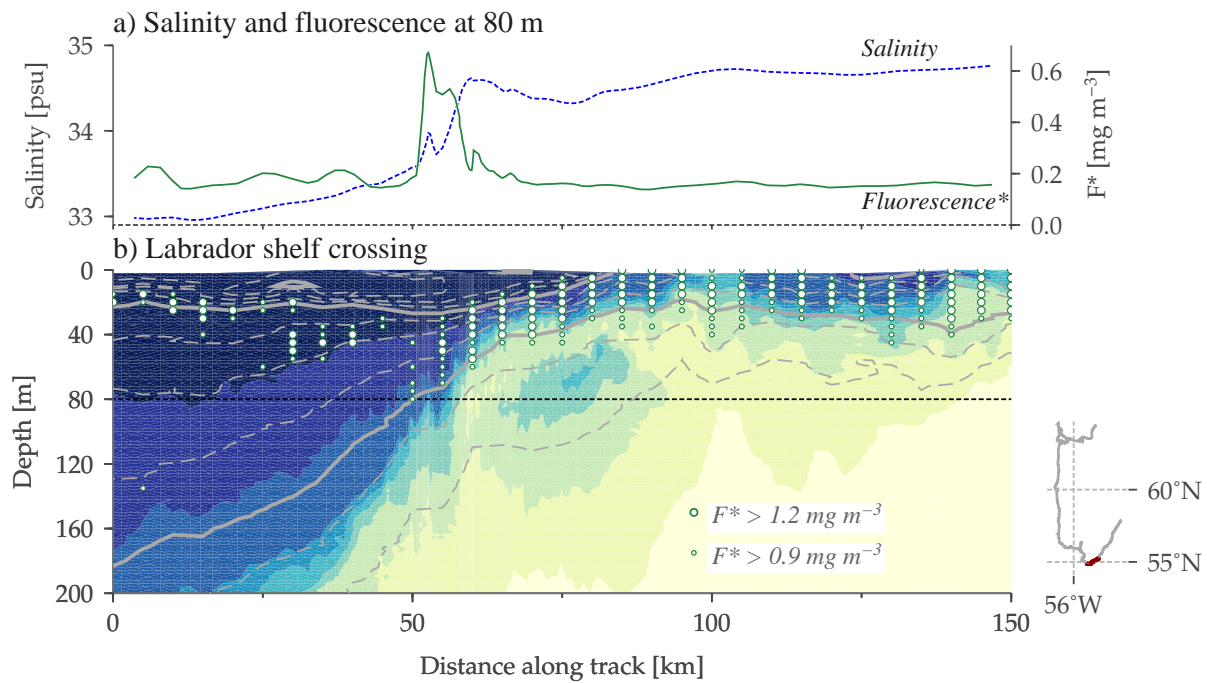


Figure 2.15: Salinity (shaded and solid line) and fluorescence bloom intensity (circles and dashed line) at the shelf-break front. (a) Line plot of salinity and F^* at 80 m depth shows the relative position of the front (high gradient in salinity) and peak fluorescence. (b) The Labrador current is on the shelf, and very cold and fresh. Density contours of 1 kg m^{-3} (thick gray) and 0.25 kg m^{-3} (thin dashed gray) are marked. Fluorescence bloom intensity was gridded to 5 km along track and 5 m in depth for plotting purposes. Large circles indicate $F^* > 1.2 \text{ mg m}^{-3}$; small circles indicate $F^* > 0.9 \text{ mg m}^{-2}$. From 75 m along the track (1000 m water depth), F^* is in the surface 40 m, while on the shelf (0-50 km along track), F^* is elevated in the thin layer at 20-30 m depth. At the front (50-75 km along track), high F^* to 80 m is observed on the 34 psu isohaline.

Chapter 3

PHYSICAL CONTROLS ON THE INTERANNUAL VARIABILITY OF THE LABRADOR SEA SPRING PHYTOPLANKTON BLOOM USING SEA-VIEWING WIDE FIELD OF VIEW SENSOR (SEAWIFS)

3.1 Summary

The spring phytoplankton bloom in the north Labrador Sea varied in intensity by a factor of 4 and in timing of onset by 3 weeks over the 11-year record from SeaWiFS satellite ocean chlorophyll, 1998-2008. This north bloom (north of 60°N and west of the Labrador shelves) is earliest and most intense, owing in part to the offshore-directed freshwater stratification from the West Greenland Current. On interannual timescales, significant correlations were found between variability of bloom intensity and physical processes, namely the offshore freshwater advection, eddy activity and river and ice melt runoff from Greenland. In contrast, the central Labrador Sea is later and weaker. No physical indicators for bloom intensity were found for this region, and 50% of its onset variance could be explained by surface irradiance. As the subpolar gyre shifts in strength and shape, freshwater outflow from the Arctic and Greenland change, we may expect further changes in the biological response as indicated by these relationships.

3.2 Introduction

Oceanic phytoplankton produce about half of the atmosphere's oxygen and form the basis for the oceanic food web. With SeaWiFS chlorophyll, it is possible to look at the dynamics and spatial structure of the spring bloom in remote areas such as the Labrador Sea. The multiyear record (1998-2008) allows examination of connections between chlorophyll activity and natural physical variability, as well as a first look at possible responses to global warming trends. *In situ* observations identify the importance of the buoyant surface layer in the Labrador Sea spring bloom (Frajka-Williams et al., 2009). Freshwater in the subpolar North Atlantic is highly sensitive to global change,

and one of the focuses of this paper.

The spring phytoplankton bloom in the subpolar North Atlantic dominates the annual cycle of chlorophyll. In the western subpolar gyre winter, deep mixing replenishes surface nutrients, likely from Antarctic Intermediate Water (Lévy, 2005), but light limitation restricts growth. This contrasts the oligotrophic subtropical North Atlantic where the annual cycle of surface irradiance is reduced, and nutrient levels in the subsurface reservoir are lower. With the arrival of spring, mixed-layers shoal and irradiance increases. The bloom begins once photosynthetic production exceeds losses. Eventually, the bloom is arrested by competition for nutrients or pressure from grazer populations, peaks and declines.

Both the timing and magnitude of the bloom affect the transfer of energy to higher trophic levels (Townsend et al., 1994). The match/mismatch hypothesis between predator and prey cycles states that the survival of higher trophic levels with time-varying life stages depends on food availability at critical periods (Conover et al., 1995). The magnitude of the bloom, measured as peak bloom or integrated productivity over the duration of the bloom, quantifies the transfer of energy from sunlight to chemical energy, and the amount of energy available to higher trophic levels.

Several physical effects are known to impact bloom timing or productivity, primarily light and stratification (Sverdrup, 1953). Their effect can be inferred from the description of the North Atlantic spring bloom above, that shallower mixed layers or more light result in an earlier bloom. Additional factors affect overall production. Light and nutrient availability and the absence of grazers enhance the biomass production. Nutrient availability in the North Atlantic is a result of deep wintertime mixing but can also be enhanced by vertical mixing. Recent studies have shown the importance of mesoscale eddies in the oligotrophic, subtropical gyre (McGillicuddy et al., 1998; Siegel et al., 1999; McGillicuddy et al., 2007), though the same eddy effects were shown to have an opposite effect in the Labrador Sea (McGillicuddy et al., 2003). Species composition of a phytoplankton population also affects production rates. Some phytoplankton are more efficient producers at low light or nutrient levels than others.

In the Labrador Sea, the importance of bloom timing and transfer of energy to higher trophic levels is especially important. Recruitment of copepods, the most abundant mezozooplankton in the region, depends on the supply of food (Head et al., 2000). Labrador Sea food chains tend to be short, enabling a description of the relationship between higher consumers such as cod, whale and bird

populations to primary production (Conover et al., 1995; Laidre et al., 2007, 2008). Interestingly, while the general pattern of bloom timing in the North Atlantic tends to be earlier at lower latitudes and later at higher latitudes (Siegel et al., 2002), this pattern is reversed within the Labrador Sea (Head et al., 2000). An early explanation of the reversal was offered by Head et al. (2000), that ice melt from icebergs in the north Labrador Sea resulted in high stratification. The importance of stratification for the north bloom was also identified in a recent study using a numerical model to recreate bloom timing patterns (Wu et al., 2008), and from coincident hydrographic and bio-optical measurements from a Seaglider during the 2005 spring bloom (Frajka-Williams and Rhines, 2008). Bloom timing also indicates distinct biogeographical zones.

Broadly, the Labrador Sea has been divided into two biogeographical zones, representing distinctions in watermass properties and biological species (Longhurst, 2007; Devred et al., 2007). The primary zone is the Atlantic Arctic in the deep Labrador Sea (> 2000 m), characterized by high winter nitrate in the mixed layer ($\sim 15 \mu\text{mol}$), an early bloom dominated by *Phaeocystis pouchetii*, followed by diatoms. The second zone is the Boreal Polar, corresponding to the cold, fresh Arctic waters on the shelves. For mesozooplankton, the shelves are dominated by *Calanus hyperboreus* (consistent with Boreal Polar) while the Greenland slope and north Labrador Sea have *C. finmarchicus*, and the central Labrador Sea, *E. norvegica* (consistent with Atlantic Arctic) Head et al. (2003). In the Irminger Sea, satellite and hydrographic-based studies showed that different zones have different bloom timing, due to population composition, mixing and stratification effects (Holliday et al., 2006; Henson et al., 2006). In this paper, we explore biogeographical regions within the Labrador Sea using both SeaWiFS chlorophyll and distinctions in dominant physical controls between regions.

The Labrador Sea is the western edge of the subpolar gyre of the North Atlantic (Fig. 3.1a). The general circulation within the Labrador Sea is cyclonic, characterized by doming isopycnals and layers of distinct watermasses in the boundary currents. The boundary currents and shelves are capped by very fresh, very cold water of Arctic origin. Extending from 200 to 800 m deep, encircling the Labrador Sea, is warm, saline Irminger Sea Water of subtropical origin. Labrador Sea Water formed during deep convection fills the central Labrador Sea from near the surface to 2500 m depth. Deeper lie Northeast Atlantic Deep Water and Denmark Strait Overflow Water which, together with Labrador Sea Water, make up North Atlantic Deep Water. Boundary currents are concentrated at

the slopes by the Greenland and Labrador sides. Offshore advection around the northern edge of the Labrador basin occurs in two or more diffuse branches (Fig. 3.1b). Deep waters are forced offshore by shoaling topography near the 3000 m isobath. This boundary current separation is visible as an eddy-kinetic-energy maximum (Fig. 3.1b). Further outflow from the Greenland slope occurs near the 1000 m isobath. Within this offshore advection are found Irminger Rings, coherent mesoscale eddies which are characterized by the fresh shelf waters at the surface and Irminger Sea Water at intermediate depths.

In this paper, we quantify the climatological pattern of bloom magnitude and timing (§3.4) and interannual variability in the bloom (§3.5) as described by chlorophyll. The relationship between boundary currents and the Labrador Sea interior turns out to be crucial to bloom dynamics. In both sections, we further discuss the physical controls on the bloom pattern and variability, first using Sverdrup's hypothesis then with measures of bloom and physical processes. We summarize the results and discuss implications in §3.6.

3.3 Data

The domain for most of the study is the black box in Fig 3.1: 54° to 66°N and 38°W to 65°W.

3.3.1 Satellite ocean color

Ocean surface color measured by satellites is converted to an estimate of chlorophyll-*a* concentration via an empirical algorithm (Feldman and McClain, 2006). The raw satellite signal is modulated by atmospheric effects, and affected by phytoplankton size and species, minerals and dissolved organic matter, resulting in an estimated error on chlorophyll of $\pm 35\%$. We used OCV4 SeaWiFS daily, 9 km resolution mapped chlorophyll, photosynthetically active radiation (PAR) and attenuation coefficient at 490 nm (K_{490}) from 1998-2008. At 60°N, low incident sun angle in the winter results in no data prior to February and after October. For all analyses except the plots in Fig. 3.6, data were binned to $0.5 \times 0.5^\circ$ resolution. Calculating annual cycles at a point, time series were first smoothed with a 3-day moving average.

3.3.2 Climatological hydrography

With the World Ocean Atlas 2005 (WOA05) climatology product, we characterized the annual cycle of mixed layer depths and nutrients in the Labrador Sea. Mixed layer depths were calculated using a density threshold. Density profiles were linearly interpolated to 20 m resolution in depth. The mixed layer depth was defined as the shallowest depth which had a density greater than the density in the surface 20 m bin by at least 0.1 kg m^{-3} .

3.3.3 Satellite altimetry

Gridded geostrophic velocity products derived from satellite altimetry were produced by Ssalto/Duacs and distributed by Aviso with support from Cnes. The delayed time reference product uses either TOPEX/Poseidon and Jason-1 or EnviSat and GeoSata altimeters, and objectively maps sea surface height anomalies to a $1/3^\circ$ resolution grid, weekly starting in 1992. For absolute velocity, a background mean dynamic topography was added to the anomalies before calculating velocities. In both cases, velocities are calculated as surface geostrophic ocean currents (u zonal and v meridional currents). We used the absolute velocity product when describing circulation in the Labrador Sea and velocity anomalies when calculating eddy-kinetic-energy (EKE),

$$EKE = \frac{1}{2} (u^2 + v^2) . \quad (3.1)$$

Offshore geostrophic velocities representing the offshore-directed branch of the subpolar gyre were estimated by averaging velocities perpendicular to the line in Fig. 3.8, with positive values to the southwest (in the direction of the gyre mean circulation). While the absolute velocities were used, and the position of the subpolar branch depends heavily on the background mean dynamic topography, for our calculations we are looking at interannual variability, which is not affected by the mean.

3.4 Methods & Results: Climatology of the Bloom

3.4.1 Relative bloom magnitude & phase

Maps of mean chlorophyll, averaged for 1998-2008, identify two regions with highest concentrations: the north Labrador Sea and Hudson strait outflow (Fig. 3.2a). Here, the north Labrador Sea

refers to the region north of 60°N and east of 58°W , including both deep water areas (over 3000 m of water) and the Greenland shelf. The Hudson outflow signal is concentrated in the crescent shape at 60°N and 62°W , and is reminiscent of fresh river plumes in the northern hemisphere. The potential vorticity waveguide of the continental shelves direct the paths of shelf currents. In the case of buoyant river plumes, Coriolis causes them to turn right along the coast. However, the Hudson outflow first crosses the shelf to the shelf-break before turning right. The turning position may be determined by bottom Ekman stress balancing pressure gradients (Chapman and Lentz, 1994), though the theory does not account for the second observed front, between the coast and the outer front, which also reaches the shelf-break before turning but with a different radius. High chlorophyll concentrations in the plume persist longer than in any of the other Labrador Sea bloom regions, possibly due to a consistent nutrient supply in the tidally-mixed Hudson Strait waters (Straneo and Saucier, 2008).

Differences in bloom phasing indicate dynamically distinct regions. Bloom start day was calculated following Siegel et al. (2002) and Henson et al. (2006). For a given year ($year_0$), the start day ($start$) at a location is defined as

$$start(year_0) = \min_{t \in year_0} \{chl(t : t + 3) > 1.05 \times \text{median}_{t \in year_0} \{chl(t)\}\} , \quad (3.2)$$

where chl is chlorophyll concentration in $mg\ m^{-3}$ and t is time in days. In words, the start day is the first day when chlorophyll values exceeded the annual median at that location by at least 5%, and remained elevated for the 3 subsequent days. Median start day for the 11 year record reduced skewing by cloudy years (when cloud cover at the start of a bloom results in missing data and a delay in the calculated start day) and is shown in Fig. 3.2b.

The overall pattern of bloom timing is that the north bloomed in the spring (April-May), central Labrador Sea later (June), and the Labrador shelves latest (June-July). The north bloom initiated nearly synoptically, covering the entire region within a 2 week period. The central Labrador Sea region, centered at 58°N and 55°W , bloomed near the Labrador shelf then spread to the east and north. Annual cycles for two bloom regions are shown in Fig. 3.3a, allowing a direct comparison of bloom peak and start between regions. The north region has an early (late April) and very strong bloom, followed by a second peak in June-July. The second location in the central Labrador Sea has a later, larger bloom in July. The last regions to bloom were the Labrador shelves and Hudson outflow. In some cases, when the shelf bloom was especially brief, our criterion for the bloom start

day mis-identifies the shelf bloom. A Seaglider observed these same bloom regions in chronological order for the bloom in 2005, describing vertical profiles of fluorescence and coincident physical properties (Frajka-Williams et al., 2009). The different phasing between these four regions suggests different dynamics.

3.4.2 Relating phase to physical properties

Sverdrup's critical depth theory predicts the timing of a spring bloom from physical properties (Sverdrup, 1953; Siegel et al., 2002; Henson et al., 2006). The theory balances depth-integrated production and respiration to estimate a critical depth for a bloom. Once the mixed layer depth is shallower than the critical depth, a bloom may begin. While the classic theory uses a simple parameterization of photosynthesis in terms of surface incident light (PAR) and exponential light attenuation (k), and an assumed-constant respiration rate, it was found to be sufficient to describe the overall pattern in the Labrador Sea. Following Siegel et al. (2002) and Henson et al. (2006), the critical depth is defined as

$$\frac{1}{kZ_{cr}} \left(1 - e^{-kZ_{cr}}\right) = \frac{PAR_c}{PAR}. \quad (3.3)$$

One crucial parameter is not measured *in situ*: compensation irradiance PAR_c . It is the light necessary for photosynthesis to exactly balance respiration (Miller, 2004). While PAR_c can vary with species, location and time, in absence of other measurements, we use $PAR_c=1.65$, a typical value for the region (Siegel et al., 2002). Since incident light (PAR) and mixed layer depth have annual cycles related to solar forcing and winter mixing, the bloom occurs when calculated critical depth intersects mixed layer depth. This is demonstrated for the Labrador Sea in Fig. 3.3b. Solid lines are mixed layer depth from Argo floats within the region. Dashed lines are estimated critical depth. Once critical depth intersects the mixed layer depth, the bloom in each region is predicted to begin. Indeed, these curves show the relative timing of the two blooms quite well.

Based on Sverdrup's model, three hypotheses may explain observed bloom timing from Fig. 3.2b:

- Hypothesis 1: Variations in light are responsible for the pattern.
- Hypothesis 2: Variations in stratification are responsible for the pattern.

- Hypothesis 3 (untestable with available data): Variations in species composition, nutrient availability or pressure from grazers in the different biogeographical regions affect bloom timing, e.g. *Phaeocystis ponchetti* can take advantage of lower light levels than can diatoms, and so blooms earlier.

The first two hypotheses were tested using mixed layer depths from the WOA05 and an annual time-series of PAR from SeaWiFS. Mixed layer depth cycles are linearly interpolated to match the higher horizontal and temporal resolution of the PAR product. Critical depth time series were calculated by solving equation (3.3) using the SeaWiFS PAR time series and constant PAR_c and k . The predicted start day at each location is the first day when the mixed layer depth is shallower than the critical depth.

For hypothesis 1, a single basin-wide average cycle of mixed layer depths was calculated. By using a uniform annual cycle for the whole Labrador Sea, we isolated the effect of light on the predicted startday (Fig. 3.4a). Over deep water, the predicted pattern of bloom initiation is latitudinal; lower latitudes bloom earlier because they receive more light. This latitudinal pattern contrasts with observed bloom start days: earlier in the north region than the central Labrador Sea (Fig. 3.2). In both the predicted and observed pattern, Labrador shelves bloom late. Sea ice constrains the Labrador shelf bloom since incident light is small until ice melts.

For hypothesis 2, critical depths were averaged to create a spatially uniform cycle. Mixed layer depth cycles varied spatially. In this scenario, the predicted shelf bloom is coincident with the north bloom, and much earlier than observed. Ice cover has been implicitly neglected by using a spatially uniform cycle of PAR. Since shelf waters are highly stratified year round, the predicted bloom is early. Over the deep Labrador Sea, the predicted phasing of the central and north Labrador blooms reflected the observed pattern: the north bloom is earlier than the central. We conclude that shallow mixed layers in the north permit the early bloom.

Combining hypotheses 1 and 2, that is, using spatially variable mixed layer depth and light cycles, the predicted start day pattern was calculated (Fig. 3.4c). In this calculation, the relative timing of the north, central and Labrador shelf (early, later, latest) blooms matched observed phasing. One difference remained just seaward of the Labrador shelf. In the observed pattern, this bloom is later than the north bloom, but earlier than the Labrador shelf and central blooms. In the predicted pat-

tern, the bloom is very early—at the same time as the north bloom. The skewed timing likely resulted from low horizontal resolution in the WOA05. Our method of linearly interpolating $1^\circ \times 1^\circ$ to higher resolutions spread the stratified shelf waters over the slope and deep water.

This test of Sverdrup’s critical depth theory showed that stratification was responsible for the north Labrador Sea spring bloom timing, while light controlled the central Labrador Sea bloom. To determine whether the stratification that causes the early north bloom was due to salinity or temperature, we calculated convection resistance, or surface-to-depth buoyancy anomaly, as in Bailey et al. (2005),

$$cr(S, T, h) \equiv \int_h^0 \sigma(S, T, z) dz - \sigma(S, T, h)h \quad (3.4)$$

where h is the reference depth, σ is the potential density and S and T are salinity and temperature. This quantity represents the amount of buoyancy (in units of kgm^{-2}) which must be removed in order to convect to the reference depth h . Negative values are stable. To separate the contributions of salinity and temperature, $cr(S_0, T, h)$ and $cr(S, T_0, h)$ are calculated, where S_0 and T_0 are fixed. Climatological buoyancy anomaly to 500 m in May is shown in Fig. 3.5. The north bloom region (north of 60°N) and the Labrador shelf are most stably stratified due to very stabilizing fresh water (Fig. 3.5b) in spite of destabilizing cold temperatures (Fig. 3.5c). The central Labrador Sea, by contrast, is beginning to be thermally stratified in May and is also weakly haline stratified. This stratification information combined with Sverdrup’s hypothesis demonstrated that in the climatological average, the north bloom is early due to haline (fresh) stratification, the central Labrador Sea blooms later once thermal warming increases, and the shelves are latest.

3.5 Methods & Results: Interannual Variability

3.5.1 EOF analysis of chlorophyll

A spatial timeseries of the interannual variability in the north bloom (April-May) is shown in Fig. 3.6. Maps of mean chlorophyll during April-May of each year show the range in peak and pattern of the bloom. The largest blooms over the 2000-3000 m isobaths (around 62°N and 54°W) are the 1998, 2002 and 2008 years. The 2002 bloom in particular was large and very concentrated. Other years, like 2003, were more confined to the Greenland shelf/slope area. Unfortunately, cloudiness affects the interannual signal in that clouds during the peak bloom may obscure the extent and

magnitude of the bloom.

To quantify interannual variability of the bloom we used empirical orthogonal functions (EOF) analysis on the deseasoned, detrended satellite ocean color data. EOF analysis identifies spatial regions which covary in time, which hopefully covary due to similar biological or physical forcings within the region. The technique is particularly fruitful for gappy data like SeaWiFS ocean color. To focus on interannual variability, seasonal cycles and interannual trends were first removed at each location prior to the analysis. Because EOF analysis does not necessarily identify physically meaningful patterns, varimax rotation was applied to improve the physical structure of the EOFs (Preisendorfer and Mobley, 1988). We then calculated homogenous correlation maps to ensure that the variability identified by the EOFs was intrinsic to the data. Homogenous correlation maps are calculated as a pointwise correlation between each principal component time series and the original time series at each location (Preisendorfer and Mobley, 1988). High correlations indicate that the EOF is representative at that location. When we refer to EOFs in the text, it is the varimax rotated pattern. Figures display homogenous correlation maps.

The first two EOFs explain 49% and 10% of the data (Fig. 3.7). The shape of these patterns does not directly reflect the climatology, since annual cycles were removed before calculating EOFs, but instead reflects the locations of high variability. Contours show positive correlations between the data and principal component time series. The first EOF is representative in the north region with maximal variability at 63°N and 54°W . Positive correlation also extends southward and slightly eastward to 56°N . The second EOF is representative of the central Labrador Sea region, concentrated between the 2000 and 3000 m isobaths between 55° and 58°N . The south-eastward extending branch of the first EOF is suggests the influence of mesoscale eddies, as the map of peak EKE in the Labrador Sea has a similar structure (Fig. 3.1b), while the second EOF includes the location of deep convection in the Labrador Sea (Pickart et al., 2002). Guided by these EOF maps and our results on physical conditions associated with the bloom climatology (§3.4.2), we related the interannual variability to physical forcing.

3.5.2 *Relating interannual variability in bloom characteristics to physical forcing*

What physical conditions and processes affect the interannual variability of the bloom? Physical effects that impact timing include light and stratification. In particular, haline stratification is responsible for the climatological north bloom timing. Eddies may influence nutrient availability, either positively or negatively. The offshore advection of freshwater by the subpolar gyre consists of the mean and eddy flow. Sources of upper ocean stratification in the region include local sea ice dynamics, melting from Greenland and changes in the Arctic outflow of freshwater. Global warming is increasing the supply of surface freshwater in the region, through increased ice melt of the Greenland ice sheet (Luthcke et al., 2006; Stearns and Hamilton, 2007; Hanna et al., 2008). Using indices to describe the state of these physical factors and bloom responses, we identified potential relationships between the bloom and physics.

We focused on two regions of high variability—the north and central Labrador Sea. Regions were chosen based on the EOFs in Fig. 3.7 and our understanding of distinct zones within the Labrador Sea from climatological bloom timing and magnitude (Fig. 3.8). For the north bloom, we used the region within 59-62°N and 52-54°W, corresponding to high variance in the EOF, the location of the offshore branch of the subpolar gyre (at the 3000 m isobath) and peak eddy-kinetic-energy. For the central Labrador Sea, the region is within 56.25-57.75°N and 54.5-57.5°W, corresponding to high variance in the second EOF and the location of deep convection.

Time series of the SeaWiFS chlorophyll averaged within each box are shown in Fig. 3.9. Comparing the two, the largest bloom years in the north region (1998, 2008) do not correspond to the largest bloom years in the central region (2004, 2007). The bloom in the north region is also larger, on average, than in the central region, which was clear in the annual cycles in Fig. 3.3, though the regions used are slightly different. The startday was fairly consistent between years in the north bloom, ranging from April 11 in 1999 to May 5 in 2008, a span of 24 days. The startday in the central Labrador Sea, on the other hand, ranged from April 27 in 1999 (during which year there was hardly a bloom to speak of) to June 3 in 2007, a span of 37 days. Notably in 2008, the entire Labrador Sea (north and central) bloomed together and early (Fig. 3.6).

Annual indices for bloom magnitude and timing were calculated for the two regions. Bloom timing was represented by average start day per year in the region. Bloom magnitude was described

by peak chlorophyll during the bloom and an integral of chlorophyll over the duration of the bloom. Duration was defined as the time from start day to end day, where the end day is the last contiguous day where chlorophyll was elevated above the threshold used for start day (5% above the annual median at that location). Peak and integrated-chlorophyll behaved similarly. Where they differ, the difference describes a change in shape of the bloom over time. When peak is elevated relative to integrated-chlorophyll, it indicates a more intense, short-lived bloom with steeper increase or decline. When peak is depressed relative to integrated-chlorophyll, it indicates a broader bloom in time. The bloom magnitude indices for the north bloom region are shown in Fig. 3.10a.

Annual physical indices were created to quantify light in both regions, and for the north region only, the offshore advection of freshwater, eddy-activity and Greenland runoff as well. Light was represented by the annual average of SeaWiFS PAR in each region. Lacking interannual time-series of stratification for the whole of 1998-2008, three proxies for freshwater were substituted: the offshore-directed branch of the subpolar gyre, eddies and runoff from Greenland (Fig. 3.10b and d). Mean offshore velocity was averaged from March through May directed perpendicular to the black and white diamonds in Fig. 3.8. While eddies travel at the mean background speeds, they are included as an additional proxy for freshwater since it is possible that they carry more freshwater than the background mean flow alone (Hátún et al., 2007). The eddy index was created by annually averaging eddy-kinetic-energy from sea surface height anomalies within the north bloom region. Annual estimates of Greenland runoff estimates were provided by Hanna et al. (2008) and Hanna, E (*pers comm*) from a meteorologically-forced numerical model.

The north bloom measures show the relationships between bloom start, duration, peak and integrated chlorophyll (Fig. 3.10a and c). Big bloom years occurred in 1998, 2002, 2003 and 2008, with noticeably dips in 2000 and 2004-2005. Highest runoff occurred in 1998, 2002-3, and 2006-7 (an estimate for 2008 was not yet available). In years when the peak chlorophyll is relatively higher than integrated chlorophyll (2002-2007), the duration is typically short (< 25 days). Generally, when a bloom begins earlier, it is also longer, except for the 2008 bloom which was late, long, and large. That the 2008 bloom persisted later into the summer may explain why it had higher peak magnitude and integrated chlorophyll, because more light is available later. Of all the variables, startday is the only one that appears to have a trend, with the earliest starts near the beginning of the record, and latest in 2008. During the 2008 spring bloom, both the north and central Labrador

Sea regions bloomed within a few days of each other. Of the physical measures, runoff and eddy-kinetic-energy track fairly well, at least during the increase from 2000-2003. The pattern in offshore velocity from resembles that of the subpolar gyre index (Hakkinen and Rhines, 2004; Hakkinen et al., 2008) though the latest years were not included in that paper. Both the gyre index and our offshore velocity dipped in 2004.

Correlations were calculated between the bloom and physical indices for the 11 year record (10 in the case of Greenland runoff, for which 2008 was not yet available). Some of the time series are strikingly correlated (Fig. 3.11). Eddy-kinetic-energy and Greenland runoff were both correlated with peak bloom in the north Labrador Sea with $r^2 = 0.38$ for EKE and $r^2 = 0.83$ for runoff, explaining 38% and 83% of the original variability. The table of r^2 values for all correlations is shown in Table 3.1. Assuming normal statistics and zero true correlation, 95% of sample correlation estimates based on 11 independent points will have r^2 values less than 0.36. For the central Labrador Sea, the only significant correlation was between light and the startday. For the north bloom, peak bloom correlated with offshore velocity, eddy activity, light and runoff; integrated chlorophyll with all but eddy activity. Start day was only correlated with offshore velocity. Estimating the peak bloom from physical parameters, we can write for the north bloom

$$peak\ intensity = 0.15 \times EKE - 4.74 ,$$

$$peak\ intensity = 0.36 \times Runoff - 7.65 .$$

While is possible to calculate multiple linear regressions, and in these cases results in explaining up to 85% of the variance in peak north bloom and 70% of integrated chlorophyll, it is not considered robust to use multiple independent (physical) variables for such a short (11 realization) record.

3.6 Conclusions

In this paper, we described the climatology and variability in two regions of the Labrador Sea spring bloom. The north bloom was early and intense owing to freshwater stratification, while the central Labrador Sea bloomed later, following deep convection. In the course of the study, we detailed biogeographical zones introduced in Devred et al. (2007); Wu et al. (2008); Frajka-Williams and

Rhines (2008) and quantified correlations between physical and bloom indices.

A test of Sverdrup's hypothesis using PAR from SeaWiFS satellite and climatological hydrography from the World Ocean Atlas 2005 demonstrated that stratification, light and ice control the bloom phasing in the Labrador Sea. In particular, buoyancy anomaly calculations showed that the haline contribution to stratification was responsible for the early northern bloom, explaining the reversal of the overall northward progression of bloom onset (Siegel et al., 2002). This haline stratification both prevents deep convection in the north Labrador Sea and also allows the early bloom. The haline-thermal balance of stratification highlights the relative importance of offshore velocities vs light or thermal warming.

EOFs identified regions of maximal variability: extending southward from the north bloom (49% of variability) and towards the Labrador slope for the central region (10% of variability). Using annual indices to represent bloom and physical processes, correlations suggest that light was responsible for variance in central Labrador Sea bloom timing, while it affected bloom intensity in the north. Bloom duration in the north seemed to relate to the intensity of offshore velocities from the 3000 m isobath, which was also correlated with both measures of bloom intensity: peak and integrated chlorophyll. The offshore velocity index is one indicator of the local strength of the subpolar gyre. The overall gyre strength is represented by the gyre index, which has shown that the subpolar gyre has been slowing and changing shape over 1992-2006 (Hakkinen et al., 2008). On the one hand, slowing would seem to imply a reduction in the offshore velocities used here (possibly seen through 2006 in Fig. 3.10b, though recent years appear to have sped up again. The change in shape, however, shortens the path of North Atlantic water to the Nordic and Labrador Seas. Significant shifts occurred in the 1990s and around 2002 and 2004.

Besides light, correlations suggest that higher eddy-kinetic-energy, offshore velocity and runoff from Greenland affect the bloom intensity. That eddies may enhance the bloom intensity due to their ability to vertically advect water properties and nutrients (Klein and Lapeyre, 2009). However, this is contrary to previous model results for eddy effects in the Labrador Sea which showed that eddies actually decrease nutrient availability (McGillicuddy et al., 2003).

Perhaps the most striking correlation was that between runoff from Greenland and bloom intensity, in part due suggestions of recent extreme changes in ice dynamics of Greenland (Luthcke et al., 2006; Stearns and Hamilton, 2007; Holland et al., 2008). While runoff from Greenland seems

several physical steps removed from the bloom location, it could steepen the boundary gradients, which could accelerate boundary currents and locally accelerate the subpolar gyre. Increased watermass gradients in the boundary currents could also enhance baroclinic instability, increasing the frequency of eddy-generation. However, one would expect that if either of these were true, then runoff and offshore velocity or runoff and eddy-kinetic-energy would be correlated, which they were not significantly. While linear regressions are suggestive of potential causation, they only show correlation. The model used to estimate Greenland runoff in Hanna et al. (2008) is forced by meteorological conditions which include factors related to light and heating. While validated with observations, it may be that changes in runoff from Greenland are due to an alternate process which affects both runoff and the bloom. Additional years of data will firm connections, or negate their (continued) influence.

The identified relationships between physical changes and bloom response have implications for physical influence on energy transfer to higher trophic levels. The significance of our work is further impacted sensitivity of the Labrador Sea to climate change. Another recent shift in physical processes is the magnitude of deep convection in the Labrador Sea. Overlapping our study period, deep convection was reduced from the late 1990s through 2007, but in the 2007-08 winter, the depth of convection passed 2000 m, owing to an increase in freshwater and ice in the northern Labrador Sea and Labrador shelf (Våge et al., 2009). Paradoxically, it may be that this freshwater protected the cold atmospheric winds until they reached the site of deep convection. The same increase in freshwater could be responsible for the change in shape of the 2008 bloom: large in size and magnitude. However, up to this point, we have intimated that an increase in freshwater would result in increased stratification and thus an earlier bloom. This is clearly not the case in 2008, when the latest bloom was observed. While it could be that the increased freshwater actually results in a thicker surface layer, a cursory look at Argo float data in our region showed that while springtime salinities were lower than over the base period (2002-2008), the mixed layer depths were not appreciably shallower.

This paper demonstrates the strength of remote observations to diagnose patterns and variability in the chlorophyll cycles. The processes and physical controls suggested by our analysis highlight the need for new *in situ* observations in this region, to describe the hydrography, nutrients and primary productivity, and directly identify dynamical links between the physics and biology, here

only suggested by simple correlations.

3.7 Figures

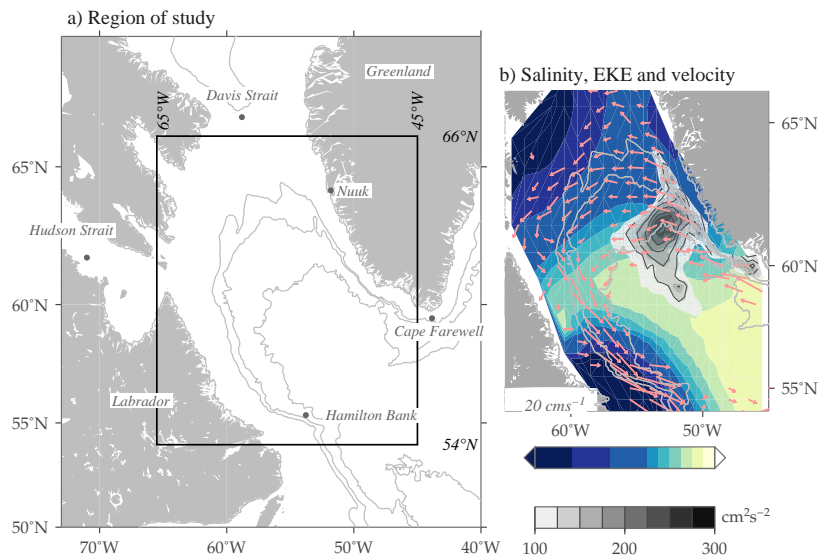


Figure 3.1: Bathymetry in the subpolar North Atlantic. Circulation in the Labrador Basin is typically cyclonic, following isobaths. The black box marks the domain for this study, from 54°N to 66°N and 65°W to 38°W.

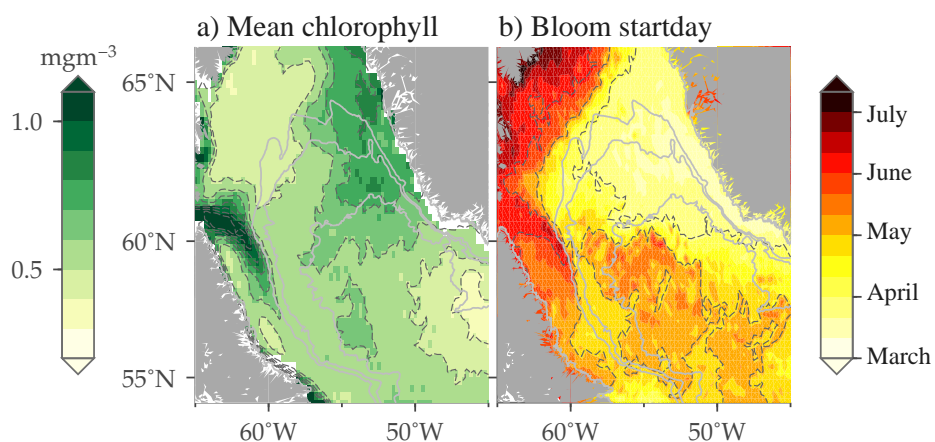


Figure 3.2: (a) Average chlorophyll from 1998-2007 and (b) median start day of the bloom. High mean chlorophyll regions (a) include the plume exiting the Hudson strait at 60°N and 65°W, and the dual-lobed feature off the coast of west Greenland, at 63°N and 57°W and 61°N and 55°W. In the start day (b) note that the Labrador Sea north of 60°N blooms early, the Labrador shelves and Hudson outflow bloom late, while the central Labrador Sea is intermediate in both magnitude and timing.

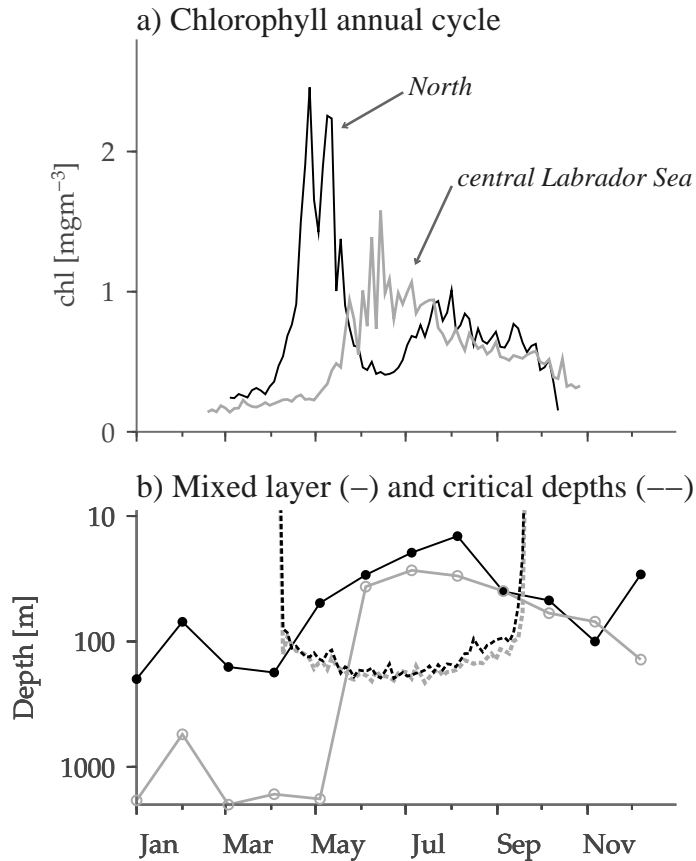


Figure 3.3: (a) Annual cycle in chlorophyll-*a* concentration from SeaWiFS at two locations averaged over 1998-2007. The north slope location (53.5°W and 62°N, dotted black) has the strongest and earliest bloom. The central Labrador Sea bloom is later and weaker (55°W and 58°N, solid gray) and the Hudson outflow region at 64°W and 60.5°N. (b) Annual cycle of mixed layer depth were calculated from Argo floats profiling within 1° of the target locations, and Sverdrup's critical depth calculated from SeaWiFS PAR using $PAR_c = 1.65$ and $k = 0.1275$. Once the mixed layer depth is shallower than the critical depth, a bloom is predicted to occur.

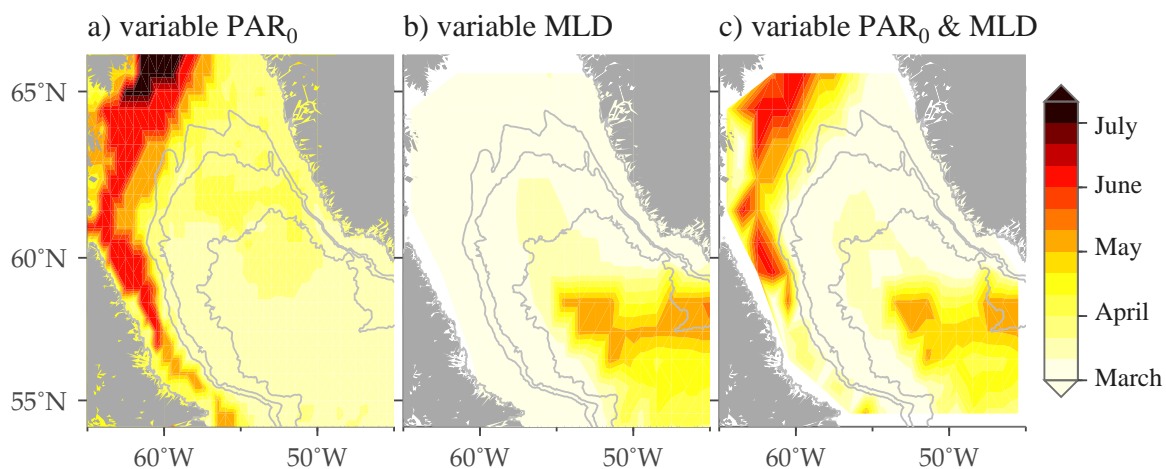


Figure 3.4: Predicted start days using Sverdrup's critical depth theory for three cases: (a) spatially variable light cycles (PAR_0), (b) spatially variable mixed layer depth cycles, and (c) variable light and mixed layer depth. From (a) we see the Labrador shelf timing is dominated by light while (b) shows that the north Labrador Sea is controlled by stratification.

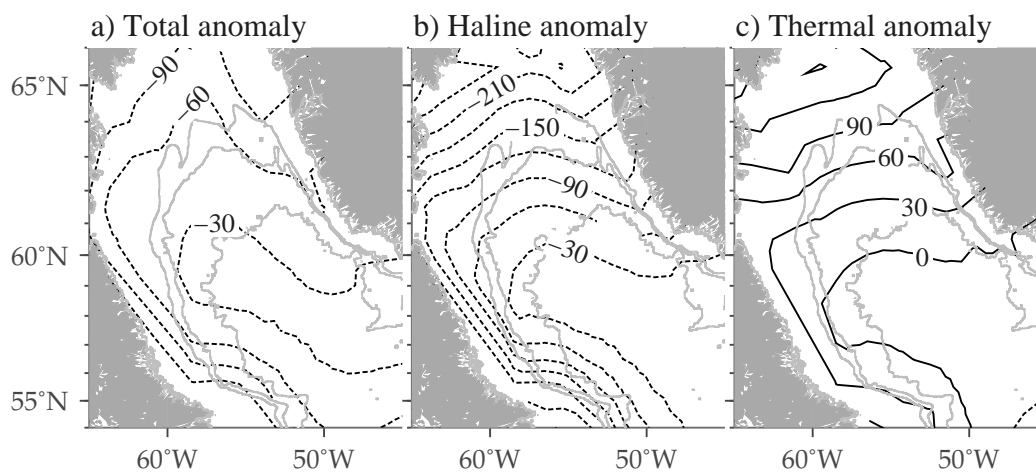


Figure 3.5: Buoyancy anomaly in May to 500 m from WOA 2005, shown as (a) total buoyancy anomaly, (b) anomaly due to temperature variations only, and (c) anomaly due to salinity variations only. Positive values are destabilizing (salty or cold) while negative values are stabilizing (fresh or warm).

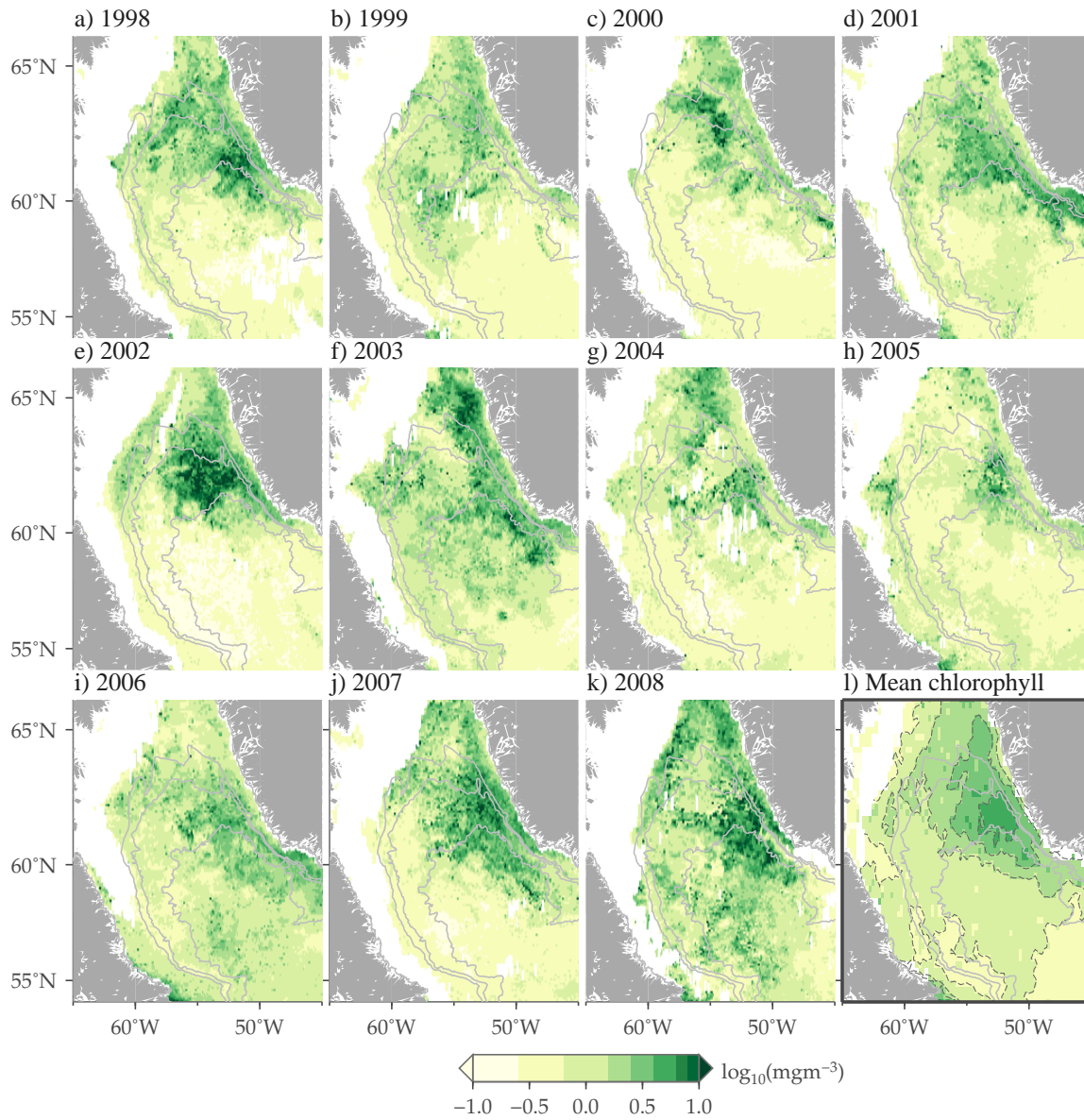


Figure 3.6: (a-k) Chlorophyll for each year, 1998-2008, averaged over April and May at 9 km resolution. (l) Mean chlorophyll in April and May for the whole record, 1998-2008.

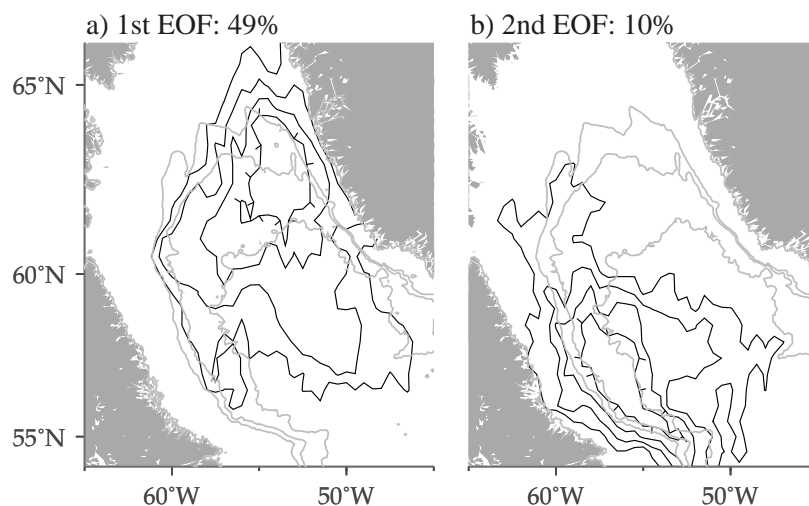


Figure 3.7: EOFs for 1998-2006 chl-*a* show major patterns of variability. (a) The first EOF explains 49% of the variability and is a background seasonal cycle. (b) EOF 2 shows a strong signal on the north slope of the Labrador Sea off the west Greenland shelf.

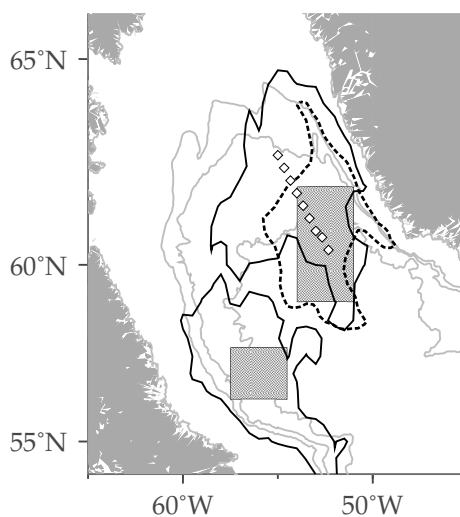


Figure 3.8: Map showing regions used to calculate annual indices. The two regions are in the shaded rectangles, the more northerly one corresponds to the north bloom while the south-westerly corresponds to the central Labrador Sea. The dotted outline is the region of high ($> 50 \text{ cm}^2\text{s}^{-2}$) mean eddy-kinetic-energy. The two solid outlines correspond to a threshold of 0.23 in the homogeneous correlation maps. The black and white diamonds are the locations where offshore geostrophic velocity anomalies were calculated, positive being perpendicular to this line, to the southwest.

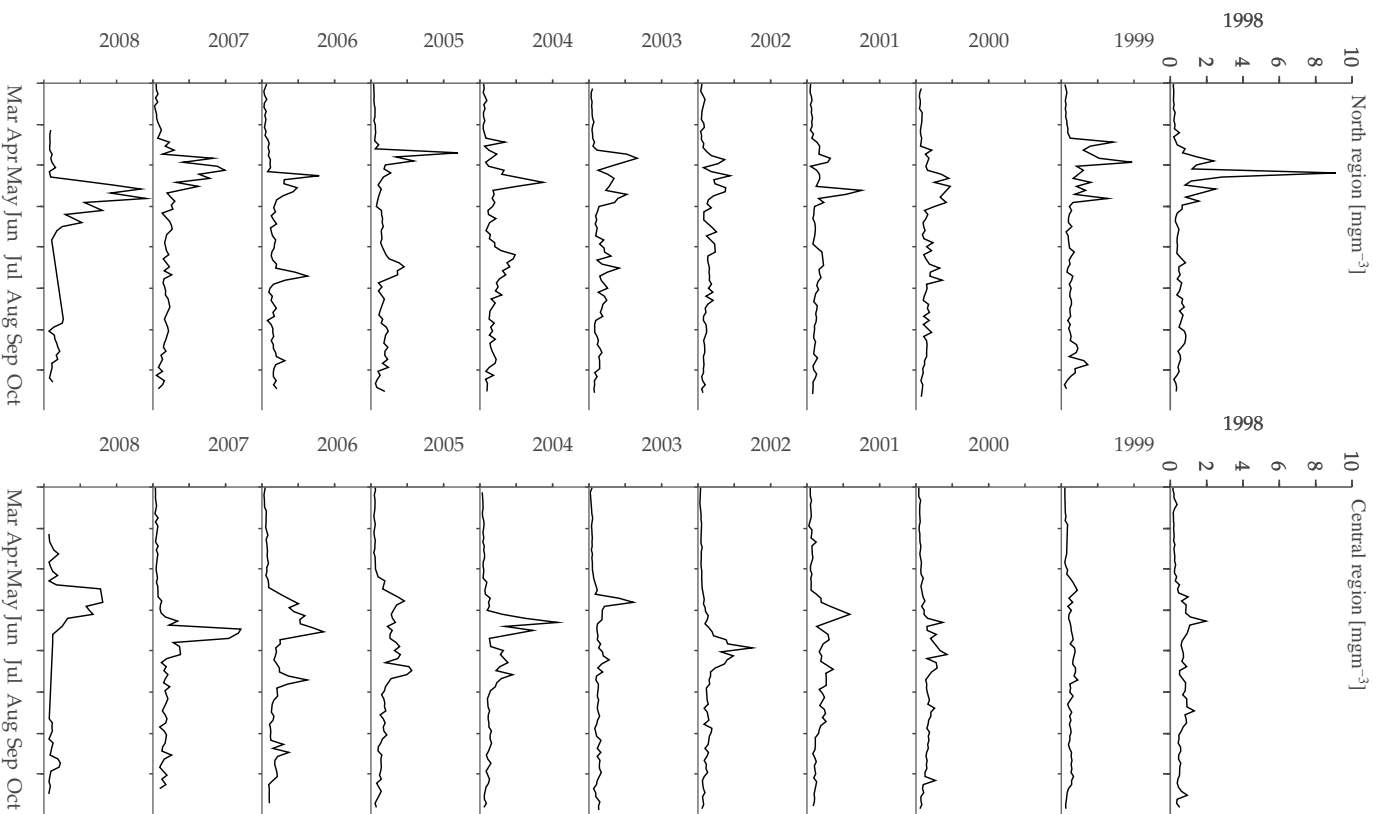


Figure 3.9: Timeseries of chl for the north bloom region (a) and central Labrador Sea region (b).

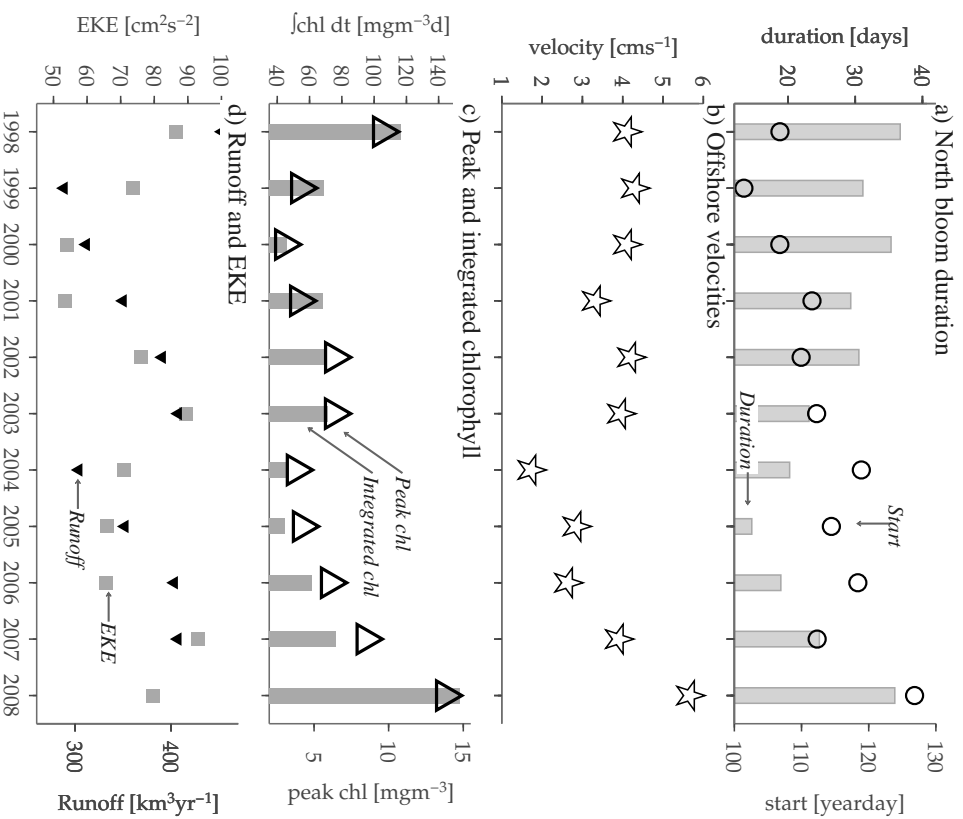


Figure 3.10: Measures of bloom and physical variability in the north region, defined by the gray box in Fig. 3.8. (a) North bloom start day (in yearday) and duration. (b) Offshore velocities averaged from March-May between 60-63°N, positive values to the southeast. (c) Peak and integrated chlorophyll. (d) Annual average runoff from Greenland and eddy-kinetic-energy.

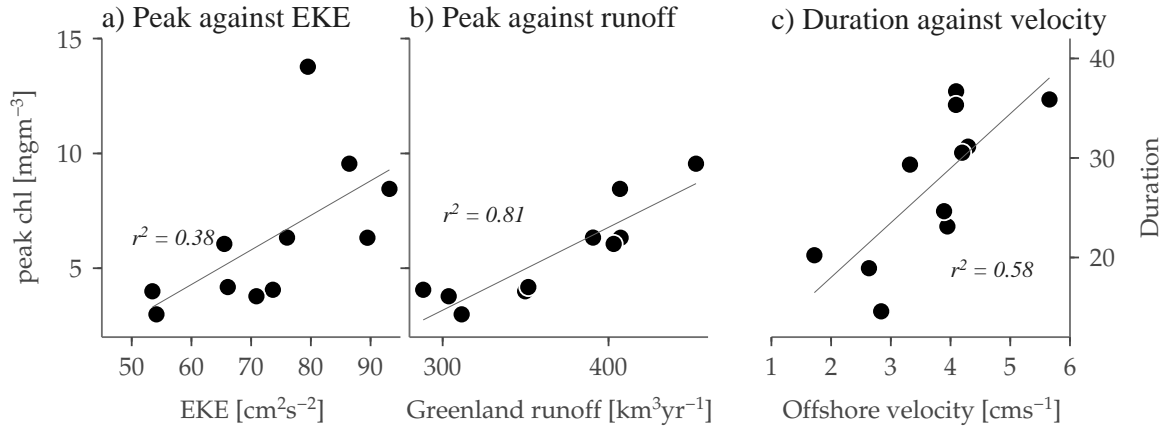


Figure 3.11: Linear regressions between peak bloom magnitude and two physical measures (a) eddy-kinetic-energy and (b) runoff from Greenland and (c) between bloom duration and offshore velocity.

(a)	peak	$\int dt$	startday
Irradiance (PAR)	0.0	0.0	0.5

(b)	peak	$\int dt$	duration
Greenland runoff	0.8	0.5	0.0
Irradiance (PAR)	0.7	0.7	0.1
Offshore-velocity (spring)	0.4	0.5	0.6
Eddy-kinetic-energy	0.4	0.2	0.0

Table 3.1: (a) Central Labrador Sea bloom variability is only explainable in terms of irradiance, highlighting the importance of thermal warming to the startday in the bloom. (b) North slope bloom variability as explained by physical processes: annual runoff from Greenland (Hanna et al., 2008), offshore geostrophic velocities between 60-63°N, annual irradiance from SeaWiFS PAR, and annual eddy-kinetic-energy. All physical indices were available for 1998-2008 except for Greenland runoff which was only available from 1998-2007. Significant correlations at 95% are boldface.

Chapter 4

DETERMINING VERTICAL WATER VELOCITIES FROM SEAGLIDER**4.1 Introduction**

In most places in the world's oceans, vertical velocities are small (order 1 cm s^{-1}). Vertical stratification, typically much higher than horizontal, creates a barrier to vertical motion, requiring a conversion between kinetic and potential energies. Vertically mixed regions, i.e. the wind- or convectively-driven mixed layers, can have higher vertical velocities (order 10 cm s^{-1}) as can sloping boundaries along topography where horizontal energy is converted to vertical energy by the interaction with the bottom.

In the stratified ocean, the velocity spectrum is dominated by internal waves, described by the Garrett-Munk spectrum (Garrett and Munk, 1972, 1975, 1979; Gregg and Kunze, 1991). Vertical velocity variance due to internal waves can be described by integrating the Garrett-Munk model to give

$$\langle w^2 \rangle = 0.25 \frac{N_0}{N} \quad (4.1)$$

where $N_0 = 5.3 \times 10^{-3} \text{ rad s}^{-1}$ is the canonical stratification. The energy level given by the $c_{GM} = 0.25 \text{ cm}^2 \text{ s}^{-2}$ coefficient is for the abyssal ocean and may vary depending on forcing. Variance in mixed regions may scale with wind energy or buoyancy fluxes. Results from prior observations of vertical velocities in the Labrador Sea during deep convection show that rms-vertical velocities scale with buoyancy forcing and with wind forcing, with a 0.5 day lag between the forcing and the resulting vertical velocity (Steffen and D'Asaro, 2002).

In this paper, we describe a technique for estimating vertical velocities from Seaglider, an autonomous underwater vehicle. Seaglider estimates vertical velocities from the difference between a predicted glider flight speed in still water and the observed glider vertical velocity from pressure,

$$w_w = w_{meas} - w_{stdy} , \quad (4.2)$$

where w_w is inferred water vertical velocity, $w_{meas} = dz_g/dt$ is measured glider vertical velocity and w_{stdy} is the modeled glider velocity. Glider vertical position z_g , measured positive upward, is computed from observed pressure and t is time. Two Seagliders (called sg014 and sg015) were deployed in the Labrador Sea in the fall of 2004. They observed stratified ocean as well as convectively mixed regions to 1000 m depth. Using the theoretical understanding of vertical water velocity and knowledge of glider flight, we tune the glider flight model then estimate errors on the vertical velocity estimates.

In §4.2, we introduce the Seaglider flight model and overall estimation procedure for vertical water velocity. In §4.3 we introduce the flight parameters. In §4.4 we show the sensitivity of the w calculation to choices of flight parameters, and in §4.5 we describe the optimization procedure. In §4.6 we give the results of the optimization procedure, including showing consistency checks with theoretical expectations for vertical velocity and error estimates.

4.2 Glider flight model

Seaglider has a low drag hydrodynamic shape, and controls its flight by changing its buoyancy and pitch angle. Pitch is changed by moving the battery pack inside the glider fore and aft. Pitch is measured by a tilt meter (Precision Navigation TCM2-80 compass). Buoyancy changes are controlled by a variable buoyancy device (VBD) which has a range of 822 cc for sg015 and 827 cc for sg014. Glider buoyancy relative to *in situ* seawater buoyancy also depends on glider compressibility, volumetric thermal expansion and initial volume. Glider density is estimated as

$$\rho_g = M/V(t, p, T), \quad (4.3)$$

where M is glider mass and V volume. Volume changes in time t , with pressure p and temperature T due to pumping, compressibility, and thermal effects,

$$V(t, p, T) = (V_0 + v_c(t)) e^{-\gamma_g p + \alpha_g (T - T_0)}, \quad (4.4)$$

where $v_c(t)$ is the change in volume due to the pump, V_0 is the glider volume at $p = 0$ and $T = T_0$ with the pump in $v_c(t) = 0$ position, γ_g and α_g are the compressibility and volumetric thermal expansion coefficients, p is pressure, T is temperature and T_0 is the reference temperature.

The Seaglider flight model model assumes steady flight, i.e. no acceleration or that forces (lift L , drag D and buoyancy B) balance:

$$L = ql^2 a \alpha = -B \cos \theta \quad (4.5)$$

$$D = ql^2 \left(bq^{-1/4} + c\alpha^2 \right) = B \sin \theta \quad (4.6)$$

where $q = \rho/2(U^2 + W^2)$ is the dynamic pressure, ρ is water density, U and W are horizontal and vertical speeds and l is the hull length (1.8 m, not including antenna). More details of the model are given in (Hubbard, 1980) and Eriksen et al. (2001). Lift is proportional to the attack angle α . Hull or profile drag is proportional to $(speed)^{3/2}$, giving the parameterization $bq^{-1/4}$ while $c\alpha^2$ is the drag induced by lift. Attack and glide angles are related via the pitch angle, $\alpha + \theta = \phi$ where α is attack, θ is glide and ϕ is pitch. Glider flight depends on the attack angle (a function of pitch and glide angle), glider relative buoyancy and lift and drag of the instrument.

A chart showing the flow of data processing is in Fig. 4.1. Measured quantities are in blue, undetermined coefficients and constants in yellow. The loop at the right hand side indicates that there is a feedback between calculations of salinity and vertical velocity, however analysis has shown that even in the Labrador Sea, where salinity variations dominate density calculations, small changes in salinity have little effect on vertical velocity.

4.2.1 Steady assumption

Due to computational limitations, we approximate the unsteady flight model with a steady one: assuming that lift, drag and buoyancy forces are always in balance ($U \rightarrow u_{stdy}$ and $W \rightarrow w_{stdy}$). The steady flight model does poorly near the surface and deep turnaround points, where the glider vertical velocity passes through zero. Also near the apogees, the buoyancy and pitch is changing rapidly, due to the VBD pumping and internal movement of weights in the glider. Hence, we neglect measurements in the top 50 m or bottom 50 m from the deep apogee before determining flight parameters. Leaving out the top 50 m of points also reduces some contamination by potential air bubble effects near the surface. Air bubbles can become trapped in small spaces of the Seaglider, or between the pressure hull and fairing, changing the glider's compressibility until pressure effects dissolve the air. This compressibility effect was shown by tests of glider compressibility in a pressure tank, Fig. 4 of Eriksen et al. (2001).

4.2.2 Roll maneuvers

The Seaglider monitors its heading continuously during a dive cycle. When the heading drifts by a user-defined amount from the desired heading, Seaglider will execute a roll maneuver to correct the heading. Typically roll maneuvers last a few tens of seconds, though in some cases an extended maneuver is required to correct the heading. Extended roll maneuvers may result in vertical velocity spikes. Fig. 4.2 shows sg014 cycle 540 measured glider velocity (w_g). On the left is measured velocity during the dive with periods of rolling highlighted in gray. There is no correspondence between w_g and rolls. On the right is w_g from the climb, when a series of extended roll maneuvers were executed. Peaks in w_g during and after the roll maneuvers are apparent. Because of the unsteady nature of the recovery, simply ignoring the individual points involved in a roll maneuver does not eliminate the spiking. Since removing individual points did not remove the entire spike, we discarded the entire contaminated w profile prior to tuning the flight model.

4.3 Flight parameters

Nominal starting values for flight coefficients, glider volume and compressibility are estimated in tank tests. Initial parameter values for sg014 are

$$a = 0.003836 , \quad (4.7)$$

$$b = 0.010078 , \quad (4.8)$$

$$\gamma_g = 4.4 \times 10^{-6} , \quad (4.9)$$

$$V_0 = 51400 \text{ cc} \quad (4.10)$$

$$\alpha_g = 70.5 \times 10^{-6} . \quad (4.11)$$

Using these values, we calculated the average profiles of vertical water velocity, separated by those measured during glider dives and glider climbs. The results are in Fig. 4.3, dashed lines. The estimated average vertical water velocity is between 0.5 and 1 cm s^{-1} upwards, with a 0.5 cm s^{-1} difference between dives and climbs, and a vertical divergence of 0.4 cm s^{-1} over 1000 m. We do not expect a mean upwelling to this degree, nor that the vertical water velocity depends on whether the glider was diving or climbing. The initial values of flight parameters need to be adjusted for each glider.

4.3.1 Note on volumetric thermal expansion in glider buoyancy calculation

Changes to glider volumetric thermal expansion α_g affect glider volume mostly through $\delta\alpha_g T_0$, where $\alpha_g T_0$ is a reference adjustment to volume. Since the choice of T_0 is arbitrary, the effective change of volume that may be compensated for by adjusting V_0 ,

$$V_2 = (V_0 + \delta V + v_c(t))e^{-\gamma_g p + \alpha_g (T - T_0 - \delta T_0)} \quad (4.12)$$

then requiring $\overline{V - V_2} = 0$. This further requires

$$-\alpha_g \delta T_0 = \overline{\log \left(\frac{V}{V + \delta V} \right)}. \quad (4.13)$$

In testing the sensitivity of vertical velocity estimates to changes in α_g (§4.4), we eliminate this effect by adjusting V_0 each time α_g is updated so that the net change in volume is zero. The sensitivity to changes in α_g shown in Fig. 4.4 reflect this two step update. This is equivalent to changing the reference temperature T_0 each time α_g is updated so that the effect of α_g due to variations in T only are expressed. The result is that changes in w due to $\alpha_g T$ is small.

4.4 Sensitivity of w to parameters

Tuning the glider flight model involves fixing the unknown flight parameters and constants in some intelligent fashion before estimating vertical velocities. We first consider how each parameter affects the estimate of vertical water velocity (w_w). Flight parameters and constants are marked in yellow on the flow chart in Fig. 4.1 and include lift coefficient (a), drag coefficient (b), induced drag coefficient (c), volume (V_0), glider absolute compressibility (γ_g) and glider volumetric thermal expansion (α_g). Seaglider has a hull which is nearly neutrally compressible, with observed changes in weight of less than 0.5 g over a 500 dbar change (Eriksen et al., 2001). Vertical temperature gradients in the Labrador Sea are low ($< 10^\circ\text{C}$ from surface to 1000 m). Small changes to the volumetric thermal expansion coefficient have little effect on glider flight.

The effect of a change in a flight parameter value was calculated by increasing each parameter from a nominal value by 5% or 5 cc for volume. Original estimates of vertical water velocity (w_w) were differenced from the new estimates. The difference profiles for sg015 cycle 230 are shown in Fig. 4.4. The strongest changes resulted from changes in volume, lift and drag coefficients, and

glider compressibility. Thermal expansion and induced drag have a negligible effect on vertical velocity (for thermal expansion, the reason is described below).

Changes to volume and compressibility had the same sign effect on w_w , regardless of whether the glider was diving or climbing. Increases to volume resulted in a shift towards downwelling w_w , while increases to compressibility (effectively a reduction in glider volume at depth) shifted w_w towards upwelling. Unpacking the effect, we consider the case of a change in the expected volume of the Seaglider. The initial guess for volume is estimated as the sum of its parts, but is not fully determined until the glider is in the field. An increase in expected volume of the glider relative to some initial guess means the glider is always more buoyant than when using the initial guess. A more buoyant glider shifts the predicted glider vertical velocity in the upwards direction. For the same measured glider vertical velocity (from dz_g/dt) on a dive, say diving downwards at 10 cm s^{-1} , the predicted vertical water velocity will be greater in the downwards direction. Conversely, suppose for a glider climbing at an observed rate of 10 cm s^{-1} upwards, that the initial volume guess resulted in a predicted glider vertical velocity of 5 cm s^{-1} . This suggests the glider was caught in a upward plume of 5 cm s^{-1} . If we now realize that the glider was more buoyant than initially believed, then the predicted vertical velocity is now increased, to 7 cm s^{-1} , then the estimated vertical water velocity is upward at only 3 cm s^{-1} . In the case of both a dive or a climb, an increase in estimated glider volume results in a downward shift of the estimated vertical water velocities.

This can also be seen by inspecting the balance of lift, drag and buoyancy. While the magnitude of the predicted velocities are shown here, separating the force balance for a glider dive vs climb is instructive. See Fig. 4.5. In the following examples, w is positive up. An increase in glider volume V_0 means that the glider is less dense and the buoyancy force B in the equations will be more positive for both a dive and climb. Then the resulting w_{stdy} for both a dive and a climb will be increased, so that w_w is decreased.

Changes to lift and drag coefficients, on the other hand, had differing effects depending on whether the glider was diving or climbing. For the same buoyancy force B and glide angle, if the lift coefficient a increases, then for a dive, then $U^2 + W^2$ must decrease, which results in an decrease in w_w . For a climb, if the lift coefficient a increases, then the computed w_{stdy} is decreased and w_w is increased. From this heuristic explanation, and the profiles in Fig. 4.4, the mean offset of vertical velocities measured on dives and climbs can be adjusted by changing the volume V_0

while the difference between vertical velocities inferred from dives and climbs (in Fig. 4.3) can be adjusted by changing lift and drag coefficients.

4.5 Optimization

4.5.1 Assumptions

Two primary assumptions are used in estimating the flight parameters. The first is that mean vertical velocity is zero. For internal waves which are periodic in space and time, this assumption is obvious, though an individual profile of vertical velocity may have a nonzero mean depending on what phases of the wave were captured. In the mixed layer, the assumption is still just mass conservation: that water going up in the mixed layer is balanced by water coming down. If the glider samples adequately randomly and enough, it should hold.

The second assumption is that the vertical water velocity does not depend on whether the glider is diving or climbing. This means that there should not be an offset between profiles of vertical water velocity averaged from glider dives only vs from climbs only. This constraint reminds us that only the lift and drag parameters described in §4.3 are able to bring the mean dive and mean climb profiles of vertical water velocity closer together.

4.5.2 Choice of minimization

Based on these two assumptions and knowledge about how each flight parameter and constants affected the profiles of vertical velocity, we tested a number of cost functions to minimize:

- Vertical water velocity variance, $\sum_t w_w(t)^2$
- Temporal mean profiles from dive and climb, $\langle |w_d(z)| + |w_c(z)| \rangle_z$
- Temporal mean offsets between profiles from dive and climb, $\langle |w_d(z) - w_c(z)| \rangle_z$
- Offsets in dive-climb magnitude, $|\langle |w_d(z)| - |w_c(z)| \rangle_z|$
- Vertical divergence, $\langle |w_d(z) - \langle w_d(z) \rangle_z| + |w_c(z) - \langle w_c(z) \rangle_z| \rangle_z$

where $\langle \cdot \rangle_z$ is the depth-average of a mean profile, $w_w(t)$ is the estimated water velocity at time t , $w_d(z_0) = \langle w_w(t : z(t) = z_0 |_{dive}) \rangle$ is a mean profile of vertical water velocity estimated during glider dives only, $|\cdot|$ is the magnitude. Each average is calculated over an ensemble of dive cycles which may vary from 20 cycles to the entire mission.

Examples of these minimizations run on pairs of parameters are shown in Fig. 4.6. Each panel shows the resulting mean profiles of w from dives and climbs after the minimizations were run. Red lines show a linear fit through each mean profile. The first two minimizations, $\sum_t w_w(t)^2$ and $\langle |w_d| + |w_c| \rangle_z$ in panels (a) and (b), top row have very similar final profiles and sets of parameters (marked in the figure). In the second row, panels (c) and (d) show the results of minimizing offsets between the dive and climb profiles, $\langle |w_d - w_c| \rangle_z$ and $|\langle |w_d| - |w_c| \rangle_z|$. There is vertical divergence in the final profiles, resulting from only minimizing the difference between the mean dive and mean climb at each depth. These minimizations only constrain the effects of a subset of the 4 main flight parameters, leaving others to vary. The result is an unlikely profile of vertical velocity. The last minimization, third row, panel (e), which minimizes vertical divergence ($\langle |w_d - \langle w_d \rangle_z| + |w_c - \langle w_c \rangle_z| \rangle_z$) fails to minimize the mean vertical velocity and results in a huge offset between w_d and w_c . We conclude that either $\sum_t w_w(t)^2$ or $\langle |w_d| + |w_c| \rangle_z$ are the best choices and call the latter w_{resid} in figures.

This minimization does not take into account possible other sources of error, besides uncertainties in flight parameters. These include asymmetries in the glider geometry or changes in flight parameters due to the ocean state. The flight model was developed for the original glider shape and sensor configuration, including the two gliders used in this paper. Sensor configuration has changed somewhat with later generations, however we expect the change to be small. It is possible that the glider flight model varies depending on the ocean state. That is, in areas of laminar flow, the drag characteristics of the glider may be different than in areas of turbulent flow.

4.5.3 Note on data processing for a semi-Lagrangian instrument

Within the mixed layer, the glider signature of vertical velocities may be affected by horizontal convergences and divergences. For example, during deep convection, surface velocities converge towards downwelling plumes. As a result, any instrument that spends time “resting” at the surface–

whether by the user's choice or to communicate data via satellite—would tend towards regions of downwelling, resulting in a vertical velocity profile that is biased towards downwelling at the surface. The magnitude of this bias depends on the scales of convergence and the time at the surface (Legg and McWilliams, 2002; Lavender et al., 2002).

Due to its relatively low speed, approximately 20 cm s^{-1} , the glider is advected by strong currents and turbulent motions. In regions with strong vertical velocity, the glider may be sped along its dive or climb. While in the dive phase of a dive-climb cycle, the glider monitors its descent rate and assumes it has reached the sea floor if a null rate persists sufficiently long. In recent missions to the Faroe Islands, a glider was caught in such a strong updraft that the dive was arrested, the glider aborted the dive and returned to the surface. Strong currents affect the sampling behavior of Seaglider, and so care must be taken when processing data.

Profiles that are gridded, binned or interpolated onto an evenly spaced depth-grid must be appropriately weighted by inverse glider speed in order to calculate statistics on multiple dive cycles. The effect of unweighted gridding of glider estimates of vertical velocity are shown in Fig. 4.7. Vertical velocity estimates were divided by whether the glider was diving or climbing (green or blue curves) and whether the glider was in the mixed layer or stratified region below (top vs bottom row). On the left are histograms for all sg014 w estimates, with no gridding applied. On the right are histograms for sg014 w which was gridded onto a 4 m evenly spaced depth grid. In the mixed layer, gridding accentuates downward motions during dives and upward motions during climbs. A purely Lagrangian instrument is speeded through downwelling on a dive, appropriately weighting the downwelling by measuring evenly in time. All average profiles shown here were computed within depth bins for measurements on the original time-spaced grid.

4.5.4 Procedure

Our minimization procedure is to regress for a and b jointly over the first 50 cycles, then γ_g and δV on all dive cycles (1-663 for sg014, 1-617 for sg015). This is iterated until parameter values converge. The resulting offset between dive profiles and climb profiles is $\sim 0.1 \text{ cm s}^{-1}$. Since only a and b fix this offset, we regressed for b on dive cycles 1-663 then γ_g and δV on dive cycles 1-663 until these again converged. The final value of b was 0.0088 instead of 0.0092, a change of less than

5%. This new value reduces the offset between w_d and w_c to less than 0.05 cm s^{-1} .

4.6 Results

The parameter sets that resulted in a minimizing $\langle |w_d| + |w_c| \rangle_z$ for sg014 over the entire mission was

$$a = 0.004 , \quad (4.14)$$

$$b = 0.0088 , \quad (4.15)$$

$$\gamma_g = 4.11 \times 10^{-6} , \quad (4.16)$$

$$\delta V_0 = -12.4 , \quad (4.17)$$

where the new $V_0 = V_{0,initial} - \delta V_0$. The resulting offset between w from dives and climbs, averaged over ensembles of 20 dive cycles is shown in Fig. 4.8. Bathymetry is stippled, and maximum and minimum mixed layer depths in each ensemble are plotted in white. Offsets between average velocities from dives and climbs appear to be distributed around zero with no clear structure. Magnitudes of the offset are higher in the deep mixing regions, but velocities there are also higher.

4.6.1 Consistency check

Our consistency checks are based on the assumptions used in creating the minimization as well as the theoretical understanding of the character of vertical velocity in the ocean. We have already shown that the mean dive and climb profiles of vertical velocity do not differ significantly, but this is a condition that was enforced by our minimization. In the stratified ocean, we expect that rms vertical velocities scale with $1/\sqrt{N}$ as

$$\langle w^2 \rangle = 0.25N_0/N . \quad (4.18)$$

The bulk estimate for the entire mission is shown in Fig. 4.9 and matches well for lower N . Above $N \approx 1.5 \times 10^{-3} \text{ rad s}^{-1}$, the scaling breaks. N higher than 1.5×10^{-3} is in the thermocline. The thermocline is both an area where the scaling can be expected to break down since energy may be trapped by stratification. This is discussed further in Chapter 5. The thermocline is also a

region where we expect the highest errors in salinity estimation, in particular, salinity spiking due to uncertain CT flushing rates in regions with large temperature gradients.

In the unstratified mixed layer, primary energy sources are winds and buoyancy flux from the atmosphere. Comparing rms vertical velocity averaged within the mixed layer over 1-day periods with forcings, we find that velocities lag forcing at 0.6 and 0.7 days, and have an $r = 0.65$ and $r = 0.58$ correlation coefficients, Fig. 4.10. Both these results give us confidence that the vertical velocity estimates by Seaglider are realistic.

4.6.2 Error estimates

Errors in vertical velocity can be estimated several ways: (1) as the uncertainty in w_w due to uncertainty in parameters (a , b , γ_g , δV), (2) the offset between the mean dive and mean climb profiles $\langle w_d - w_c \rangle_z$, and (3) by the high frequency noise level.

Frequency spectra of vertical velocity were calculated from glider profiles in the mixed layer and below the mixed layer. Data were first subsampled to the lowest sampling rate, 40 s for sg014, and only profiles with at least 256 data points were used. There were 19 such profiles in the mixed layer and 39 in stratified water. Spectra were averaged together producing the estimate in Fig. 4.11a. Higher energy is visible in the mixed layer than below by about a decade or multiple of 3 for velocity. Also shown (Fig. 4.11b) is a histogram of buoyancy frequency values for the two sets of profiles. As expected, N is larger for the profiles taken below the mixed layer. For frequencies less than N , the GM-model predicts a white spectrum of w while above N would be a Kolmogorov spectrum with slope $-5/3$. Since N varies, there would just be a tendency towards these slopes. At the highest frequencies, above $N > 0.0126 \text{ rad s}^{-1}$, instrument noise increases, as can be seen by the high frequency rolloff in the spectrum from profiles of w below the mixed layer. The noise estimate from this method is $\pm 0.6 \text{ cm s}^{-1}$.

4.7 Discussion

We have shown how the various unknown flight parameters in the Seaglider flight model affect estimated profiles of vertical velocity. Lift and drag can move mean profiles estimated from dives and climbs closer together, while induced drag has little to no effect. Volumetric thermal expansion

had a small effect, once the volume offset due to the reference temperature was accounted for.

Five minimization choices were tested, and it was determined that there is little measurable difference between $\langle w^2 \rangle$ and $\langle |w_d| + |w_c| \rangle_z$. The latter minimization was chosen since it seems more likely to constrain the actions of the various flight parameters. We described the compensation between parameter choices, and as a result, chose to run the minimization over the entire mission, after fixing the lift coefficient from the first 50 dives. The resulting offset between mean dive and climb profiles was very small, and the pattern of offsets over the course of the mission and in depth was reassuringly random.

We checked the resulting estimates of vertical velocity with the theoretical WKB scaling from Munk (1981) and found that they compared well in the weakly stratified deep ocean, though the scaling broke in the thermocline. Further consistency checks are given in Chapter 5, confirming that vertical velocity magnitudes and scales compare well with theoretical expectations for the mixed layer and stratified ocean, and relationships with forcing. The high-frequency roll off in the vertical velocity spectrum gives an estimate of the noise, approximately $\pm 0.6 \text{ cm s}^{-1}$.

Appendix: Effect of a faulty pitch sensor on w (sg015)

Glider sg015 was found to have a faulty pitch sensor. For Seaglider, this can be diagnosed by estimating the relationship between measured pitch and pitch control. The glider estimates a desired pitch angle based on its distance from the target latitude and longitude, and the flight model. To meet that angle, it adjusts pitch control which refers to the distance forward and aft that the battery pack moves within the glider body to set the pitch. The gain is approximately 12-15° per centimeter movement. Since pitch also depends on buoyancy and the marginal volume (VBD), we calculate the linear relationship between observed pitch and the predicted control elements for sg014 to check the stability of the relationship,

$$\theta = \mathbf{A} \begin{bmatrix} I \\ \theta_{control} \\ v_c \\ B \end{bmatrix}, \quad (4.19)$$

where \mathbf{A} are the coefficients (\mathbf{A}_1 being a mean contribution), I is an identify vector, $\theta_{control}$ is the pitch control, v_c is the volume change produced by the VBD and B is the glider's buoyancy. The resulting coefficients \mathbf{A} are shown in Fig. 4.12, filled gray circles. The estimates, done over ensembles of 20 dive cycles were fairly constant, especially in the mean, though some dependence on pitch control was seen. The the latter half of the mission, when the glider was experiencing deep convection (cycles 350-350, the buoyancy and VBD dependence appear more variable, but because buoyancy changes very little and the VBD did not have to pump as much, the net contribution of the buoyancy and VBD dependencies on pitch remains small. Repeating the same procedure for sg015, we see that the mean relationship (Fig. 4.12a) is much more variable, especially after dive cycle 300 (Fig. 4.12, open black circles). The result, if we do not attempt some correction for pitch, is that the mean vertical water velocity is near zero for the first 250 dive cycles but significantly nonzero in the latter half of the record.

To test the effect of replacing the pitch input to the glider flight model with an estimated pitch, we calculated the relationship between pitch and controls for sg014 from the first 331 dive cycles, then estimated pitch for these same dive cycles based on the model. We repeated this for sg014, cycles 332-663 and sg015 cycles 1-308 where the pitch model was relatively constant.

The difference between the new average profiles, using the estimated pitch, and the original average profiles using the measured pitch is shown in Fig. 4.13. The offset is large right at the surface, where pitch changes rapidly, but there also appears to be a mean offset between vertical velocity from the dive and climb with corrected pitch. The offset is on the order of 0.1 cm s^{-1} , with climbs having a greater mean upward vertical velocity. If sg015's pitch may be corrected in this way for the latter half of the record, then we can expect a mean offset between the dive and climb in the corrected pitch, and that vertical velocity error is increased by about 0.1 cm s^{-1} .

4.8 Figures

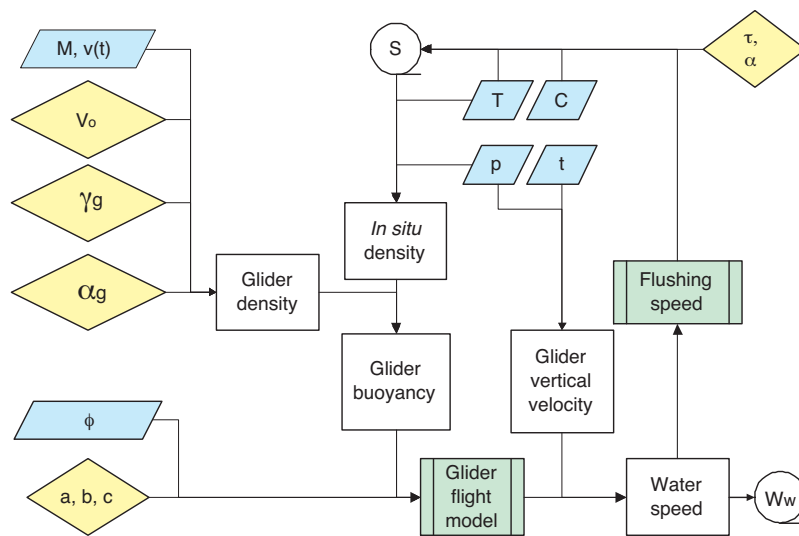


Figure 4.1: Flow chart of Seaglider flight model and processing procedures. In blue are measured quantities (glider mass M , controlled volume $v(t)$, temperature T , conductivity C , pressure p , time t and pitch θ), in yellow are parameters of the flight model (volume V_0 , glider absolute compressibility γ_g , thermal expansivity α_g and lift a , drag b , and induced drag c coefficients) and the salinity calibration parameters (τ and α). In green are the models applied, the Seaglider steady-flight model and the CT-cell flushing speed. In white are calculated quantities. Vertical water velocity (w) and salinity (S) are the calculated products affected by tuning the flight model.

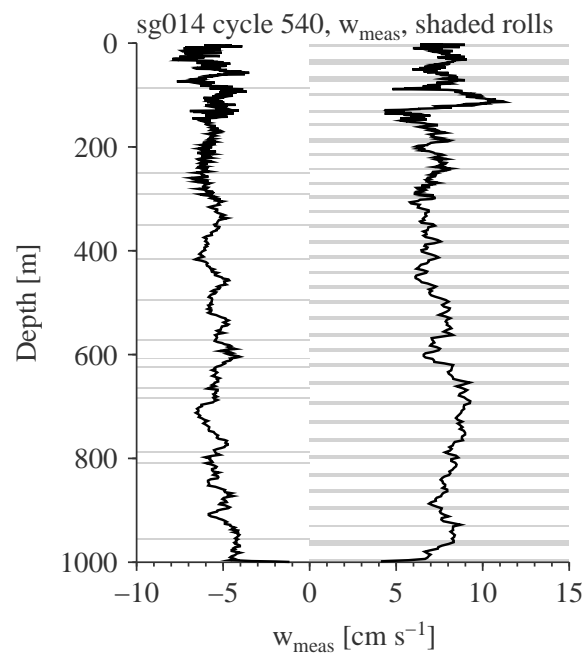


Figure 4.2: Measured vertical glider velocity in the presence of extended roll maneuvers, sg014 cycle 540. Glider vertical velocity w_{meas} is plotted, so negative values correspond to diving and positive values to climbing. The duration of a Seaglider roll maneuver is shaded in gray. Note the velocity spikes during roll maneuvers as the Seaglider was climbing (right side of plot).

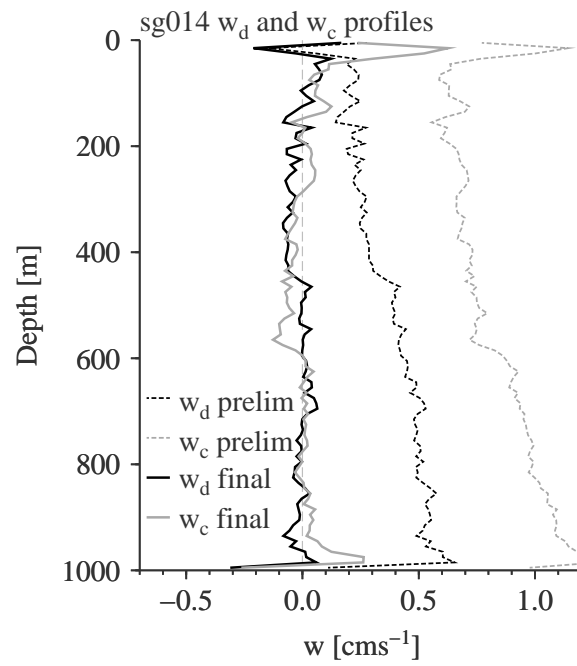


Figure 4.3: Average profiles of vertical water velocity, separated by glider dives (black) and climbs (gray), for the entire mission sg014. In dashed are the average profiles using nominal flight parameters. In solid are the average profiles using flight parameters chosen by the procedure outlined in §4.5.4.

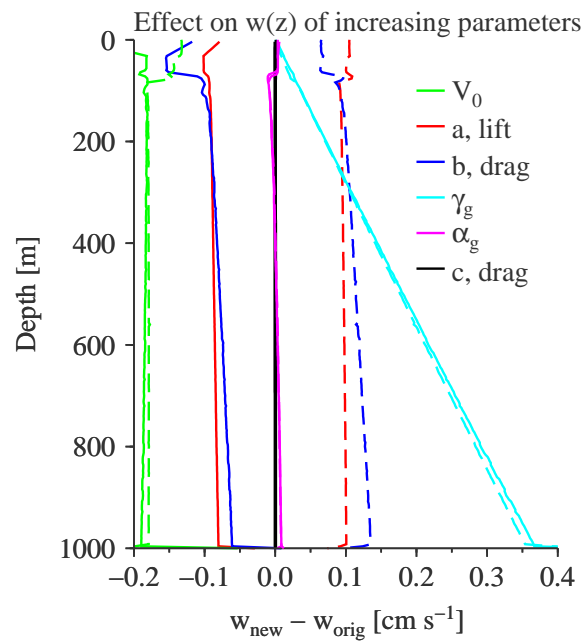


Figure 4.4: Effect of a 5% increase of each parameter (or +5 cc for volume) on vertical velocity profiles ($w_w(z)$), calculated as new vertical velocity profile minus the original. The effect for w_w from glider dives is in solid lines while climbs are dashed.

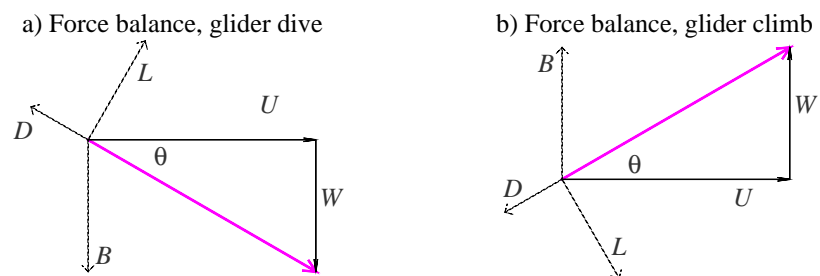


Figure 4.5: Diagram of force balance on the Seaglider, during a dive (a) and during a climb (b). Forces are lift (L), drag (D), and buoyancy (B). The glider velocity is U and W in the x - and z -directions, and θ is the glide angle.

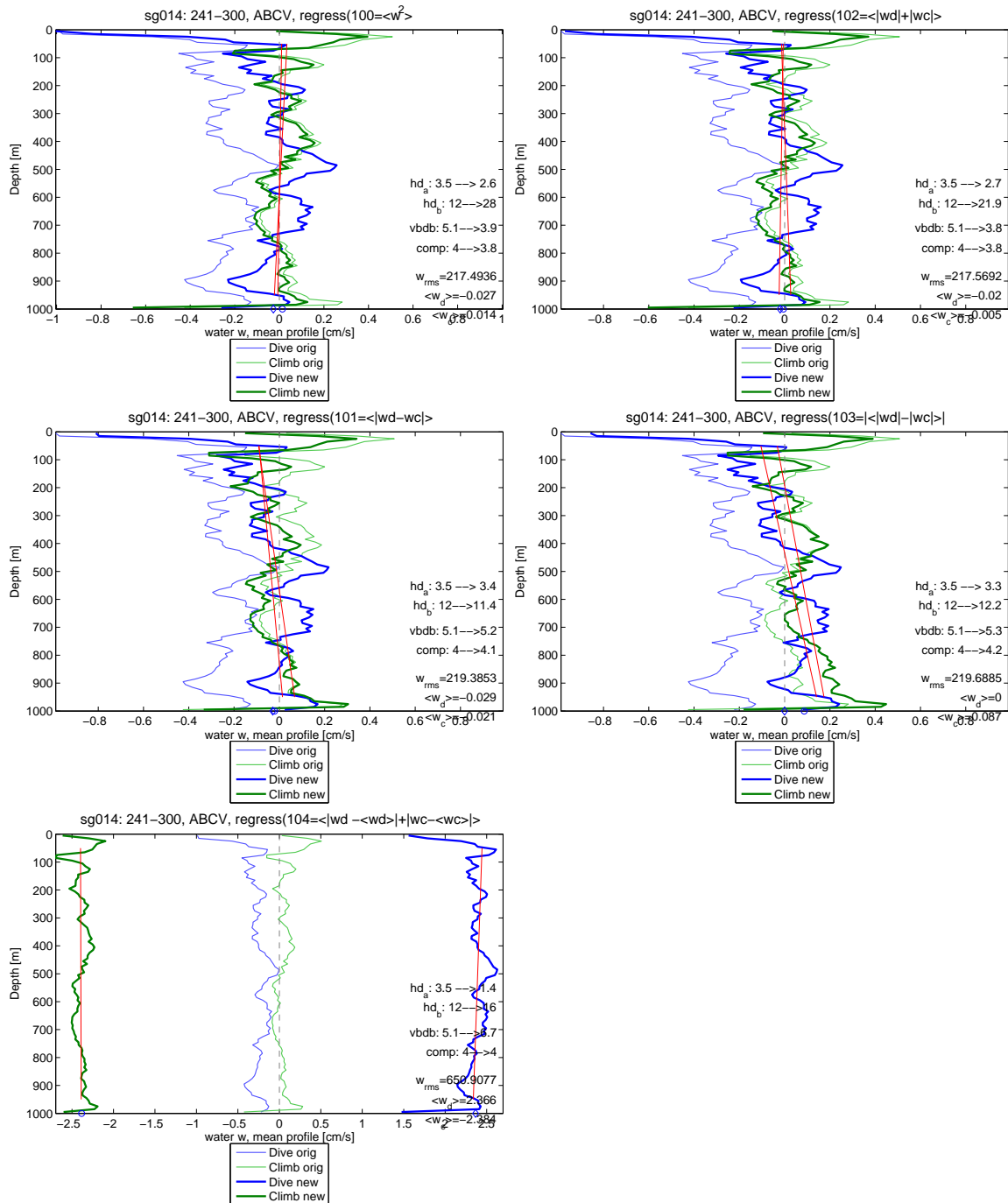


Figure 4.6: Choice of minimization procedures, tested for cycles 241-340 from sg014. Each panel shows the resulting mean profile of vertical velocity estimated during Seaglider dives (blue) and estimated during climbs (green). The red lines are linear trends fit to each profile, showing divergence or offsets. The old and new parameters are in the text of each figure, and the choice of minimization is in the title, corresponding to the list in §4.5.2.

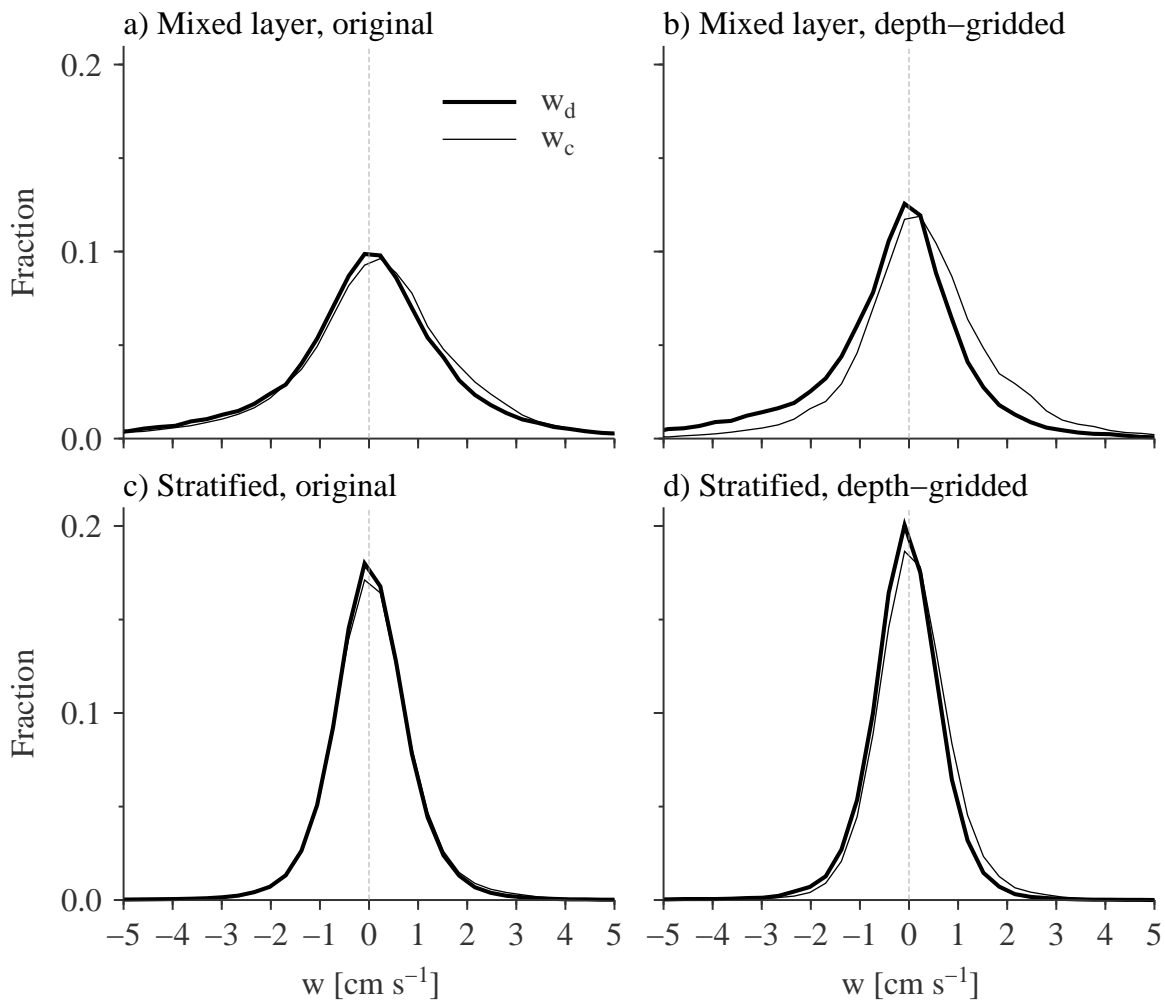


Figure 4.7: Effect of gridding vertical water velocity estimates (w_w) by depth bins before calculating distributions. The left column shows the histogram of original water velocity estimates w_w in the mixed layer (a) and stratified ocean (c). The right column shows the same data, but gridded by depth before calculating histograms, (b) and (d). Transforming w_w profiles onto an evenly spaced depth-grid over-weights downward velocities during dives and upward velocities during climbs.

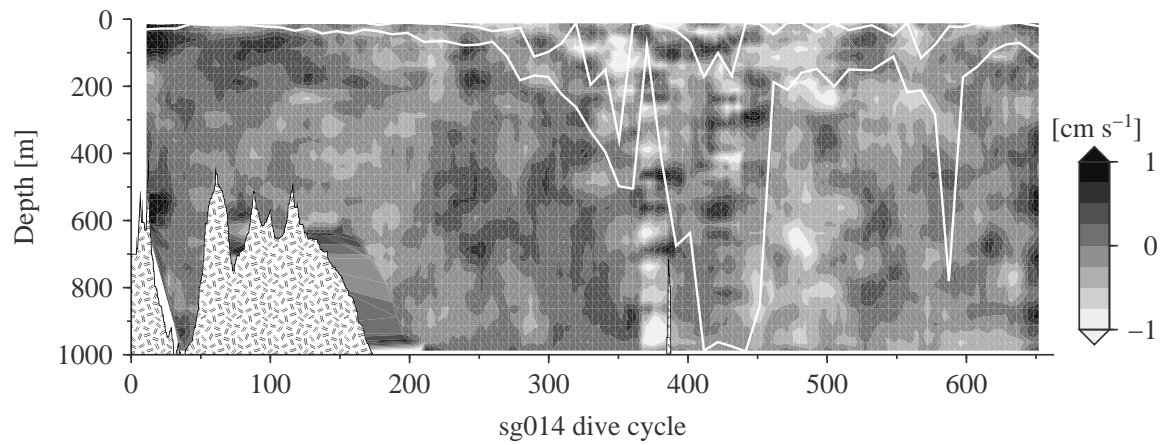


Figure 4.8: Offset between the average profile of vertical water velocity computed over an ensemble of 20 dives and an ensemble of 20 climbs. Black regions means the average velocity profile from dives is more upwards than from the climb. Bathymetry is stippled. Minimum and maximum mixed layer depths observed during each ensemble are overlaid in white.

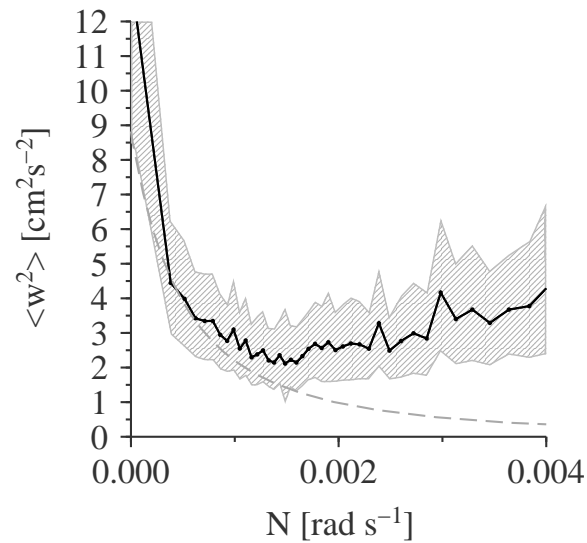


Figure 4.9: WKB-scaling of w_{rms} in the stratified ocean, sg015. Vertical velocity measurements were binned by N . For $N < 0.0013 \text{ rad s}^{-1}$, measurements matched theoretical expectations for a GM-internal wave field, scaling as $\langle w^2 \rangle \approx 0.25N_0/N$. The WKB-scaling breaks for $N > 0.0013 \text{ rad s}^{-1}$.

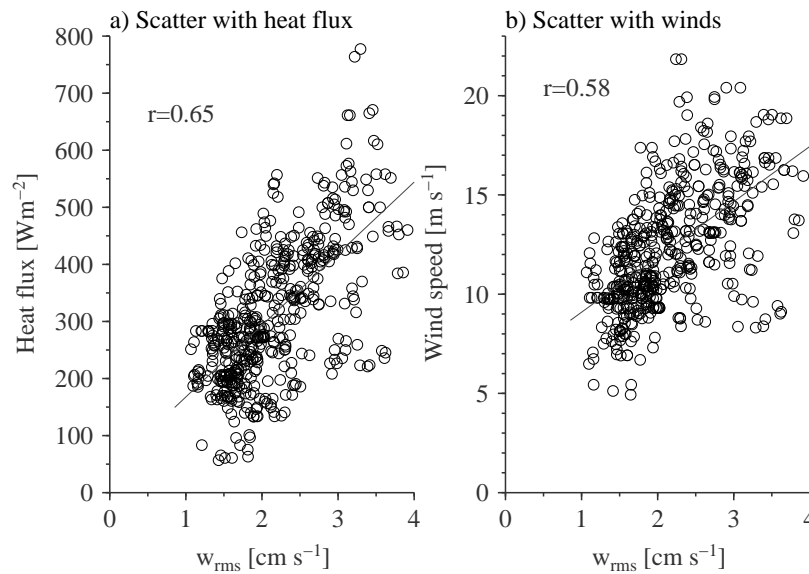


Figure 4.10: Scatterplots of sg015 w_{rms} on heat flux (a) and wind speed (b) for lagged daily averages.

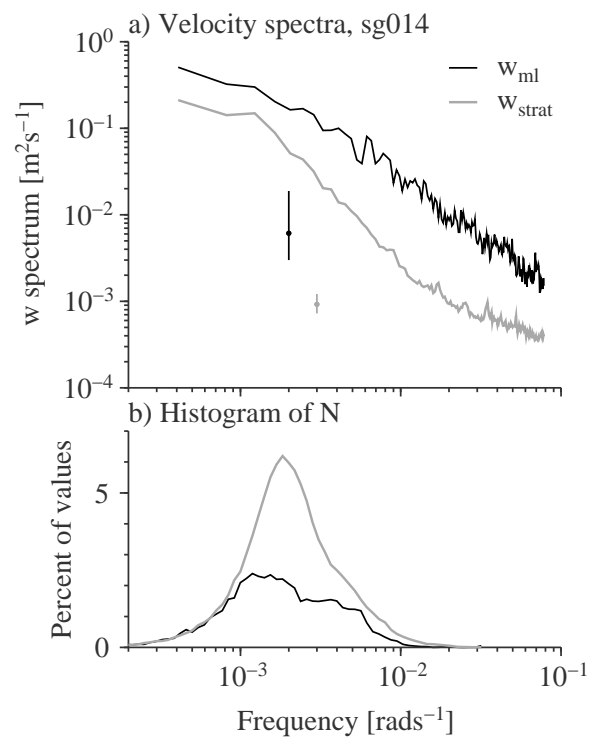


Figure 4.11: Frequency spectrum (a) and histogram of buoyancy frequency N (b). Black curves are from profiles entirely within the mixed layer, while gray curves are from the stratified ocean. 95% confidence bands for the spectra are given by the vertical lines in the corresponding color.

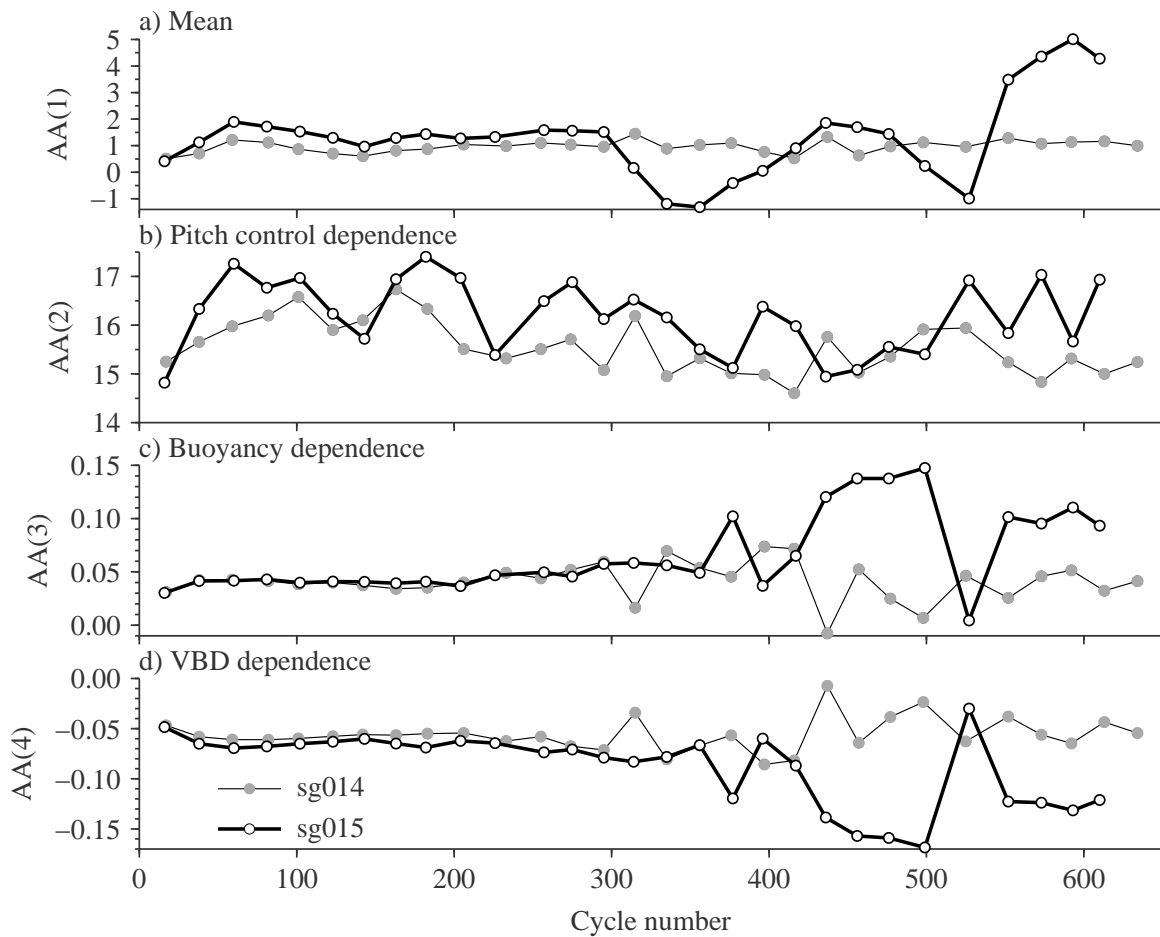


Figure 4.12: Stability of measured pitch related to mean (a), pitch control (b), buoyancy (c) and VBD (d), as described by (4.19), for sg014 (gray) and sg015 (black). The mean (a) is relatively steady for sg014 and for sg015 before dive cycle 300. After dive cycle 300, the mean for sg015 ranges from -2 to 5.

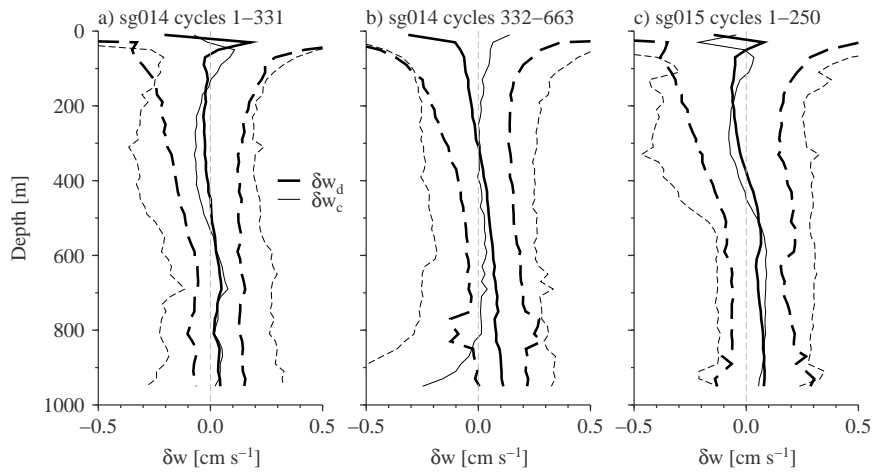


Figure 4.13: Mean change in profiles of vertical velocity (w_w) due to substituting modeled pitch, calculated from (4.19) for measured pitch. Panels are for sg014 cycles 1-331 (a), sg014 cycles 332-663 (b) and sg015 cycles 1-308 (c). Effect of pitch correction procedure on mean profiles of vertical velocity from dives (black) and climbs (gray) and with standard deviations in dashed lines of the same color. The overall change is less than 0.1 cm s^{-1} .

Chapter 5

**VERTICAL VELOCITIES IN THE STRATIFIED AND DEEP CONVECTING
LABRADOR SEA FROM SEAGLIDER, 2004-05****5.1 Introduction**

In most of the world's oceans, the surface thermocline is highly stratified, preventing the free exchange of surface properties and forcings with the abyss. In the Labrador Sea, weak stratification and large wintertime heat losses allow convective overturning to greater than 1000 m deep. Its remote location and intense meteorological and oceanic conditions limit most observations to hydrography and tracer properties after active convection has ended. Notable exceptions include the Labrador Sea Deep Convection Experiment, OWS Bravo and Bravo mooring, and several moorings from IFR in Kiel in the site of deep convection (Avsic et al., 2006). More recently, autonomous profiling floats (Yashayaev and Loder, 2009) and Seagliders have enabled wintertime observations of hydrography (Argo since 2001, Seaglider in 2003-2005) and vertical profiles of vertical velocity (Seaglider). The Seaglider observations are the focus of this chapter.

Deep convection differs from wind-driven mixing in that unstable surface stratification is created by interaction with the atmosphere or ice. In the Labrador Sea, cold, dry air from the Canadian plateau cools the surface, creating a thermal inversion. Dense plumes can descend at speeds of up to 10 cm s^{-1} , reaching deeper than 1000 m. Three conditions are typical of the regions which undergo deep wintertime convection: (1) preconditioning that establishes very low subsurface stratification, (2) strong upward buoyancy fluxes that in the Labrador Sea and Mediterranean are associated with cold, dry winds from over the land, but in other regions may result from an influx of salt via brine rejection from ice formation processes and (3) doming isopycnals associated with a cyclonic circulation. Strong buoyancy fluxes break near-surface stratification, while preconditioning allows the dense plumes to reach more deeply. In the Labrador Sea, the preconditioning may result from the previous year's convection, which typically leaves a bolus of weakly stratified Labrador Sea Water

(LSW) in the central Labrador Sea. Thus, deep convection is likely to exhibit interannual/decadal variability as deep stratification is retained, strengthened or weakened over several years. Cyclonic circulation aids convection by shoaling stratified isopycnals and reducing the overall amount of buoyancy which must be removed in order for the dense plumes to reach the weakly stratified depths.

This buoyancy which must be removed is referred to as convection resistance (CR) (Bailey et al., 2005). CR is the depth-integrated density anomaly above a particular depth h ,

$$CR(h) = \int_{-h}^0 \sigma(S, T, z) dz - \sigma(h) \times h \quad (5.1)$$

with units kgm^{-2} . Multiplying by g/ρ_0 gives $[J/kg]$. Negative values of CR correspond to stable stratification. The contributions to this integrated buoyancy anomaly may be separated by temperature and salinity by substituting a constant salinity or temperature in the calculation of potential density σ . These constituent CRs are

$$CR(h, \bar{S}, T) = \int_{-h}^0 \sigma(\bar{S}, T, z) dz - \sigma(\bar{S}, T, h) \times h \quad (5.2)$$

$$CR(h, S, \bar{T}) = \int_{-h}^0 \sigma(S, \bar{T}, z) dz - \sigma(S, \bar{T}, h) \times h. \quad (5.3)$$

If \bar{S} and \bar{T} are the average salinity and temperature for the profile to depth h and a linear equation of state is used, then complete convection resistance is the sum of the constituent CR s. In the Labrador Sea, stratification is dominated by salinity, and the northern Labrador Sea in particular is blocked from deeply convecting by a relatively fresh surface layer. Convection resistance due to salinity is shown in Fig. 5.1b. CR contours describe the doming isopycnals and preconditioning (nearer to zero is less stratification) while heat flux contour show the region where heat loss is high. The intersection of the two is the region where deep convection is typically found. The intersecting region may be modified by a change in either preconditioning or heat flux patterns. In 2008, for example, the geometry and timing of Labrador shelf ice cover changed, moving the region of highest heat loss towards the center of the doming isopycnals (Våge et al., 2009). The result was some of the deepest convection (> 2000 m) observed in a decade.

Convection occurs over multiple length scales (Marshall and Schott, 1999), ranging from larger convecting patches down to plumes. The local process of vertical mixing is intermittent and spatially inhomogenous, mediated by plumes organized horizontally at scales of less than 1 km, while

the larger convecting patch refers to the general location where plumes may occur. After deep convection ceases, the edges of the bolus of well-mixed water are subject to baroclinic instability, while the middle slumps and finds its neutral buoyancy level.

Convection has been observed in laboratory and numerical models (see review, Marshall and Schott (1999)), and less frequently in the open ocean. Several instruments can observe vertical velocities during convection, each with its own pros and cons. Acoustic Doppler Current Profilers (ADCP) mounted on deep water moorings produce vertical velocity profiles at ~ 20 m vertical resolution at a single location with noise levels ~ 1 cm s $^{-1}$. Limited horizontal information is available from analysis of the beam spreading characteristics. Deep Lagrangian floats give the motion of fluid parcels in the mixed layer with limited horizontal information (Steffen and D'Asaro, 2002). Seagliders estimate vertical velocity along a specified track with a roughly 1:3 vertical to horizontal slope and noise levels somewhat lower than ~ 1 cm s $^{-1}$. Some horizontal and vertical structure information is available, though space and time are aliased. Comparisons between mixed layer and stratified vertical velocities are also possible.

In this chapter, we compare the 2004-05 winter (hereafter called 2005) with preceding and succeeding years. We then examine the high resolution hydrography from Seagliders, as well as the structure, magnitude and distribution of vertical water velocities in stratified regions and in unstratified, convecting regions.

5.2 Data and Processing

5.2.1 Seaglider

The Seaglider is an autonomous underwater vehicle developed at the University of Washington (Eriksen et al., 2001). It navigates using dead reckoning between Global Positioning System (GPS) fixes, transmits data and may receive commands via the Iridium satellite system after each dive-climb cycle. Profiles are made to 1000 m depth with an approximately 1:3 vertical to horizontal slope. Relative to aspect ratios of physical features in the Labrador Sea (e.g. a 100 m mixed layer depth divided by a largest Rossby radius of 10s of kilometers, or the related Prandtl ratio, f/N where f is the Coriolis frequency and N the buoyancy frequency), a 1:3 slope is nearly vertical. The glider typically surfaces 6 km through the water from where its dive began. On its sawtooth

trajectory, the spacing of glider profiles averages 3 km, but nearer the surface and 1000 m depth, sampling is regular but non-equispaced, ranging from 100s of meters to near 6 km. During a single dive-climb cycle, sampling is uniform in time within specified depth intervals, ranging from every 5 s in the top 40 m to every 40 s deeper than 300 m, corresponding roughly to vertical spacing between 0.3 and 2 m at a 0.06 m s^{-1} dive and climb rate.

In this observational program, 5 Seagliders were deployed between October 2003 and August 2005. Seagliders S/N 14 and 15 (hereafter designated as sg014 and sg015), the focus of this chapter, were deployed from Davis Strait on 24 September 2004. Their tracks are shown in Fig. 5.1a, criss-crossing the north Labrador Sea from east to west as they transited southwards. Around 65°N , they switched headings to due south, following 55°W and 58°W . The gliders turned eastward once they reached the 1000 m isobath on the Labrador shelf then traversed the region of deep convection in February before heading northeastwards to be picked up off the Greenland coast. Along the track, the Seagliders measured temperature and conductivity (Sea-Bird Electronics (SBE) custom sensor), pressure (Paine Corporation 211-75-710-05 1500PSIA). Sg015 additionally had fluorescence and optical backscatter (WETlabs custom ECO-BB2F puck), and dissolved oxygen (SBE 43F Clark-type oxygen electrode) sensors, from which data are described in Frajka-Williams et al. (2009). Depth-averaged horizontal velocities are calculated from Seaglider measurements, using a flight model based on Seaglider hydrodynamics and surface positions between two consecutive surfacings with typical error of about 1 cm s^{-1} . Data calibration details are given below.

Salinity

Seaglider uses an unpumped conductivity cell (Sea-Bird Electronics SBE 4 conductivity cell) in order to conserve energy, since power consumed by typical pumped systems is an appreciable fraction of overall Seaglider power consumption. Instead of pumping, Seaglider relies on its motion through the ocean to flush the conductivity cell. For a glider speed between $0.2\text{-}0.5 \text{ m s}^{-1}$, a range typically found on a dive-climb cycle, the cell flushing speed ranges from 0.1 to 0.4 m s^{-1} , considerably slower than typical pumped rates of 2 m s^{-1} . Measurement of temperature just outside the conductivity cell and variable flow rates through the cell result in the need to estimate temperature accurately within the conductivity cell in order to estimate salinity. The first correction is a simple

but variable time lag between when water passes the thermistor to when it fills the measurement volume of the cell. The second is the thermal inertia of the cell which can significantly heat or cool water within the thermal boundary layer along the cell wall, affecting its conductivity.

In order to correct salinity, we needed a model for the cell flushing rate given the glider speed and attack angle, a description of the development of internal boundary layers and the effect of cell geometry on the pressure head between the cell mouth and exit. The cell flushing rate was determined empirically in a flume and depends on cell diameter and geometry. The time offset between the thermistor and cell active volume was calculated as the flow rate vs distance from the thermistor to opening, then as a volume flux through the cell based on the flushing speed.

Using the lags and flush rate, we calculate the average temperature in the active cell associated with the time the water passed the thermistor. The thermal inertia response was modelled following Lueck (1990); Lueck and Picklo (1990). Parameter choices for each glider were determined empirically, by inspection, to reduce unrealistic overturns in the thermocline and differences between dive and climb salinities at the same temperature. Some salinity spikes still remain, in part due to unresolved vertical gradients. These spikes are removed after the other corrections have been applied, using a simple despiking algorithm. Full details of the salinity algorithm are forthcoming (Eriksen, *in prep*).

Vertical velocity

See Chapter 4.

Argo-glider hydrography comparisons

To check glider calibration *in situ*, we found Argo float profiles which were near to gliders in space and time (within 60 km and 10 days). There were 14 pairs of Argo and glider profiles within this radius. Four pairs were within 30 km, approximately the Rossby radius for the region, and 5 days. Fig. 5.2 shows the pairs of glider and Argo profiles nearest in time: Argo float 4900528 matched with sg014, cycle 307 (within 56 km and 2 days) and Argo float 6900274 and sg015, cycle 260 (within 19 km and 4 days). In the deeper layers, salinity and potential temperature at deeper layers agreed within 0.01 and 0.05°C. This agreement is typical of the closest pairs of profiles and is typical

of intrinsic horizontal variability of the deep Labrador Sea. Hence, instrumental accuracy may be better than this.

5.3 *Interannual trends in convection, 2003-2008*

The 2005 convective winter in the Labrador Sea occurred during a period of overall restratification. Using NCEP heat flux estimates from 2002-2008 and Argo float data available during the convective winters of 2003 and 2005-2008, we can estimate the general trends in heat content in the Labrador Sea as well as watermass properties of Labrador Sea Water formed over the 6 year period.

In keeping with other interannual descriptions of convection, we will compare the thickness of pycnostad layers as in Lazier et al. (2002) and $\theta - S$ properties as in Yashayaev (2007). Both of these studies relied on the rich and long timeseries of the repeat hydrographic section across the Labrador Sea known in *World Ocean Circulation Experiment* (WOCE) terminology as AR7W (Yashayaev, 2007). Using Argo allows us to observe convective products during the active winter so we are better able to compare to glider observations during winter.

5.3.1 *Atmospheric forcing*

Cold, dry air off the Canadian continent is a primary driver of the deep convection in the Labrador Sea. Surface buoyancy flux due to atmospheric forcing may be written,

$$B = \frac{g\alpha Q}{c_p} + g\beta(E - P)S \quad (5.4)$$

where Q is heat flux and $E - P$ evaporation minus precipitation. g is gravitational acceleration, α the thermal expansion of seawater, which depends on temperature and salinity S , c_p the specific heat of seawater ($\approx 4 \text{ kJkg}^{-1}\text{K}^{-1}$), and β the haline expansion coefficient. It has been shown that for this region, freshwater flux is a small contributor to the mean buoyancy flux, approximately 3% or -2 Wm^{-2} (Lazier et al., 2002). For this chapter, heat flux is calculated as the sum of NCEP short wave radiation flux, long wave radiation flux, sensible heat flux and latent heat flux, and is in units of Wm^{-2} . Negative sign indicates heat or buoyancy loss from the ocean to the atmosphere.

During the winter, sensible heat dominates, with about -300 Wm^{-2} lost to the atmosphere, while latent heat flux contributes another -150 Wm^{-2} . Longwave radiative flux is low, and nearly constant

at -70 Wm^{-2} . Shortwave insolation is responsible for warming the surface ocean $+80 \text{ Wm}^{-2}$. The spatial location of greatest heat loss is shown in Fig. 5.1b, around 59°N , 58°W . The location of greatest heat loss is seaward of the continental shelf, primarily because the Labrador shelf is ice-covered until late in the spring, shielding the cold atmospheric winds from the relatively warmer water. This location is more stratified than the central Labrador Sea where deepest convection is found (around 56°N , 54°W), as shown by convection resistance (CR) contours in Fig. 5.1b. It is also upstream of the region of deepest convection around the cyclonic circulation in the Labrador Sea, reflecting the time-lag between the heat loss and deep convection as upper-ocean stratification is removed.

For 2002-2008, the heat content anomaly was calculated as a time integral of daily NCEP-NCAR II reanalysis heat fluxes (latent, sensible, shortwave and longwave radiation), as in Lazier et al. (2002). This assumes that lateral heat flux can be neglected. The timeseries of total heatflux in the convection region was used, with the mean removed. Mean values in heat flux contribute a linear trend to the integrated heat anomaly, while removing the mean requires that the beginning and end points of the heat anomaly integral be at the same level. Variations relative to this mean result from seasonal and interannual variations. The heat anomaly in Fig. 5.3 shows a restratifying trend from 2002-2007 that reverses with anomalously high heat loss in 2008.

5.3.2 *LSW properties from Argo hydrography*

Deep convection can be measured by the depth of convection and by variations in the annual vintage of Labrador Sea Water. In the late 1980s to mid-1990s, LSW production was strong and relatively persistent, with LSW volume peaking in winter 1994/95. An abrupt reversal of the NAO and cessation of cold windy winters occurred in 1996, and deep winter convection has been sporadic since. Finally, winter 2007/08 saw the return of convection to 1600 m depth, with the strongest air-sea heat flux since the mid-1990s, in spite of an NAO index that was only moderately positive. Using Argo floats, we calculated the mean properties of potential temperature, salinity and density within the convecting region during deep convection. The mean profiles shown in Fig. 5.4 were calculated following Lazier et al. (2002) by first transferring data in the convection region of $56\text{-}58^\circ\text{N}$, $53\text{-}55^\circ\text{W}$ in April to σ -coordinates, then averaging, before returning to an average depth-grid. The effect

is to reduce variations in properties due to heaving of internal wave surfaces or averaging across isopycnals that are sloped.

The potential temperature in the well-mixed depth range increases between 2003 and 2005-2007 (Fig. 5.4b). This increase in average temperature of LSW corresponds to the restratifying trend (increase in heat) observed by the cumulative heat flux curves of Fig. 5.3. The 2008 convective product is cooler than 2005-2007, though not as cold as 2003. Salinity changes are less noticeable, with the average LSW salinity around 34.83-34.86. Mixed layer depths are best seen in the profiles of potential density, with the deepest ones observed in the 2008 year to 1600 m by our calculation, compared to 1000 m for the other years.

The volume of LSW may be estimated from the minimum vertical density gradient. Following Lazier et al. (2002), we created a histogram of thicknesses in $\sigma_{1.5}$ (potential density anomaly relative to 1500 db) from Argo profiles collected in the ventilated region in the month following the modification of LSW (Fig. 5.5). However, we chose the fixed month of April for our interannual comparison, rather than the deepest convected profiles. It is the earliest month where the $\sigma_{1.5}$ peak in the distribution matches with the summer months, i.e. after surface modification of LSW has ended. Pycnostads are defined as regions where the layer thickness between 0.002 kgm^{-3} intervals is 50 m or greater. This method helps deal with multiple mixed layers often observed during Labrador Sea deep convection, which may be indicative of slantwise convection or interleaving of different well-mixed density classes (Pickart et al., 2002; Väge et al., 2009).

LSW decreases in density from a maximum in 2003 ($\sigma_{1.5} \approx 34.635 \text{ kgm}^{-3}$) to a minimum in 2007 ($\sigma_{1.5} \approx 34.59 - 34.6$) before a striking increase in both density and thickness in 2008 (to $\sigma_{1.5} \approx 34.63 \text{ kgm}^{-3}$). The combination of factors leading to this renewal of deep convection (depths > 2000 m) is described in recent papers (Väge et al., 2009; Yashayaev and Loder, 2009) and will not be discussed here. The 2008 year also showed the most homogenous watermass in April, with a 1360 m total thickness of pycnostads by this calculation. The 2003 year was not far behind with a total thickness of pycnostads of 1270 m. The 2003-2007 years were relatively inhomogeneous in temperature, salinity and density even within the actively convective region. A particular strength of the Seaglider over Argo floats is that it creates high resolution sections of hydrographic properties, with 6 profiles per day to 1000 m, compared with the Argo's single profile to 2000 m every 10 days. These will be discussed further in §5.4.2.

5.4 Glider Observations, 2004-05

Two Seagliders, sg014 and sg015, were deployed from the Davis Strait on September 24, 2004. Their tracks can be seen in Fig. 5.1a. They were directed to make a series of intersecting transects across the northern Labrador Sea. Once they crossed south of roughly 65°N , the gliders were directed southward along neighboring meridians (sg015 on 58°W and sg014 on 55°W) until they reached the Labrador shelf. Sg015 turned east at $56^{\circ}30'\text{N}$ then south to encounter the shelf again. From there it headed northwest but was advected by strong along-shelf currents to the west, before it turned north, then west, then north again. It proceeded north along 55°N , observing 1000+ m mixed layers, before eventually being lost to the sea at the end of March, 2005. When sg014 reached the Labrador shelf at 55°N , it turned northeastward to follow the WOCE AR7W repeat section, then criss-crossed the West Greenland offshore currents (deeper than 1000 m) before being pulled offshore by a powerful eddy. Sg014 was entrained in an Irminger Ring, piloted free eventually then returned to Nuuk to be recovered at the end of April, 2005. These observations are the subject of Hátún et al. (2007) and will not be discussed here.

In the Davis Strait, the gliders profiled between the southward flowing Baffin Island Current (BIC) on the western side of the strait, and the northward flowing West Greenland Current (WGC) on the eastern side of the strait. The BIC is characterized by very fresh, cold surface waters while the WGC contains a signature of remnant Irminger Sea Water (warm and salty) below the surface fresh layer. These two currents can be seen in Fig. 5.6 and Fig. 5.7 hydrographic sections (Mertz et al., 1993; Cuny et al., 2002; Tang et al., 2004).

As the two gliders crossed the 1000 m and 2500 m isobaths travelling south along 58°W (sg015) and 55°W (sg014), they sampled westward directed extensions of the West Greenland Current that turn away from the Greenland coast at the 1000 m and 3000 m isobaths (Cuny et al., 2002). These offshore advective currents appear in both glider records as thick layers of warm, salty Irminger Sea Water (ISW) from about 100-500 m, indicated by the high temperatures (red) in November-December of Figs. 5.6b and 5.7b. The core of this Irminger Sea water weakens as the gliders continue south, but is still found when the gliders encounter the Labrador shelf. Shelf encounters are visible as dark blue regions near the surface in potential temperature in January for Fig. 5.6b and December and January in Fig. 5.7b, and also as steep peaks in bathymetry in (e) panels at the

same times. As each glider leaves the shelf region and crosses the central Labrador Sea, the ISW signature disappears and the deepest convection is observed.

Sg014 sampled its deepest mixed layers (greater than 1000 m) at 58°N, 50°W along the AR7W line, near the end of January. It soon left the region of deep convection, before the largest mixed layer depths of the season were recorded by Argo floats. Sg015 sampled its deepest mixed layers between 56-60°N along 55°W in February. Along this northward track at 59°N it also encountered a stratified eddy surrounded on both sides by 1000 m deep mixed layers, shown in the θ record in Fig. 5.7 in shaded gray. Sg015 also left this region for the freshwater stratified area north of 60°N before deep convection had ended, and neither glider observed the process of restratification.

5.4.1 *Convection hydrography, 2004-05*

Mixed layer depths greater than 200 m were observed from December to February by sg014 and sg015. Both gliders observed mixed layer depths exceeding the full dive depth in late January and early February. They collected approximately 36 and 50 profiles, respectively with mixed layer depths ≥ 1000 m. Sixteen argo profiles were available from January 1-March 1, 2005 within 56.4-59°N and 50 – 55.5°W. Argo profiles are more sparsely distributed since Argo floats only profile every 10 days, returning 50-55 samples per 2000 m profile. Gliders profile to 1000 m approximately 6 times a day, returning 500-750 samples per profile.

5.4.2 *$\theta - S$ variations in deep mixed layers*

In glider profiles of well-mixed deep layers with surface to 1000 m density variations of less than 0.01 kg m^{-3} , the range of average mixed layer temperatures observed were 3.34-3.65°C and 34.83-34.86 from sg014 and sg015 (Fig. 5.8). This span of 0.35°C and 0.03 corresponds to a density difference greater than 0.02 kg m^{-3} (allowing for observed density-compensation) within the convection region. (During this period, sg015 was within 56.4-58.4°N and 54.84-55.44°W and sg014 was in 57-59°N and 50-52°W.) Argo hydrographic profiles immediately after the surface is restratified (Fig. 5.4) give a density change of 0.03 kg m^{-3} from 100 m depth to 1000 m, the center of the newly formed LSW. Thus, the observed horizontal variations in convectively mixed regions are of the same magnitude as the vertical stratification present after deep convection ends. This suggests

that the process of restratification is speeded along by the horizontal variations in density within the mixed patch, rather than requiring lighter water to move from the edge of a large, fully horizontally and vertically mixed patch to restratify.

A stratified eddy encountered by sg015 in the region of deep convection had properties matching those of Irminger Rings (Lilly et al., 2003; Rykova, 2006). Salinities increased within the depth range 100-600 m as the glider profiled 11 times within the eddy. Surface temperatures were 0.5°C warmer than surrounding water. Temperatures and salinities at 900 m were the same as the surrounding convecting areas. Waterfall plots (Fig. 5.9, corresponding to the gray shaded region in Fig. 5.7) show the transition from vertically well-mixed salinity and potential temperature on year day 40 to a stratified region with warm and salty Irminger Sea Water from 100-500 m. The absence of a deeper mixed layer at the surface of the Irminger Ring indicates that it is relatively “young,” experiencing its first winter, as opposed to eddies which have already undergone convection (Rykova, 2006). This eddy is unlike those described by Steffen and D’Asaro (2002) or Gascard and Clarke (1983), both of which were identified with a cold surface layer and deep mixed layers. Instead, the $\sigma_{1.5}$ contours in Fig. 5.9a show a very stratified eddy while the deeper mixed layers are on either side (less than 0.01 kgm⁻³ density variation from the surface to 1000 m). The vertical velocity field in Fig. 5.9c shows high vertical velocities on either side of the eddy and very low vertical velocities within the eddy. These will be discussed further in §5.5.4.

The deepest mixed layers observed by sg014 are shown similarly in Fig. 5.10 for the period highlighted in gray in Fig. 5.6. Contours of $\sigma_{1.5}$ in Fig. 5.10a show weak stratification near 1000 m in all profiles except around day 29-34, and increased stratification near the latter half of the period. Again, vertical velocities are highest in areas with weakest stratification and damped in regions with higher stratification (days 33-38, especially deeper than 500 m).

5.4.3 Heat flux calculated from glider heat content

As in Steffen and D’Asaro (2002), we estimate net atmospheric heat fluxes from observed changes in oceanic heat content, assuming a 1-d column model and that all heating is from the atmosphere. In reality, the situation is 3-d,

$$\frac{dH}{dt} = \vec{u} \cdot \nabla_h H + Q , \quad (5.5)$$

where Q is the surface heat flux, $H = \rho c_p \int \theta dz$ is heat content, \vec{u} is the ocean circulation. Furthermore, Seagliders are not purely Eulerian, and observe heat changes $\partial H / \partial t|_g$ that include the effect of their own velocity u_g through water,

$$\left. \frac{dH}{dt} \right|_g = (\vec{u} + \vec{u}_g) \cdot \nabla_h H + \mathcal{B}_0 . \quad (5.6)$$

Following a method of calculating oceanic heat fluxes in Steffen and D'Asaro (2002), heat content was averaged over the 1000 m of each glider profile, $\rho_0 c_p \bar{\theta}(t)$ where $\bar{\theta}$ where c_p the heat capacity of seawater. Then

$$Q_{est} = \rho_0 c_p \frac{\partial \bar{\theta}(t)}{\partial t} , \quad (5.7)$$

where Q_{est} neglects the transit through spatially variable stratification. The $\rho_0 c_p \bar{\theta}$ time series for sg014 and sg015 are shown in Fig. 5.11a. From September through November there is an apparent increase in heat content even though net heat loss is expected. This is due to the glider moving from the very cold, fresh Davis Strait waters towards the offshore extension of the West Greenland Currents with a strong, warm core of Irminger Sea water. The thickest part of this current was sampled at the peak in heat content, in early November, and can be seen here in the heat content plot as well as in the hydrography in Figs. 5.6 and 5.7. The heat loss estimated from this peak towards the period of deepest convection is -730 to -900 Wm^2 from November through January, three times the estimate from NCEP/NCAR II reanalysis heat fluxes, and is a combination of the atmospheric heat loss and the transit towards regions which have been subjected to higher heat loss and typically devoid of warm, salty Irminger Sea Water. A plot of θ at depths below the mixed layer (not shown) indicate that 500 m θ is increasing along the track in a region isolated from the surface fluxes, then decreasing by about 2°C from the location of highest heat content to the period of deep convection, when mixed layer depths reach past 500 m. This is confirmation of a contribution by the glider flight through horizontal stratification, $u_g \cdot \nabla H$.

For comparison, the same calculation was done with Argo float 4900611 that persisted in the central Labrador basin for 2 consecutive winters, 2005 and 2006. Argo floats spend 10 days following currents around 700-1500 m) before profiling every 10 days. Since they do not have a translational velocity of their own, the heat flux estimates are much closer to those from NCEP and historical measurements, -240 to -260 Wm^{-2} (Fig. 5.11b.). The end result is that due to slow glider speeds, these transects cannot be used to estimate heat flux.

5.5 Vertical velocities measured by Seaglider

Sg014 and sg015 estimated vertical water velocities in the Labrador Sea, leading up to and during deep convection. We focus on two measures of the w field: magnitude (w_{rms} velocity) and length scales (decorrelation length scale along the glider track). From the whole record, rms-speeds in the mixed layer are higher than those in stratified regions (Fig. 5.12a). For each profile, w_{rms} was calculated above and below the mixed layer depth. Smoothing by averaging over 20 dive cycles, mixed layer $w_{rms} \approx 2 \text{ cm s}^{-1}$ while below the mixed layer, it is closer to 1 cm s^{-1} . In the deeper mixed layers in January and February, the w_{rms} velocity is further elevated, and will be discussed further in §5.5.2. An exception to mixed layer w_{rms} exceeding those in the stratified region occurs when sg014 ascends the Labrador shelf in the first half of January. Here, w_{rms} velocities below the mixed layer are relatively higher than in other stratified areas. This is a region of high heat flux and winds, but so are most of the observations. On the shelf, however, the total depth of the water column is only $\sim 400 \text{ m}$, trapping internal wave energy nearer the surface and within the Seaglider observation range more so than for a 4000 m water column.

The second quantification of vertical velocity is the decorrelation length scale. The zero-crossing decorrelation length scale L is defined as the lag τ where the autocorrelation function first crosses zero. While the decorrelation scale was calculated as a function of vertical position, the Seagliders profiled at a 1:3 slope. Fig. 5.13 shows two profiles of vertical velocity, one from sg014 dive cycle 284 in the stratified region (with mixed layer depth of about 40 m) and the other from sg015 dive cycle 482 with mixed layer $> 1000 \text{ m}$. The stratified example (black) has a consistent wavenumber similar to what might be expected for an internal wave, while the unstratified w has higher amplitude variations, shorter scales and downward spikes in w . For comparison, a profile where the mixed layer depth was about 420 m is also shown in red.

Shorter scales are quantified by the lagged autocorrelation in Fig. 5.13b, visible in the earlier decorrelation. For a sinusoid, the zero crossing is exactly $1/4$ times the equivalent wavelength, so that dominant wavelengths are 4 times the zero crossing length. In the stratified region, this length scale is approximately a 350 m scale. By contrast, the length scales in the mixed layer appear to scale with the mixed layer depth. As the mixed layer is deepening in January and February, the mixed layer decorrelation scale also increases. The ratio between length scale and mixed layer

depth is about 1 : 4.

Characteristics of Seaglider vertical velocity observations in the mixed layer and stratified region will be discussed in more detail in the following sections. Different dynamics dominate vertical velocities in stratified as unstratified regions and so are treated separately (§5.5.1 and §5.5.2). Next, we describe observations at two interfaces between stratified and unstratified regions: the transition zone at the base of the mixed layer (§5.5.3) and the stratified Irminger Ring surrounded by 1000 m convectively mixed layers (§5.5.4).

Vertical velocity spectra from the Seaglider

Seaglider travels at approximately a 1:3 vertical to horizontal slope, $10\text{-}25\text{ cm s}^{-1}$ or about $3\text{-}8\text{ cm s}^{-1}$ vertically. The Garrett-Munk model spectra for internal waves were derived for Eulerian measurements as from a mooring or bottom-mounted instrument. The glider velocity results in aliasing of the observed vertical velocity energy between frequency and wavenumber space. Fig. 5.14 shows the canonical GM76 vertical velocity spectrum in frequency and vertical wavenumber space. The expected vertical velocity frequency spectrum for internal waves ($\omega < N$) is roughly white while above N , not shown in Fig. 5.14, the $-5/3$ slope is expected for both frequency and wavenumber. The phase speed corresponding to a 6 cm s^{-1} glider velocity is marked in magenta. The glider traveling on a slant path observes a combination of variability in the vertical, horizontal and time. For hydrostatic eddies and waves, with large to submesoscale lateral scale, typically the aspect ratio $H/L \ll 1$ so that for such motions the glider is effectively moving vertically. At smaller scales, higher frequency motions may be more isotropic and tend to be higher frequency, in which case the glider samples across all three coordinates x , z and t .

Even so, frequency spectra of vertical velocity were calculated from glider profiles in the mixed layer and below the mixed layer. Data were first subsampled to the longest sampling interval, 40 s for sg014 and sg015, and only profiles with at least 256 data records at the reduced sampling rate were used. For sg014, there were 19 such profiles in the mixed layer and 39 in stratified water. Spectra were averaged together producing the estimate in Fig. 5.15a. Higher energy is visible in the mixed layer than below by about a decade. The histograms of buoyancy frequency values for the two sets of profiles are in Fig. 5.15b. By construction of the mixed layer, N is larger for the

profiles taken below the mixed layer. Variations in N affect the calculated slopes, here about $-5/3$ in the mixed layer and somewhat whiter in the stratified profiles. At frequencies $> 0.0126 \text{ rad s}^{-1}$, measurement noise increases, as can be seen by high frequency rolloff in the spectrum of stratified w . Variance from $0.0126 \text{ rad s}^{-1}$ to the Nyquist frequency corresponds to a standard deviation of 0.6 cm s^{-1} , roughly the noise estimate for these data.

Velocity spectra from a mooring-mounted ADCP

The Sonderforschungsbereich (SFB) 460 group at the Leibniz-Institut für Meereswissenschaften at the University of Kiel (IFM-GEOMAR) maintains several long-term oceanographic moorings, one of them being the K1 site in the central Labrador Sea ($56^{\circ}33.6'N$, $52^{\circ}39.5'W$) (Avsic et al., 2006). They were equipped with a combination of upward looking ADCPs (Teledyne RD Instruments, Poway, California, United States), acoustic current meters (ACM, Aanderaa Data Instruments, Bergen, Norway) and SeaCats (Sea-Bird Electronics Inc., Bellevue, Washington, United States). One of these moorings, called K1 recorded data from August 10, 1996 through May 25, 1997 sampling deep convection in 1997 near where Seagliders observed convection in 2005. Vertical velocities from these ADCPs have a negative bias (mean w is less than zero), Fig. 5.16a. We compare velocity spectra from the K1 ADCP measurements with those from Seaglider. Mooring measurements are affected by large-scale advection past the instruments, resulting in Doppler-shifting of observed frequencies. Thus, while we think of mooring measurements as being clearly Eulerian, Doppler-shifting of frequencies again aliases horizontal structure onto temporal variation. This can be used profitably with moorings embedded in strong mean flows or strong eddies, to estimate horizontal scales. The existence of strong near-inertial/tidal peaks in the mooring spectrum does suggest the lateral scale of these motions is quite large.

The mixed layer position was estimated by comparing 75 m and 425 m SeaCat salinities, shown in Fig. 5.16b. When salinities matched within 0.01, the mixed layer was $> 425 \text{ m}$ and when they differed, it was shallower than 425 m. Mixed layers $> 425 \text{ m}$ were observed from February 10-March 17, 1997. The preceding 35 day period (January 6-February 10, 1997) was used for the stratified comparison. Before the mixed layer depth exceeded 425 m, the two velocity time series show lower magnitudes, Fig. 5.16a. After the mixed layer depth exceeded 425 m, intermittent

large-amplitude downward spikes and vertical coherence of vertical velocities are apparent. The velocity time series was from the 17.4 m ADCP bin centered at 313.4 m. RMS-speeds for the stratified region were mean \pm standard deviation of $w_{rms} \approx 1.3 \pm 2.7$ and horizontal $u_{rms} \approx 8.3 \pm 243.1$ cm s⁻¹, while in the unstratified region they were $w_{rms} \approx 1.7 \pm 6.8$ and horizontal $u_{rms} = 7.7 \pm 186.8$ cm s⁻¹, (using 2529 measurements, every 20 min, for each). In the lab, vertical velocities in the mixed layer are approximately 1.5 times horizontal velocities, but the energetic mesoscale is absent in the lab. The vertical structure of w shows high correlation over O(100 m) separation and marginal correlation over the whole mixed layer. Thus, there is some vertical coherence to the plumes though not as extensive as seen in idealized models.

Velocity spectra were calculated by dividing each 35 day vertical velocity time series into 24 segments, calculating the spectra, then averaging. See Fig. 5.16c. Vertical lines indicate the Coriolis parameter, $f \approx 1.2 \times 10^{-4}$ rad s⁻¹ (14.34 hr), very near the semidiurnal tide, $M_2 \approx 1.4 \times 10^{-4}$ rad s⁻¹ (12.42 hr). The near-inertial peak is visible in the horizontal energy spectra, both below and above the mixed layer depth. Above the inertial frequency, the GM model for randomly phased internal waves predicts an -2 slope for horizontal energy spectra and a white spectrum for vertical energy (Garrett and Munk, 1972, 1975, 1979; Gregg and Kunze, 1991). Above the buoyancy frequency, unknown here due to missing SeaCat temperature data, one expects a $-5/3$ red spectrum for both horizontal and vertical velocities. At frequencies > 0.0126 rad s⁻¹, the mixed layer vertical velocity spectrum flattens, indicating the presence of measurement noise. Variance from 0.0126 rad s⁻¹ to the Nyquist frequency corresponds to a standard deviation of roughly 0.6 cm s⁻¹, the estimated measurement noise.

5.5.1 Vertical velocities in the stratified ocean

Most of the kinetic energy in the ocean is along isopycnals. Significant vertical velocities exist in the surface mixed layer, in fronts, during wave breaking events, and near topography. Smaller magnitude vertical velocities exist in the stratified ocean interior due to internal waves. The velocity spectrum is described fairly well in most places by the Garrett-Munk spectrum (Garrett and Munk, 1972, 1975, 1979; Gregg and Kunze, 1991). Internal wave kinetic energy is partitioned into horizontal and vertical components by the aspect ratio of waves which depends on their frequency via

the dispersion relation,

$$\frac{k_h^2}{k_z^2} = \frac{\omega^2 - f^2}{N^2 - \omega^2}, \quad (5.8)$$

where k_h and k_z are the horizontal and vertical wavenumbers, ω the wave frequency, f the Coriolis parameter, and N the buoyancy frequency. Freely propagating waves (with real wavenumbers) are constrained to have frequencies between the Coriolis and buoyancy frequency, typically satisfying $f < \omega < N$. When the wave frequency is near the buoyancy frequency ($\omega \approx N$), motions are more vertical than horizontal while near-inertial waves ($\omega \approx f$) have motion concentrated in the horizontal. When $N \approx f$, there are no internal waves at all. Internal wave energy spectra are peaked at the near-inertial frequency in horizontal velocities, decreasing with increasing frequency, but the internal wave aspect ratio tends to whiten the frequency spectrum of vertical velocity energy.

Velocity variances depend on stratification, described by WKBJ-scaling. For vertical velocities in a GM model ocean, this relationship can be written as

$$\langle w^2 \rangle = c_{GM} \frac{N_0}{N}, \quad (5.9)$$

where $N_0 = 5.2 \times 10^{-3} \text{ rad s}^{-1}$ is the canonical pycnocline stratification and $c_{GM} = 0.25 \text{ cm}^2 \text{ s}^{-2}$ the coefficient for GM energy levels (Munk, 1981). We tested (5.9) using Seaglider velocities, binning w measurements by N to compute $\langle w^2 \rangle$ in each bin. Thirty bins were chosen with nearly the same number of measurements in each. The resulting estimate of c_{GM} was close to the 0.25 coefficient for $N < 0.0013 \text{ rad s}^{-1}$ (Fig. 5.17). The agreement is confirmation that Seaglider estimates of vertical velocities are reasonable.

Since tides and winds are the primary energy sources for internal waves, and tides are relatively stationary, we further separated measurements by the concurrent surface wind speeds from Yu and Weller (2007). The result is a weak dependence of c_{GM} on wind speed. When separated into 6 wind bins from 0-20 m s^{-1} , c_{GM} ranged from 0.15-0.4, generally increasing with wind speed with the exception of a lower estimated c_{GM} around 15 m s^{-1} . Using just 2 wind bins ($u_{wnd} < 10 \text{ m s}^{-1}$ and $u_{wnd} > 10 \text{ m s}^{-1}$), c_{GM} is slightly higher for the higher winds (Fig. 5.18). Each point on the plot is an estimate of $\langle w^2 \rangle$ from approximately 3000 individual measurements. For $N > 0.0013 \text{ rad s}^{-1}$, in the seasonal pycnocline, the estimated c_{GM} diverges from the predicted scaling (5.9). Vertical velocity variance at higher N are above those predicted by the stratification alone. Details and possible causes will be discussed further in §5.5.3.

5.5.2 Vertical velocities in the surface mixed layer

Mean profiles, variance and skewness

Asymmetries between upward and downward velocities are expected during deep convection, in particular that downward velocities are more intense and localized while the return upwelling is weaker and more diffuse (Marshall and Schott, 1999). This has been observed for velocities measured by an ADCP on a mooring, as well as in lab experiments (Coates et al., 1995; Maxworthy and Narimousa, 1994), and appears in observations as a negative skewness of the velocity measurements. Negative skewness indicates that downward plumes are typically of higher magnitude than upward plumes, which is predicted by numerical models of convection. Lab results have shown that plumes entrain fluid as they descend, widening and decelerating. As a result, expected mean profiles of vertical velocity are near zero, variance is elevated near the surface and skewness is negative.

We calculated these quantities in scaled depth coordinates (z/MLD) for vertical velocity measurements from sg014 for profiles with a mixed layer depth from 400-990 m. (We neglected profiles with mixed layer depths > 1000 m since we cannot scale them properly). Mean profiles of vertical velocity are near zero (Fig. 5.19a). Variance profiles, calculated from profiles of w after removing the mean profile, is intensified near the surface though glider estimates in the top 20-50 m near the surface turnaround point are suspect since the steady state assumption of glider flight is violated here. Skewness is negative, but noisy. Variance profiles compare well with estimates from LES and DLF (Harcourt et al., 2002), though our estimate is more surface intensified than those from the model and floats, possibly due to differences in how we calculate mixed layer depth. Slight changes in density—too small to constitute the mixed layer depth by our algorithm—are associated with damped vertical velocities (Fig. 5.10); the true depth to which convective plumes reach may be shallower than our estimated mixed layer depth. Data from Lagrangian floats, on the other hand, were used to estimate velocity within the more strongly mixing region and period only (Steffen and D’Asaro, 2002).

Relationship to wind and buoyancy forcing

The mixed layer is usually created by mechanically driven wind mixing or diurnal convection, but these processes are typically limited to a few tens of meters up to a couple hundred meters in

hurricanes. Deep convection, resulting from unstable density gradients created by extreme buoyancy flux can result in overturns past 1000 m deep. Two scalings for how vertical velocities relate to buoyancy flux are

$$w_*^3 \propto B_0 H, \text{ non-rotating, 1-d} \quad (5.10)$$

$$w_*^2 \propto B_0 / f, \text{ rotating,} \quad (5.11)$$

where B_0 is the surface buoyancy flux, H the mixed layer depth, f the Coriolis parameter and w_* the velocity scaling (Fernando et al., 1991; Maxworthy and Narimousa, 1994; Jones and Marshall, 1993; Steffen and D'Asaro, 2002). Rotational effects become important for small Rossby numbers, $Ro_* = B_0^{1/2} / f^{3/2} H$, when the advective timescale for the non-rotating velocity to transit the mixed layer H is long enough for rotational effects to be felt. In the lab, plumes were observed to follow non-rotating scalings near the surface before evolving into rotationally-stiffened columns at depth (Marshall and Schott, 1999).

Testing the convective scalings with Seaglider observations of w , we used the Yu and Weller ocean flux product (hereafter called YW) (Yu and Weller, 2007). Heat fluxes at the glider's position were estimated from the YW product, which is available daily on a $1 \times 1^\circ$ grid. Sg014 and sg015 only travel about 18 km a day, but if one crossed between two of the 1° boxes in the YW estimate, a weighted average of the winds and heat fluxes from the 2 boxes was used. Mixed layer rms-vertical speeds were calculated during 1-day periods corresponding to the YW product. Time series of YW winds, heat flux and sg015 w_{rms} are shown in Fig. 5.20b. Wind levels ranged from 5-20 m s^{-1} over the 3-month period, but with no large linear trend. Heat fluxes decreased at the glider position at the end of February. At this time, the glider was at 60°N , 55°W , leaving the region of deep convection. The three time series covary before about February 20, 2005. The glider shelf crossing, in the first half of January, marked by very shallow mixed layer depths in panel (a), does not appear to have different w_{rms} levels.

Lag correlations between w_{rms} and winds and between w_{rms} and heat flux were calculated for the record from January 1-February 20, 2005 (Fig. 5.20a). The best lag relationship was for w_{rms} approximately 0.6 and 0.7 days after heat fluxes and wind forcing, respectively, with r^2 values of 0.42 and 0.34 (Fig. 5.21). Heat fluxes correlated better with velocity variance than did winds. Scatterplots for the lagged series are shown in Fig. 5.22.

The lag relationship between vertical velocity, winds and heat flux is somewhat different from that found by Steffen and D’Asaro (2002) using deep Lagrangian floats in the convective winters of 1997 and 1998. Heat flux was a much stronger predictor of vertical velocities in the mixed layer than wind fluxes, and than our Seaglider estimates. Heat flux-vertical velocity variance had an $r^2 \approx 0.9$ at a half-day lag, while winds-vertical velocity variance had an $r^2 \approx 0.6$. The optimal lag between vertical velocity and forcing was 0.5 and 0.75 days for their two years of measurements.

One possible explanation for the increased skill of heat fluxes and winds in predicting vertical velocities seen by Steffen and D’Asaro (2002) is their improved meteorological product, a 4-times-daily modified NCEP/NCAR II reanalysis product (Renfrew et al., 2002). This product had been corrected to more closely match shipboard meteorological observations since NCEP/NCAR heat fluxes as well as ECMWF product were found to be significantly off in the Labrador Sea (Sathiyamoorthy and Moore, 2002). Another difference between the work with Lagrangian floats and our gliders is that vertical velocities from the deep Lagrangian float are in the actively mixing mixed layer only; floats move with water parcels by construction, and may be converged into convecting regions more than the glider sampling patterns. Even so, the linear fits of glider vertical velocities with heat flux and wind (Fig. 5.22) agree quite well with their Fig. 15 for 1997 and 1998.

The dependence on rotational vs non-rotational control was tested during the Labrador Sea Convection experiment using the velocities observed on the deep Lagrangian floats (Steffen and D’Asaro, 2002). Vertical velocities were found to scale with a combination of the 1-d and rotational effects, with improved skill over simple heat flux and wind forcings. Initial estimates of the rotational vs non-rotational scalings for glider estimates of vertical velocity give a weaker relationship than do the correlations with heat flux and winds alone.

5.5.3 *Energy levels in the transition zone at the mixed layer base*

Vertical velocity variance diverges from simple WKB-scaling at high N with energy levels in w much higher than predicted (Fig. 5.18). The record of N and WKB-scaled rms-vertical speeds from sg015 (Fig. 5.23) show that the regions where $c \approx \langle w^2 \rangle / N / N_0$ exceed the canonical $c_{GM} = 0.25$ are just below the mixed layer base, especially in the Davis Strait and northwest Labrador Sea (October-December) and in the stratified Labrador Shelf waters (mid December and early January).

After deep convection, stratification is lower and the break in scaling less apparent.

The region just below the mixed layer and extending for several tens to ~ 200 meters with elevated stratification is the seasonal pycnocline, also known as the “transition zone” between the surface unstratified layer and the stratified interior. The elevated density gradient appears as a peak in the buoyancy frequency profile. The profile of N averaged over dive cycles 50-200 from sg015 is in Fig. 5.24b. This region has high N and $\langle \omega^2 \rangle > N/N_0$ in Fig. 5.23a and b. The transition zone is the region through which wind driven energy in the mixed layer must pass in order to generate internal waves in the abyssal ocean. Two physical regimes may be occurring. At a very stratified mixed layer base, the ocean may behave essentially as 2-layers, supporting interfacial waves. In a strong pycnocline, there may also be a peak in buoyancy frequency N which has interesting effects on the internal wave band ($f < \omega < N$).

At the base of the mixed layer, if the N profile is discontinuous, the fluid may support interfacial waves. In practice, the ocean stratification is always continuous, though a large change in density over a narrow depth band at the mixed layer base may still permit interfacial waves. This would appear as a higher vertical velocity variance or spike at the peak in N , corresponding to upwelling or downwelling experienced by the glider right on the interface. The magnitude of the velocity would likely be constrained by energy levels in the mixed layer at that location or nearby, since the turbulent mixed layer motions bumping on the stratified layer below would create the interfacial wave. Fig. 5.24 shows an average of 150 cycles (300 profiles) of vertical velocity variance and buoyancy frequency N . Profiles were aligned by mixed layer depth so that depth on the y-axis refers to distance below the mixed layer depth for each profile.

A strongly stratified transition zone, with a peak in N , can also act as an internal wave guide—a depth band of elevated N with lower N above and below (Eriksen, 1978; Desaubies and Gregg, 1981). In the early portion of sg014 hydrographic record, the vertical profile of $N(z)$ is near zero in the surface mixed layer, increases sharply in the seasonal pycnocline (N_{max}) then decreases again to a background stratification in the ocean interior (N_1 , Fig. 5.24b). Within the pycnocline, elevated N increases the width of the internal wave frequency band, $f < \omega < N_{max}$. Freely propagating internal waves with frequency between $N_1 < \omega < N_{max}$ can persist within the pycnocline, but not above or below. As they propagate towards the mixed layer ($N \approx 0$ or the deep interior (N_1)) they encounter a turning point and energy is reflected away from the low stratification. Mode solutions

can be constructed to fit within the waveguide though with a pycnocline only a few 10 s of meters thick, observations of wave modes can be hard to distinguish. The source of energy for these waves is the mixed layer, and peak energy levels appear to be bounded by mixed layer energy (Fig. 5.24a). After deep convection, from mid-February and later, the profile of buoyancy frequency below the mixed layer does not have this peak (Fig. 5.23a). Correspondingly, the vertical velocities are not peaked in this region.

5.5.4 Stratified eddy surrounded by deep convection

During deep convection, sg015 observed a stratified Irminger Ring at 59°N, 55°W surrounded by fully 1000 m deep mixed layers, visible in the waterfall plot in Fig. 5.9 corresponding to the shaded region in Fig. 5.7. From the discussion of vertical velocities in the stratified ocean (§5.5.1), internal waves are supported in the frequency band $f < \omega < N$. At the eddy location, $f = 1.24 \times 10^{-4} \text{ rad s}^{-1}$. Within the eddy, from 100-300 m, the buoyancy frequency $N \approx 1.4 \times 10^{-3} \text{ rad s}^{-1}$. Outside the eddy, N is barely distinguishable from f . Similar to the transition zone at the base of the mixed layer, we have a stratified region (the pycnocline or the eddy) adjacent to an unstratified region (the surface mixed layer or deep convecting mixed layers). Unlike the transition zone, here, $N \rightarrow 0$ in the horizontal direction. Because the eddy has a rotational velocity, there is the additional influence of a local f_{eff} that is modified by the eddy's rotation.

Average profiles of salinity, potential temperature, N and w variance are shown in Fig. 5.25 for inside the eddy and on either side of the eddy. Inside the eddy, there is a clear peak in salinity at 350-400 m and 34.865, about 0.015 greater than outside the eddy. Potential temperature inside the eddy is stratified and increasing towards the surface 100 m, with a maximum of 4°C near the center of the eddy in the surface mixed layer. Interestingly, the effects of the strong buoyancy forcing that drive deep convection on either side of the eddy are not yet apparent in the stratification within the eddy. The result is relatively high N in the top 400 m of the eddy as compared to the surrounding convecting region. Concurrent profiles of w show much higher variance on either side of the eddy than within, which is repeated in the mean profiles of w^2 in panel (d): outside the eddy, $\langle w^2 \rangle \approx 4 - 16 \text{ cm}^2 \text{ s}^{-2}$ while inside the eddy, $\langle w^2 \rangle < 1 \text{ cm}^2 \text{ s}^{-2}$.

In examining vertical velocity energy in the stratified ocean (§5.5.1), we found that $\langle w^2 \rangle$

scales with the inverse of N except for $N > 0.0013 \text{ rad s}^{-1}$ where $\langle w^2 \rangle$ was elevated. Figure. 5.26 plots the entire mission of $\langle w^2 \rangle$ against N in black, and observations from the eddy and actively convection region in red and white circles, respectively. In the eddy, $\langle w^2 \rangle$ is well below the curve for the rest of the stratified Labrador Sea.

Several factors may contribute to reduced vertical velocity energy within the stratified eddy. The range of supported frequencies is much wider within the eddy than in the convective region without, where N approaches f . While the horizontal scale of the eddy (20-30 km) may limit the wavelengths that persist within the eddy, near N waves have small horizontal scale and propagate vertically. Smaller scales do, however, correspond to higher dissipation rates. The gradients in N , decreasing with increasing distance from the center of the eddy, may result in critical layers at the edges of the eddy. As a wave packet approaches the edge of the eddy and region of deep convection, N approaches f or even zero. A wave packet conserving frequency ω , originally between f and some higher N within the eddy, will tilt to have near vertical motion as N along the ray path approaches ω . Critical layers result in high dissipation due to increasing wavenumbers of waves.

One potential sign of critical layers here are the lower energy within the eddy, resulting from increased internal wave energy dissipation. One might also expect that w energy should be high at the edge of the eddy, where wave energy becomes primarily vertical. However, this can be difficult to distinguish from the high vertical velocities outside the eddy, in the actively convecting region. Horizontal slices through N and $\langle w^2 \rangle$ at particular depths do not show a clear peak in vertical velocity energy before the actively convecting region is reached. These observations of vertical velocities in a stratified Irminger Ring surrounded by deep convection are unique. Other observations of Irminger Rings, while perhaps slightly more stratified than surrounding waters, do not have the complete separation of the freely propagating internal wave frequency band.

5.6 Conclusions

Two Seagliders observed the 2005 convective winter in the Labrador Sea. Their high resolution sections of hydrography provided an unprecedented view of the horizontal variability in watermasses within a region of deep convection, with a horizontal range of 0.02 kg m^{-3} observed within a small area, suggesting that rapid restratification after deep convection, to a vertical difference in $\sigma_{1.5}$ from

100 to 1000 m could be accomplished by interleaving of density classes found within the convection region, rather than lateral transport over long distances from the edge of the convective patch to the center.

This glider record Labrador Sea provides a new set of observations with which to test theoretical scalings for vertical velocities. While deciphering the space-time aliasing of a hydrographic section which crosses 2000 km in 6 months is tricky, the range of observations also provides a snapshot of vertical velocities in the stratified region, during deep convection, within the transition zone at the base of the mixed layer, and in a stratified eddy surrounded by convection.

Within the stratified ocean, for $N < 0.0013 \text{ rad s}^{-1}$, vertical velocity variance scaled with $1/N$, with a higher energy level when wind levels were higher. This scaling breaks down for $N > 0.0013 \text{ rad s}^{-1}$, within the stratified pycnocline. In the $\sim 40 \text{ m}$ directly beneath the mixed layer, rms-vertical velocities were nearly as high as within the mixed layer above. Over the thicker stratified pycnocline, 50-250 m below the mixed layer, especially in the Davis Strait, energy levels were elevated above the WKB-scaling.

In the unstratified mixed layer, during deep convection, rms-vertical velocities were found to scale with heat flux and winds, with a 0.6 and 0.7 day lag. The r -values were approximately 0.5 and 0.4, respectively, lower than those found by Steffen and D'Asaro (2002), but with similar slopes and y-intercepts to the linear fit. A stratified Irminger Ring was observed surrounded by 1000 m mixed layers. Within this stratified eddy, vertical velocities were much smaller than the WKB-scaling present in the general stratified ocean. Just outside the eddy, vertical velocities were approximately $3 \text{ cm}^2 \text{ s}^{-2}$, 2-3 times higher than in the eddy ($0.5 \text{ cm}^2 \text{ s}^{-2}$).

5.7 Figures

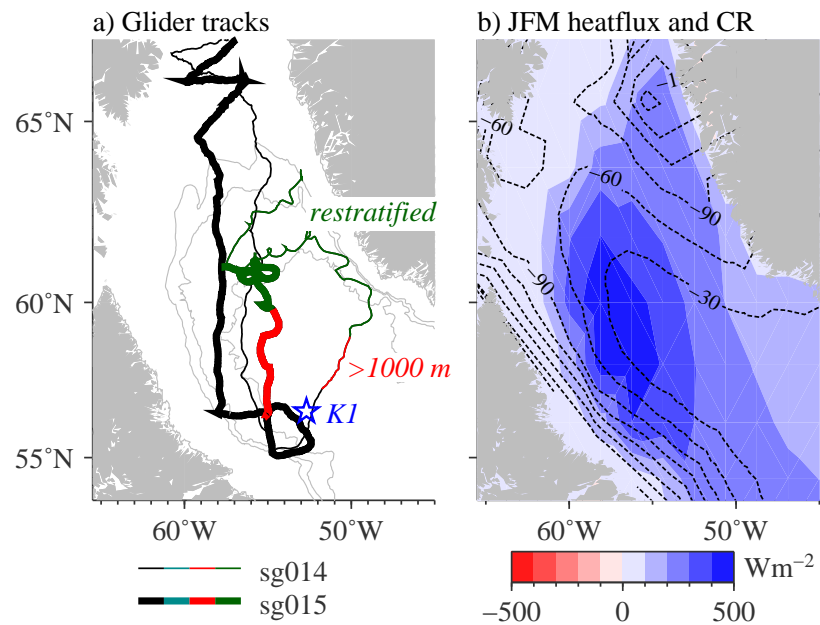


Figure 5.1: (a) Map of the Labrador Sea with Seaglider tracks, sg014 (thin) and sg015 (thick). Regions with mixed layer depths greater than 1000 m are in red, while the restratified region post-deep convection is in green. (b) Average winter heat fluxes (latent and sensible heat fluxes, net long wave and net short wave radiation) are in blue shading. Greater heat loss to the atmosphere (oceanic cooling) is in more saturated blue. Salinity convection resistance, the surface to 500 m buoyancy anomaly due to salinity variations in March, is contoured in dashed lines. Negative convection resistance indicates haline stratified (relatively fresh water above 500 m as compared to at 500 m). The blue star in (a) indicates the position of the K1 mooring.

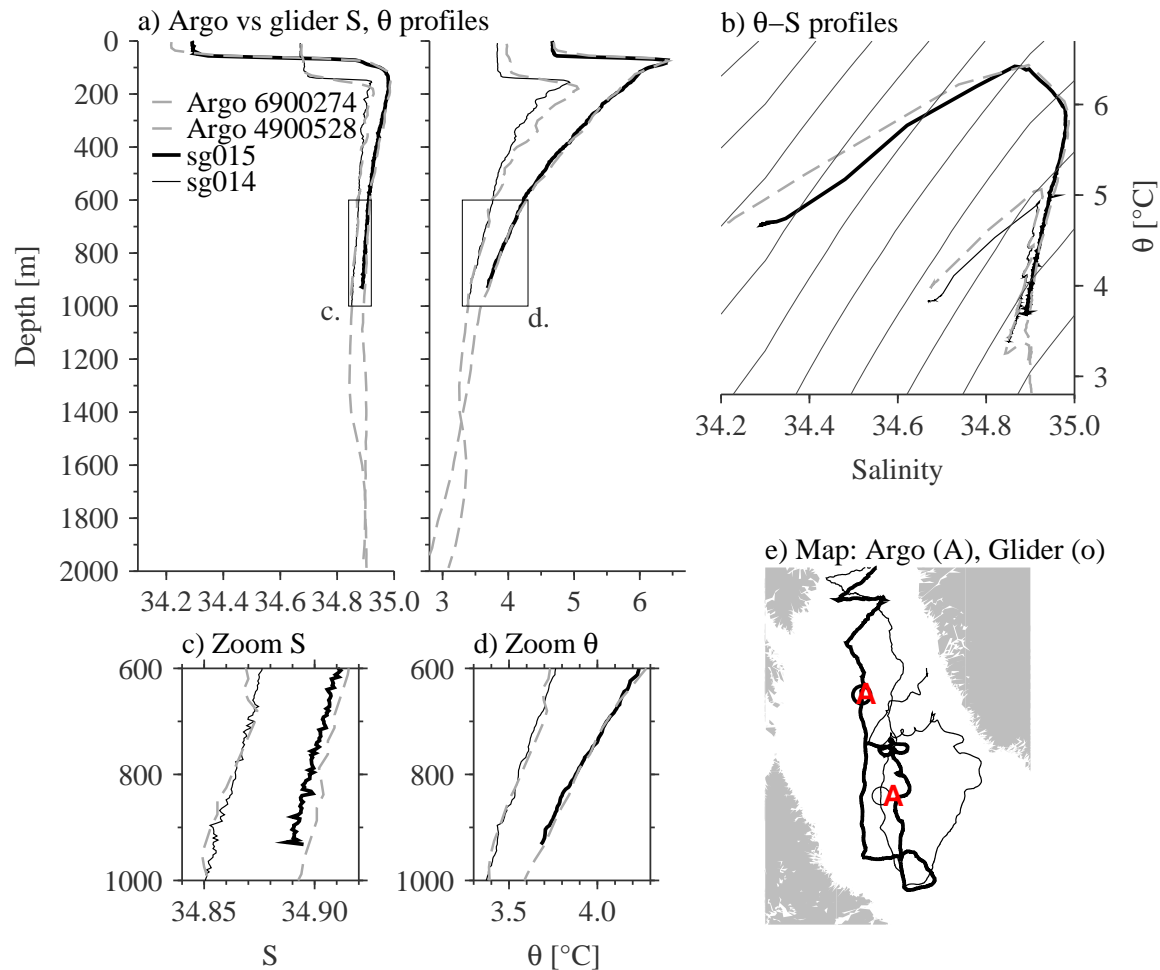


Figure 5.2: Comparison between selected Argo and Seagliders hydrographic profiles. The whole 1000 m Seaglider and 2000 m Argo profiles as a function of depth are in (a), the same data plotted in $\theta - S$ is in (b) contoured every 0.01 kg m^{-3} , detailed salinity and temperature plots are in (c) and (d), and the map showing the profile locations is in (e). The chosen profiles are the 2 pairs nearest in time for sg015 and sg014: Argo 6900274 (62.87°N , 57.69°W , November 14, 2004) and sg015 cycle 260 (62.83°N , 58.04°W , November 17, 2004) and Argo 4900528 (59.05°N , 55.58°W , December 17, 2004) and sg014, cycle 307 (59.03°N , 56.55°W , December 19, 2004). In the detail salinity plot (c) of the profiles between 600-1000 m, a uniform offset between sg015 and Argo salinities shows the Seaglider registering salinities fresher by 0.01, while temperatures were within 0.05°C .

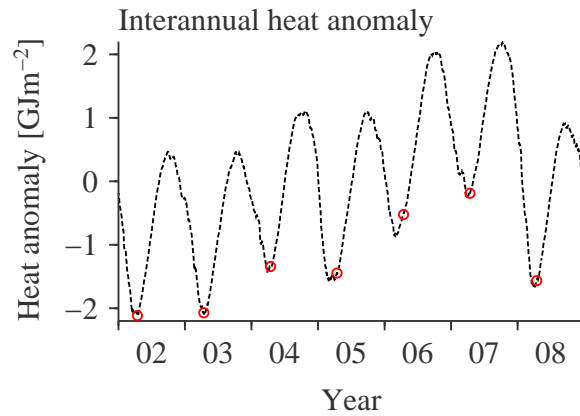


Figure 5.3: Cumulative heat content from time-integrated NCEP heat fluxes (latent, sensible, net shortwave and longwave). Cumulative anomaly in April is circled. The increasing trend from 2002-2007 is indicative of gaining heat (restratifying) until 2008 when cooling was particularly intense.

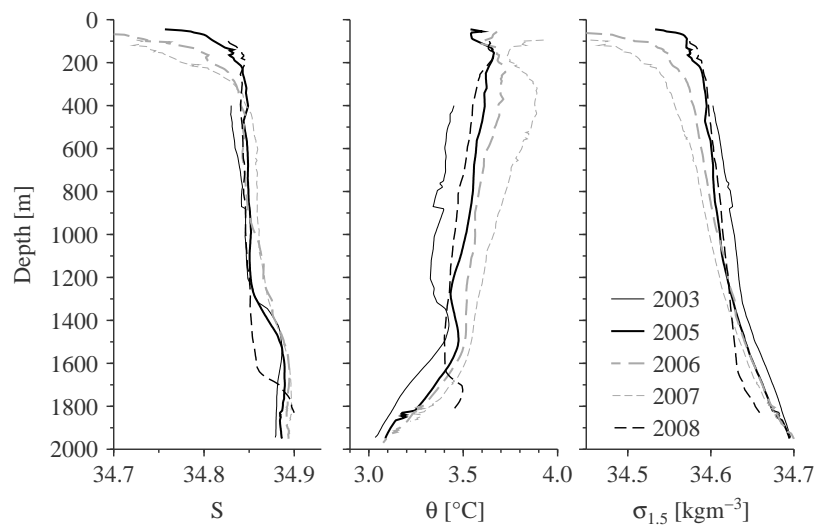


Figure 5.4: Evolution of LSW over the 2003-2008 years, as shown by density class per year. No profiles were available in 2004. Regions near the surface, especially for 2003, lack some points due to the conversion to σ coordinates. Profiles are only shown over depth regions that were created using at least the median number of points per sigma level.

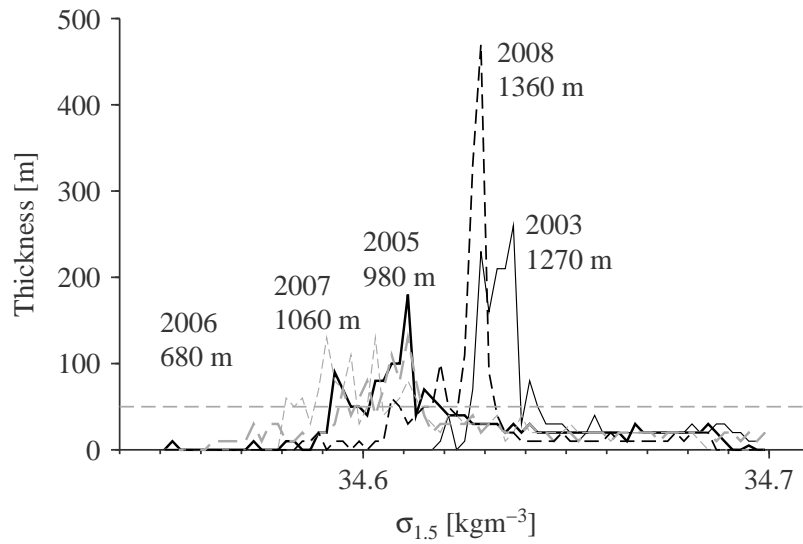


Figure 5.5: Distribution of $\sigma_{1.5}$ thickness after Lazier et al. (2002, Fig. 5): Thickness of layers between $\sigma_{1.5}$ intervals of 0.002 kgm^{-2} in the convection region of $56\text{-}58^\circ\text{N}$ and $53\text{-}55^\circ\text{W}$ for April; legend as in Fig. 5.4. This plot quantifies what is visible in the mean profiles of Fig. 5.4, that the 2008 convective winter had the deepest mixed layers (thickest pycnostad) in several years, while the 2003 and 2005 years were still near 1000 m.

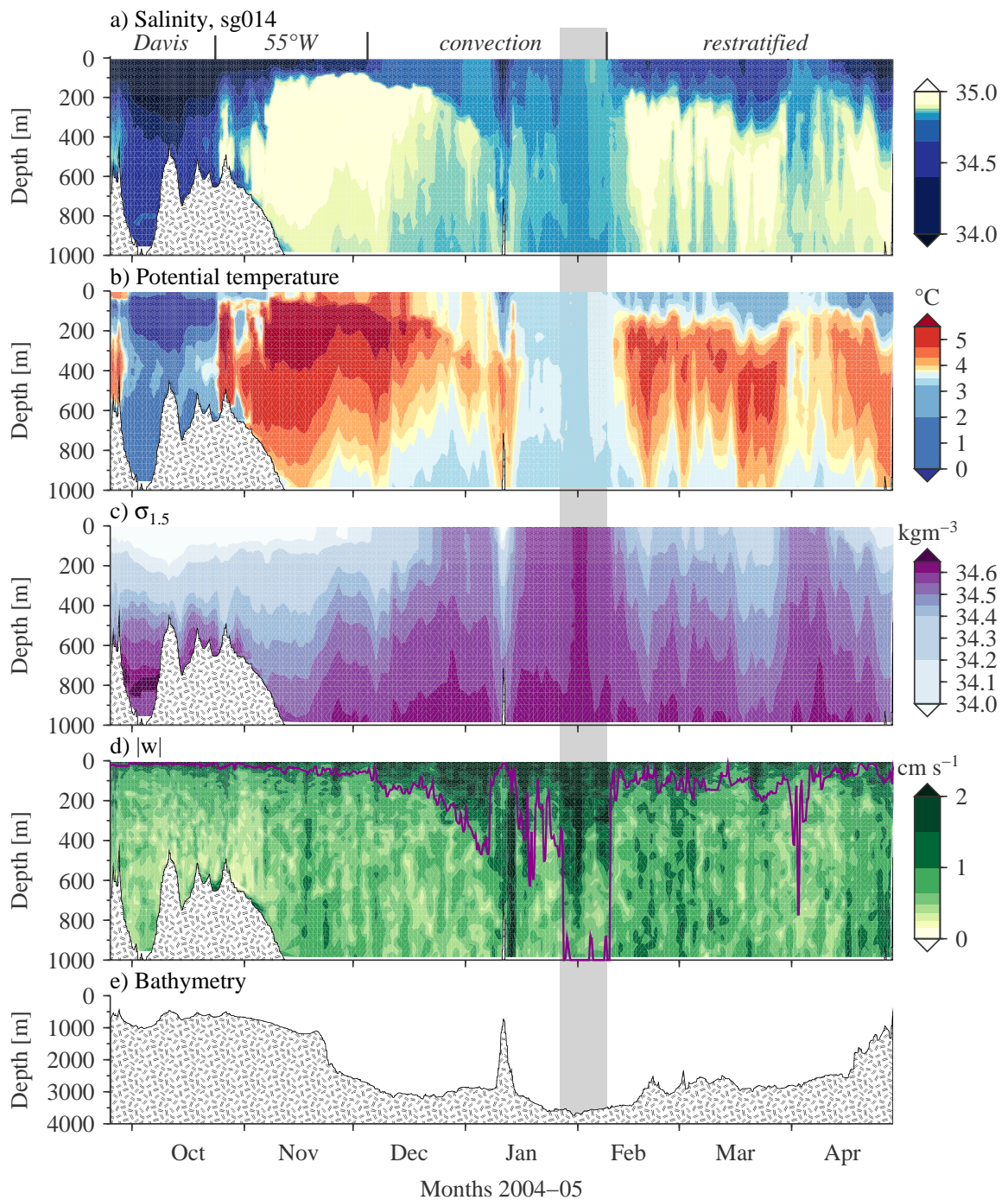


Figure 5.6: Salinity (a), potential temperature (b) and potential density ($\sigma_{1.5}$, c), vertical speed $|w|$ (d), and water depth (e) observed by sg014. The regions labeled above (a) correspond roughly to the colored regions in the map in Fig. 5.1a: Davis and restratified correspond directly, while the section marked 55°W is unmarked in Fig. 5.1a, and the red-highlighted sections maps only the region with 1000 m mixed layers here. Profiles from the section highlighted in light gray appear in Fig. 5.10.

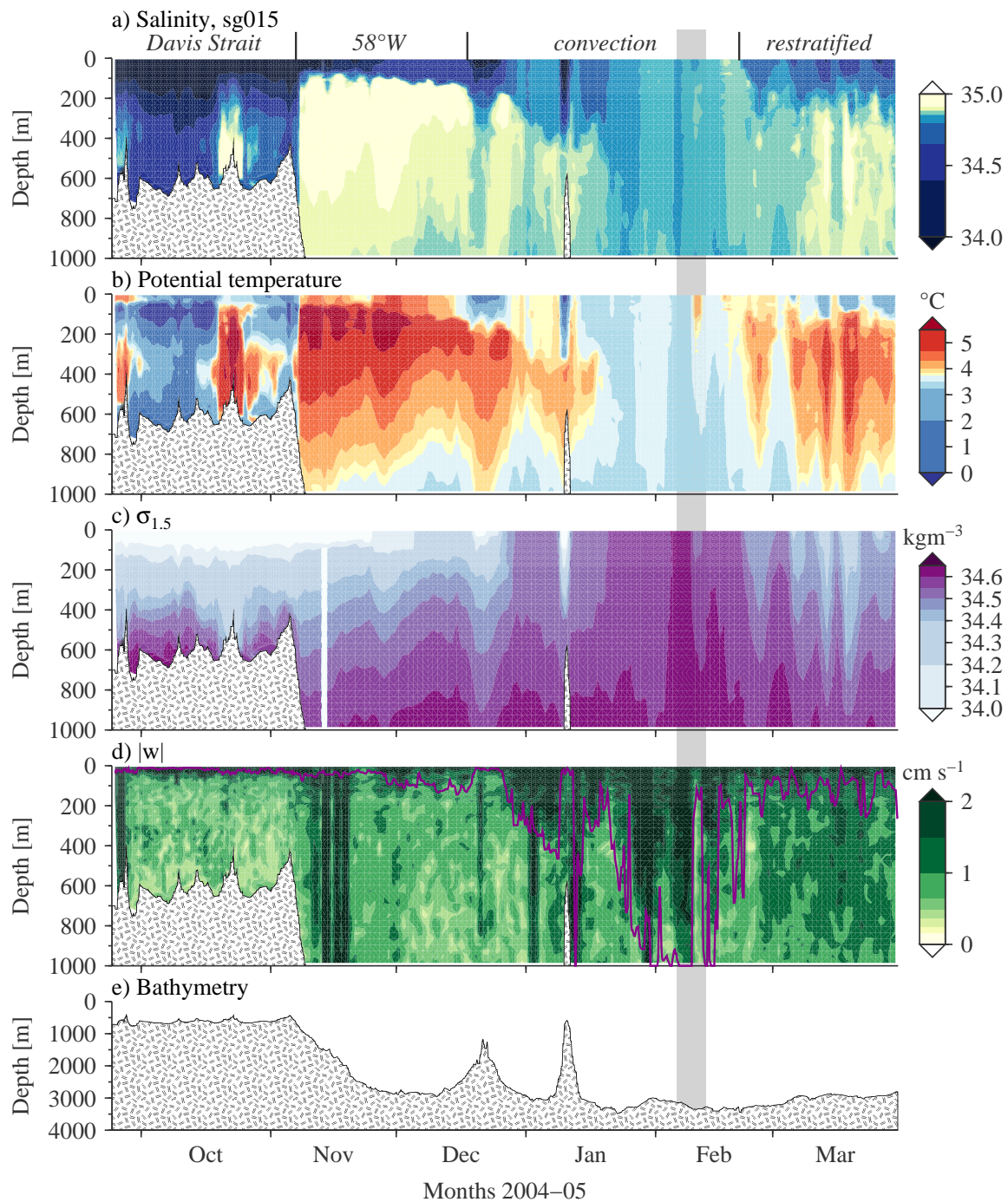


Figure 5.7: Salinity (a), potential temperature (b) and potential density ($\sigma_{1.5}$, c), vertical speed $|w|$ (d), and water depth (e) observed by sg015. The regions labeled above (a) correspond roughly to the colored regions in the map in Fig. 5.1a, as for Fig. 5.6. Profiles from the section highlighted in light gray appear in Fig. 5.9.

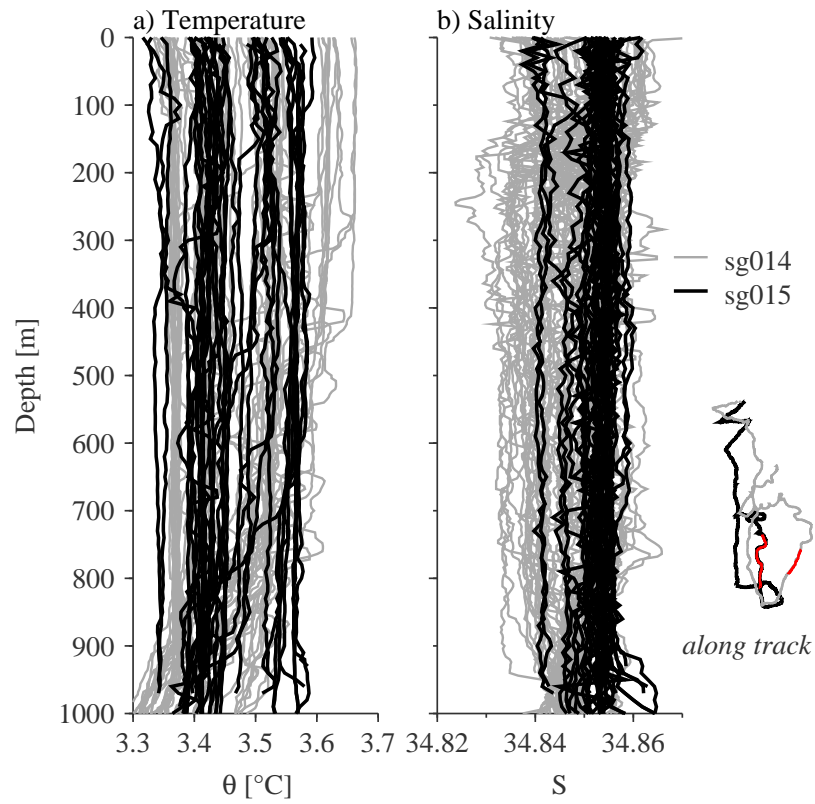


Figure 5.8: Potential temperature (a) and salinity (b) profiles during deepest mixed layers observed by sg015 (black) and sg014 (gray), at the locations specified on Seaglider tracks in the inset. Sg015 profiles are from the black solid line (January 30-February 14, 2005) while sg014 profiles are along the gray solid line (January 12-25, 2005).

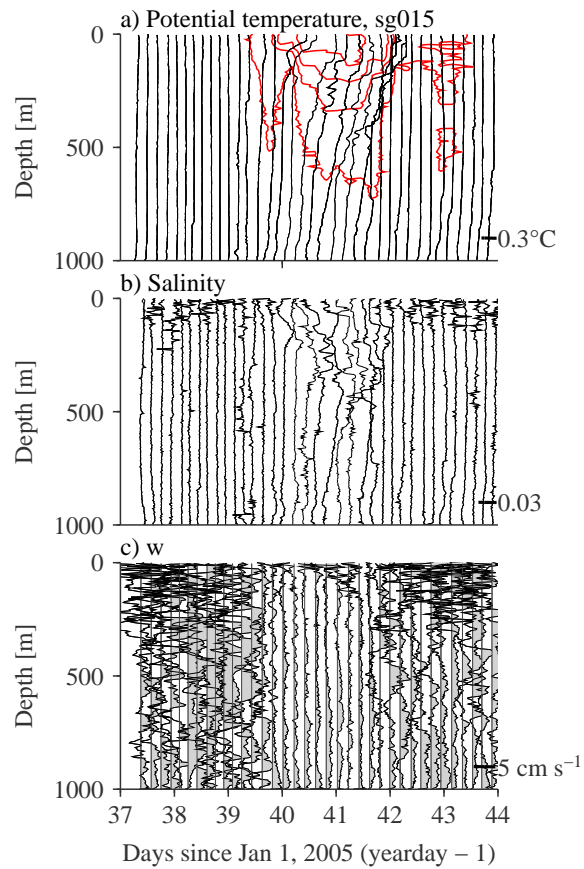


Figure 5.9: Waterfall plot of (a) potential temperature, (b) salinity, and (c) vertical velocity during active convection in the Labrador Sea. In (a), $\sigma_{1.5}$ is contoured at 0.02 kg m^{-3} . The region shown corresponds to the gray shaded region in Fig. 5.7.

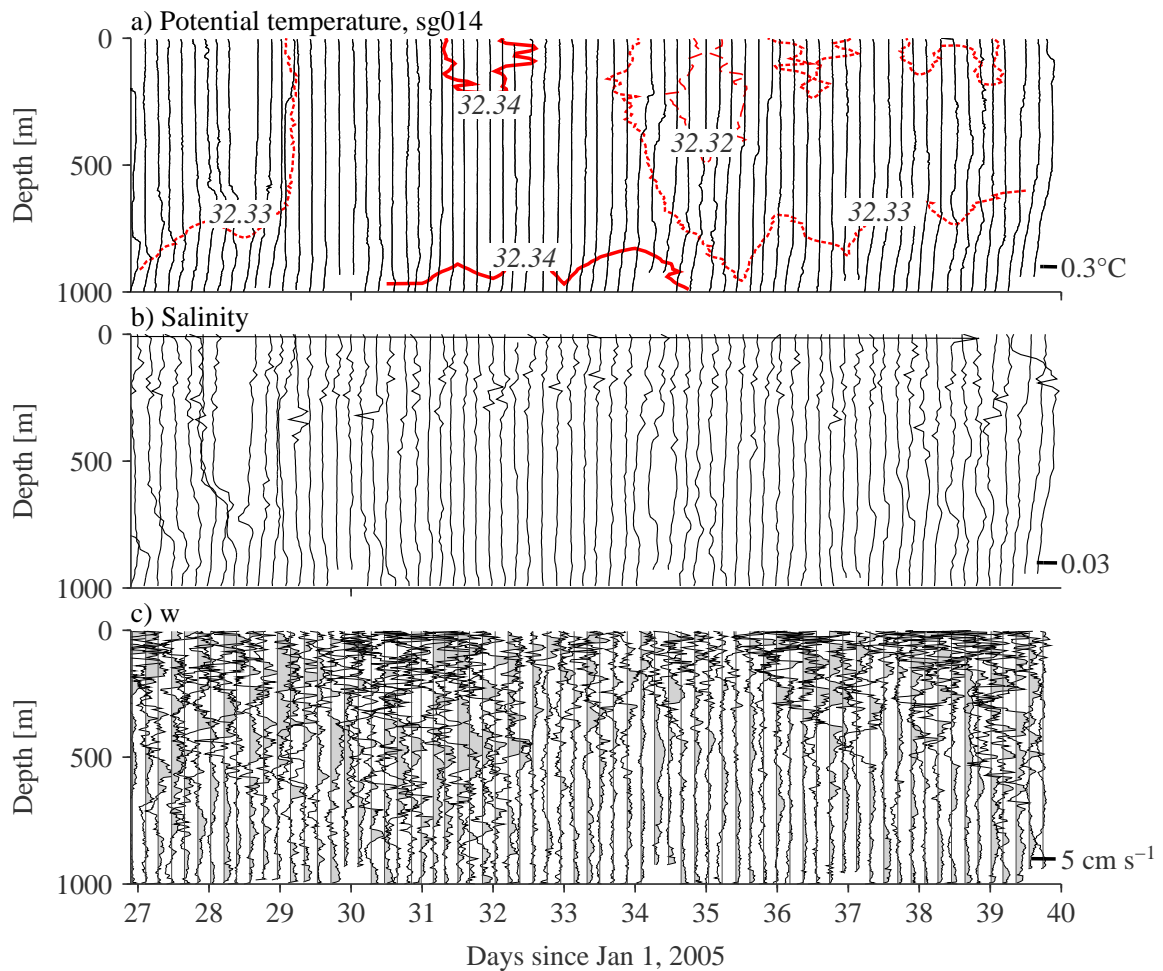


Figure 5.10: Waterfall plot of (a) potential temperature, (b) salinity, and (c) vertical velocity during deepest mixed layers observed by sg014 in the Labrador Sea. The region shown here corresponds to the gray shaded region in Fig. 5.6. In panel (a), the red contours correspond to potential density contours at 0.01 kgm^{-3} spacing.

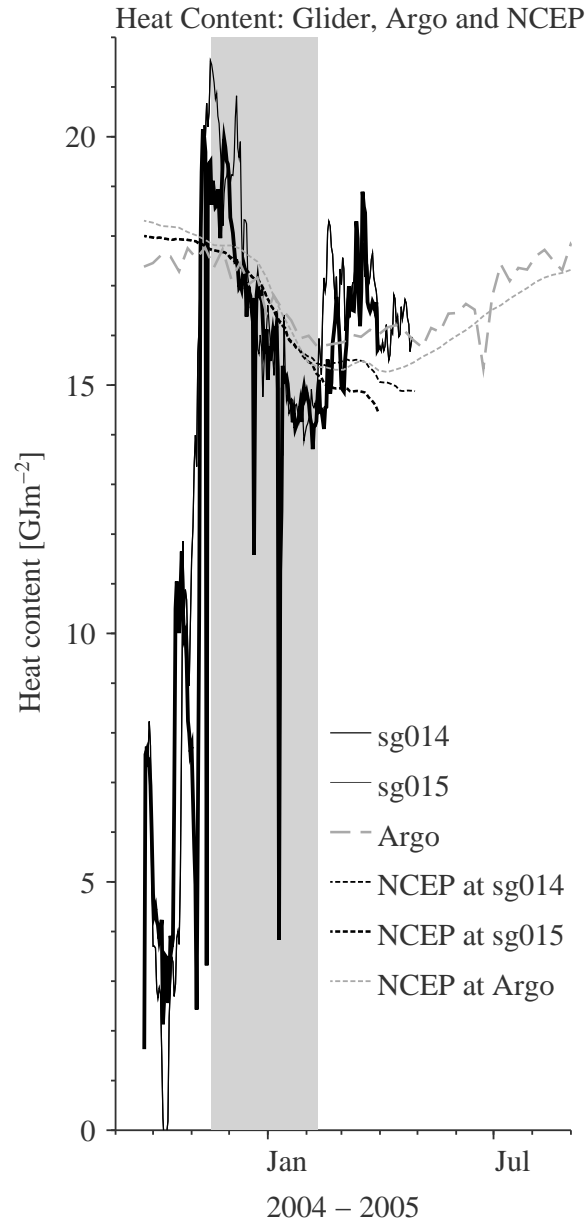


Figure 5.11: Heat content from sg014, sg015, Argo float 4900611 (in the convection region for the duration) and NCEP reanalysis. Heat flux is slope of the linear fit to the heat content within the shaded region (November 11, 2004-February 10, 2005): for sg014, -985 W m^{-2} , for sg015, -700 W m^{-2} and for Argo and NCEP, approximately -240 to -280 W m^{-2} . Wintertime heat fluxes from Seaglider, which have significant translational motion, are much greater than those predicted by the NCEP fluxes.

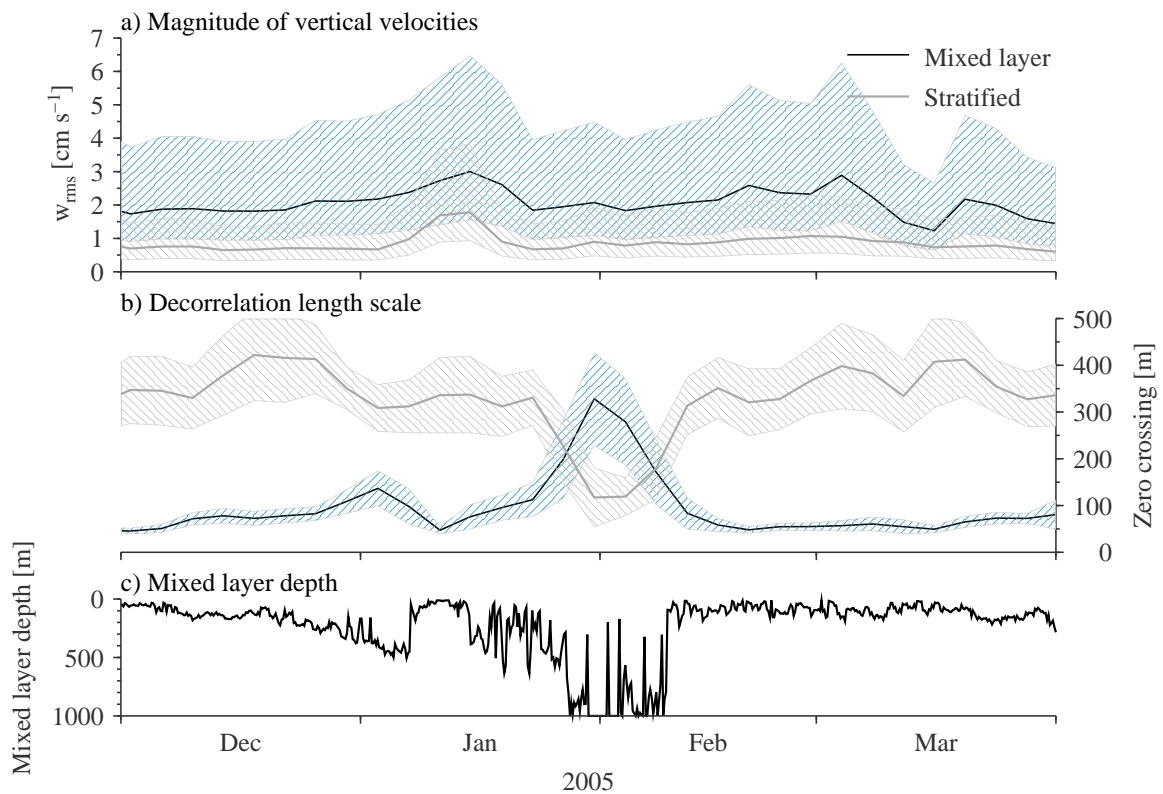


Figure 5.12: Rms-vertical speeds (a), decorrelation length scales (b) and mixed layer depths (c) for sg014, below the mixed layer (black) and within the mixed layer (gray). Speeds and length scales are averaged over 8 days, approximately 24 dive cycles. Shading indicates 95% confidence intervals. Sg014 was on the Labrador Shelf around January 10, as shown by the shallow mixed layer depths. Deep convection with mixed layers > 1000 m were sampled at the end of January and beginning of February, 2005.

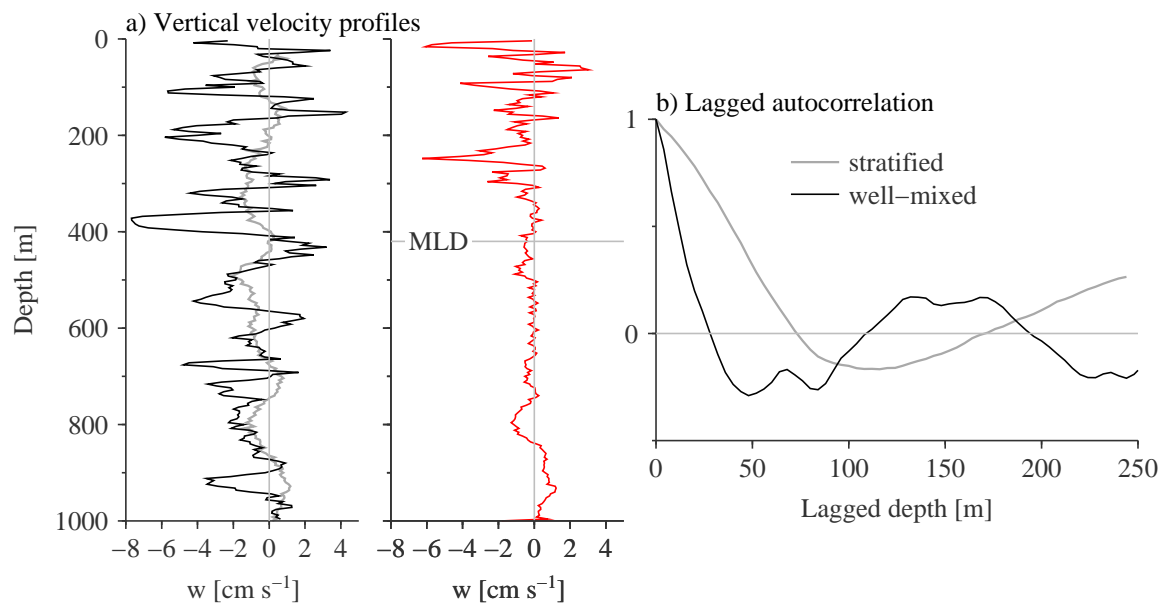


Figure 5.13: Spatial scales in vertical velocity from stratified and convecting regions, sg014. The gray line in panel (a) is w from dive cycle 284 in the stratified region while the black line is dive cycle 482 in a 1000 m deep mixed layer. The red line is for dive cycle 347 with mixed layer depth of 421 m, and (b) shows lagged autocorrelations for the fully stratified and fully unstratified profiles. Though Seaglider does not make vertical profiles but rather travels at a 1:3 slope on average, the stratified profile of w appears to have a consistent wavenumber like an internal wave while the unstratified w has downward peaks, higher amplitudes and shorter scales. Zero crossings are approximately $1/\pi$ times the equivalent wavelength.

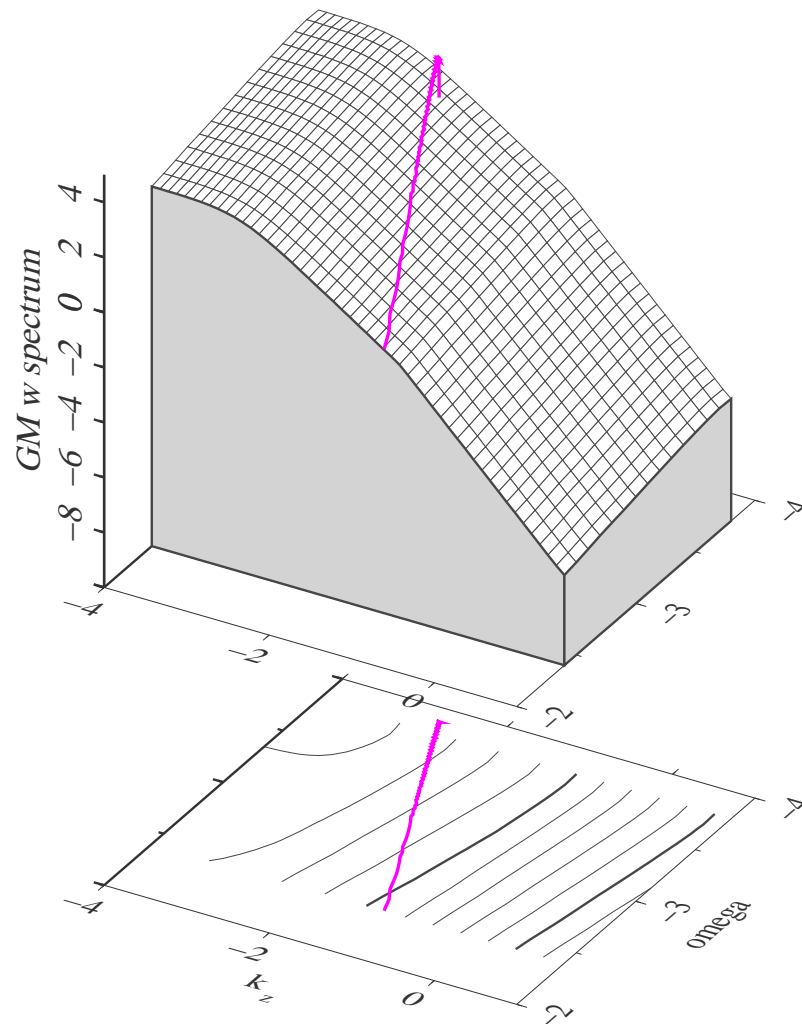


Figure 5.14: Canonical GM76 vertical velocity spectrum in wavenumber-frequency space. The wave phase speed (ω/k_z) corresponding to the typical glider vertical speed of 0.06 cm s^{-1} is plotted in magenta.

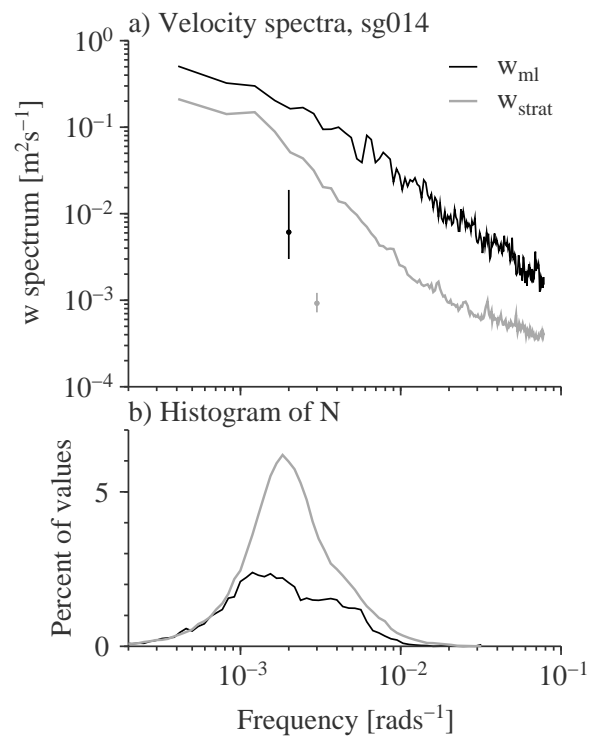


Figure 5.15: a) Vertical velocity spectra from sg014. 95% confidence intervals were calculated using the number of independent days of sampling as the degrees of freedom, 10 for the mixed layer and 115 for the stratified spectra. The histogram of buoyancy frequency values (N) is shown in (b), indicating the approximate location of expected breaks in the spectra. For frequencies $< N$, internal waves may dominate with a white spectrum, while for frequencies above N , a turbulent regime is expected (slope $-5/3$).

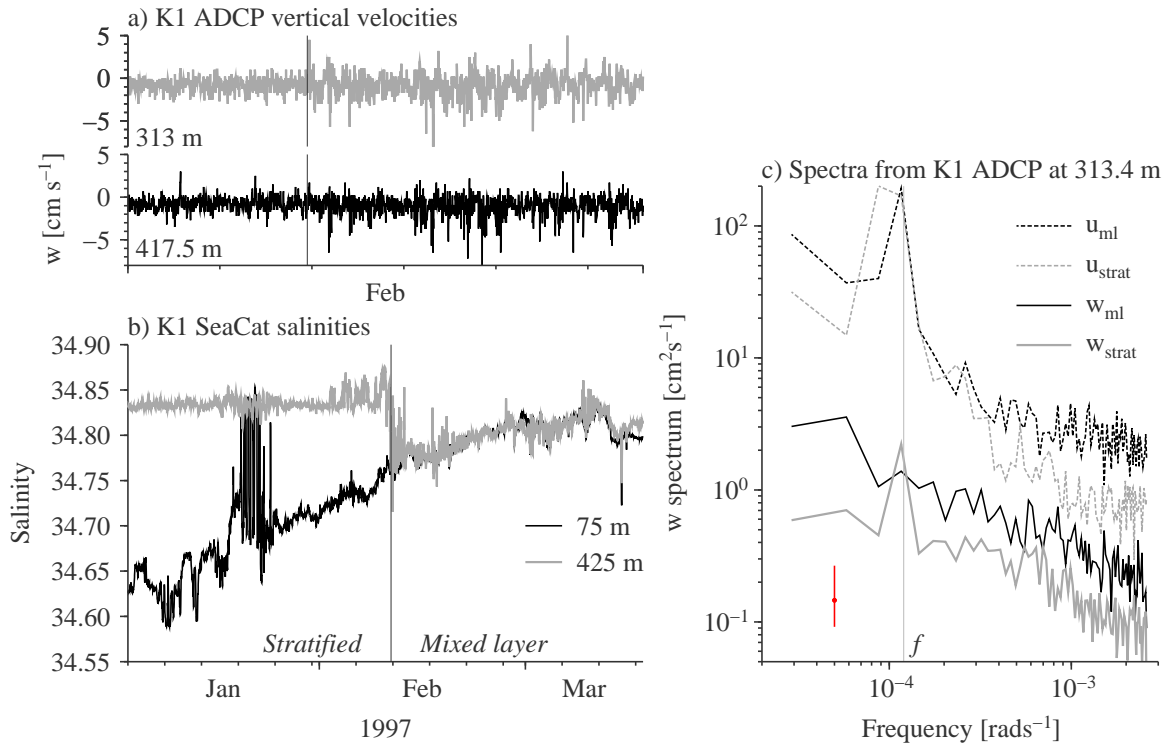


Figure 5.16: Vertical velocity time series for the month of February (a), salinity time series from January through March (b) and velocity spectra (c) from the K1 mooring, 1996-97 convective winter. Salinities from 75 m and 425 m SeaCats are shown. When the two measurements agree, the mixed layer is at least 425 m deep. Velocity spectra were calculated from the upward looking ADCP at the 313.4 m depth bin. Stratified spectra are for the time period before February 10, while mixed layer are for after February 10. Time series were broken into 14 segments before calculating spectra then averaging to produce the spectra shown. The red bar is the 95% confidence interval for all 4 spectra. The vertical gray line in (c) indicates the Coriolis parameter (f).

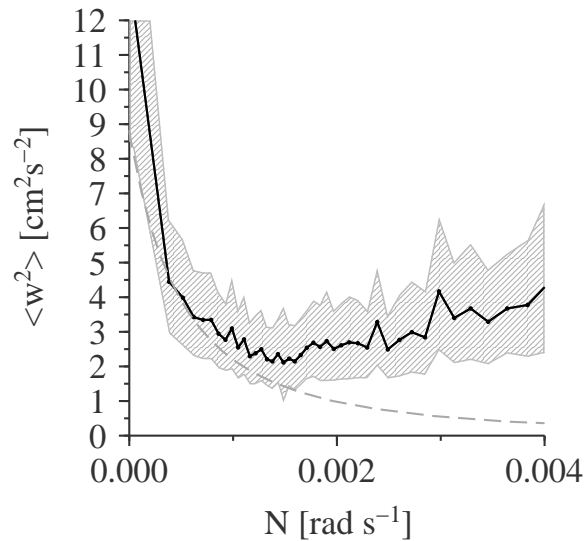


Figure 5.17: WKB-scaling of w_{rms} in the stratified ocean, sg015. Vertical velocity measurements were binned by N . For $N < 0.0013 \text{ rad s}^{-1}$, measurements matched theoretical expectations for a GM-internal wave field, scaling as $\langle w^2 \rangle \approx 0.25 N_0 / N$. The WKB-scaling breaks for $N > 0.0013 \text{ rad s}^{-1}$.

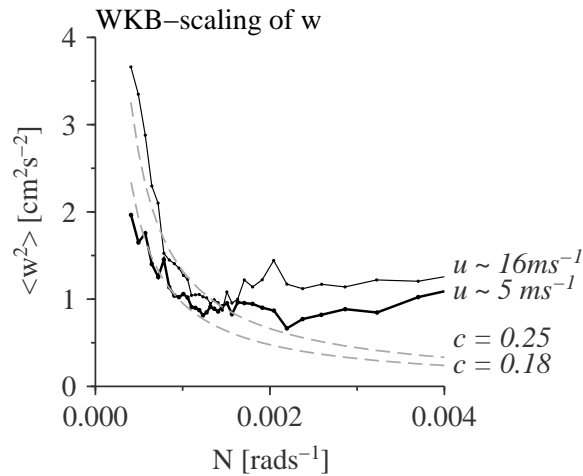


Figure 5.18: WKB-scaling of w_{rms} in the stratified ocean, sg015. Vertical velocity measurements were binned by N and wind speed (either $> 10 \text{ m s}^{-1}$ or $< 10 \text{ m s}^{-1}$). Winds in these two bands averaged 5 and 16 m s^{-1} . For $N < 0.0013 \text{ rad s}^{-1}$, measurements matched theoretical expectations for a GM-internal wave field, scaling as $\langle w^2 \rangle \approx 0.25 N_0 / N$. The WKB-scaling breaks for $N > 0.0013 \text{ rad s}^{-1}$. A weak dependence of the coefficient c_{GM} on winds was found, though 95% confidence intervals overlap. $c_{GM} \approx 0.18$ for weaker winds and 0.25 for higher winds.

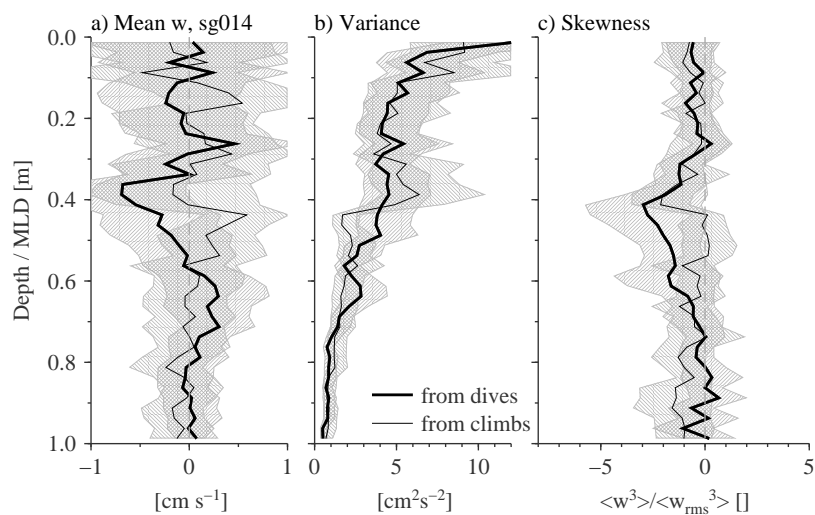


Figure 5.19: Mean profiles of vertical velocity (a), variance (b) and skewness (c) in scaled depth coordinates ($z / \text{mixed layer depth}$) from sg014 for profiles with mixed layer depth ≥ 300 m. The surface is at 0 and mixed layer depth at 1. Vertical velocities have a near zero mean. Variance levels increase near the surface, and skewness is somewhat negative.

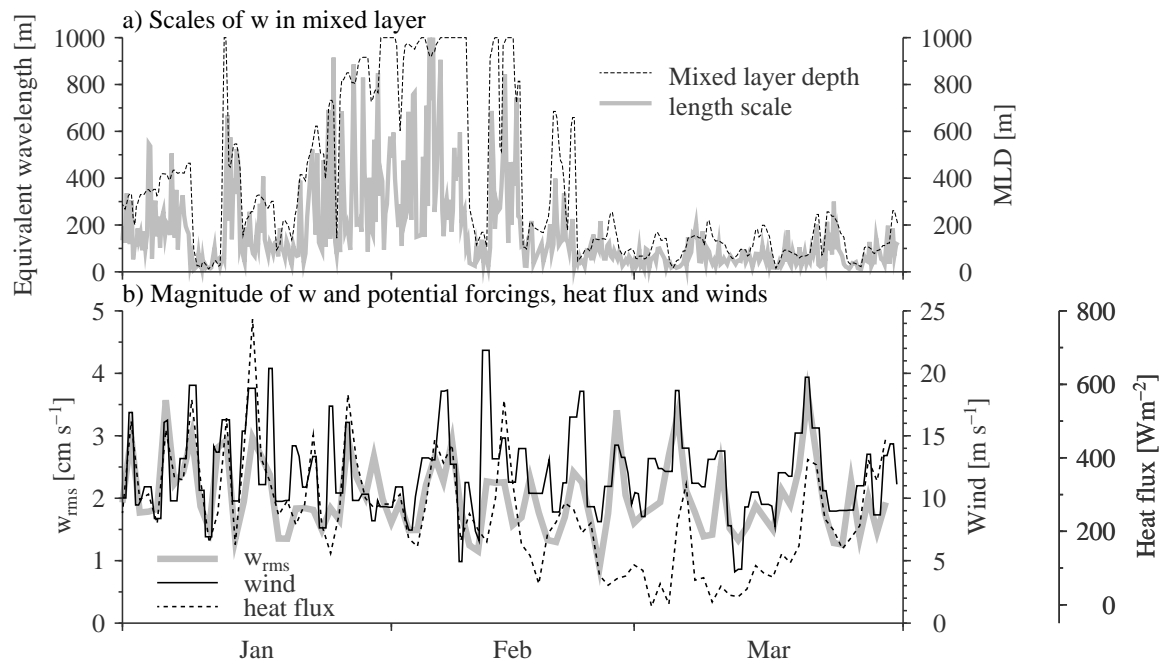


Figure 5.20: Scales and magnitude of vertical velocities in the surface mixed layer from sg015, January through March, 2005. a) Decorrelation length scale of vertical velocities in the mixed layer and the mixed layer depth. Notably, the length scales appear to correlate with mixed layer depths, with a ratio of about $L = 0.27MLD$. b) Magnitude of vertical velocities in the surface mixed layer estimated as w_{rms} in 1-daily periods corresponding to the daily period of the heat fluxes and winds from Yu and Weller 2007. Wind speeds and heat fluxes are also shown.

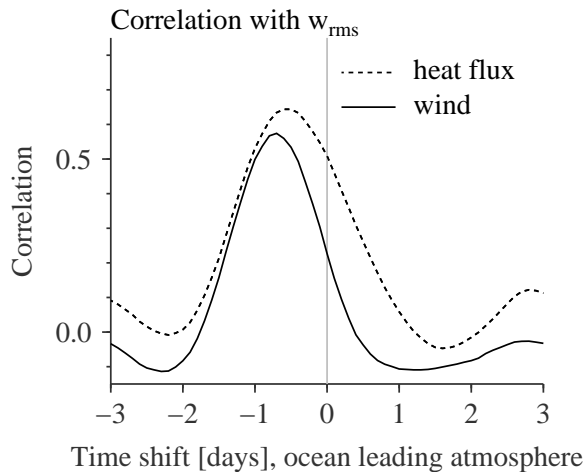


Figure 5.21: Lag correlation between w_{rms} and heat flux (dotted line) and winds (solid line) for sg015, January 1-February 20, 2005 (51 days). Peaks were found for a lag of about 0.6 days (heat flux) and 0.7 days (winds). Correlation coefficients are above 0.5.

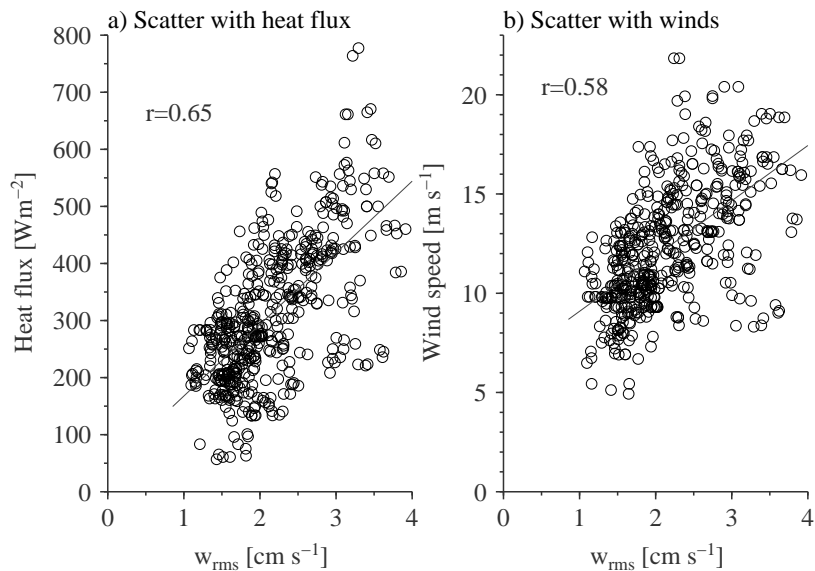


Figure 5.22: Scatterplots of sg015 w_{rms} on heat flux (a) and wind speed (b) for time series lagged by 0.6 days (a) and 0.7 days (b).

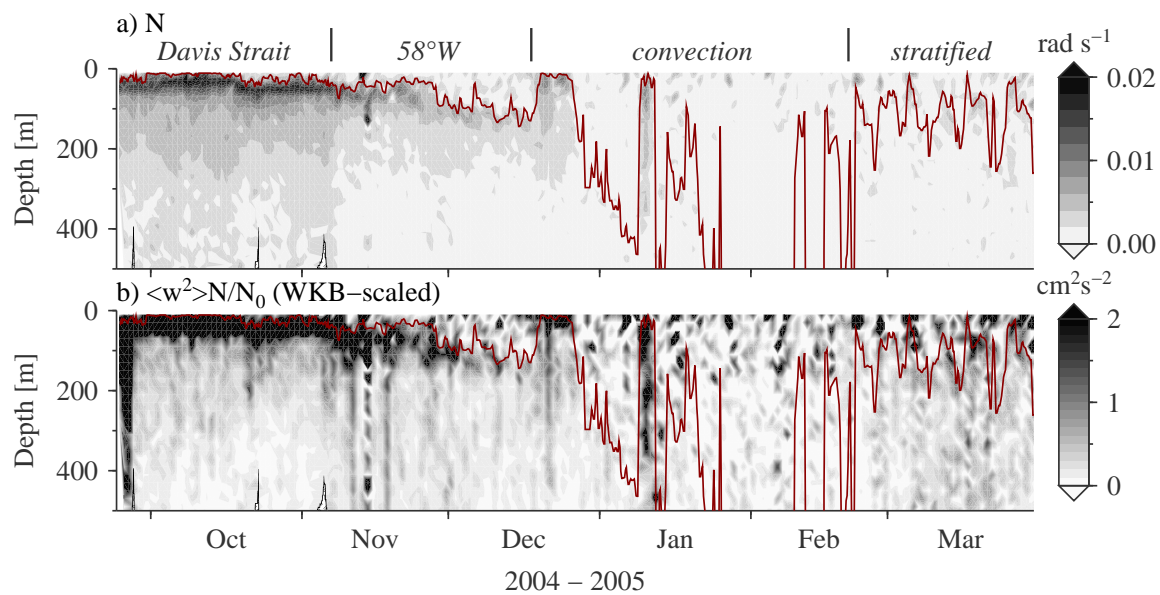


Figure 5.23: Buoyancy frequency (a), WKB-scaled vertical velocities (b) and wind speed (c) for the entire mission, top 500 m, sg015.

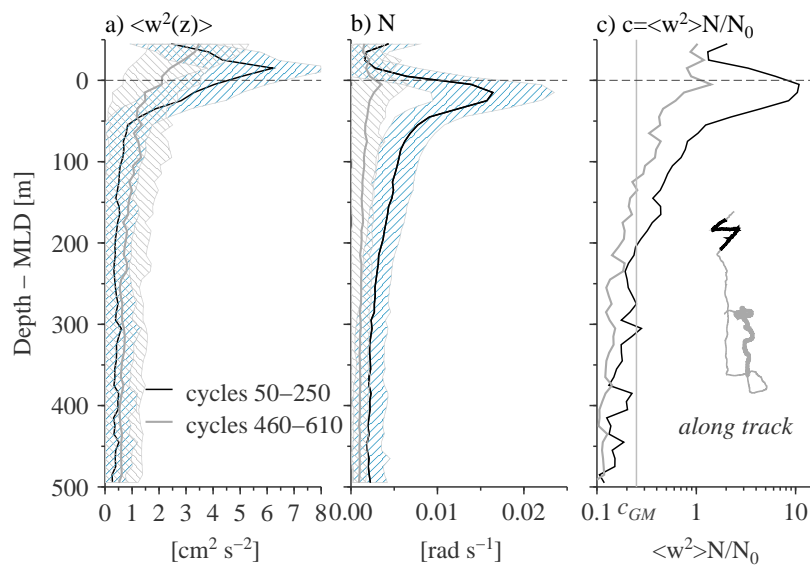


Figure 5.24: Average profiles of vertical velocity variance (a) and buoyancy frequency (b) which have been shifted vertically to align by mixed layer depth. Shaded regions indicate ± 1 standard deviation, calculated over 150 dive cycles, sg015 cycles 50-200. Panel (c) is the average coefficient, $c = \langle w^2 \rangle N / N_0$ where N_0 is the canonical pycnocline stratification for the GM model of internal waves.

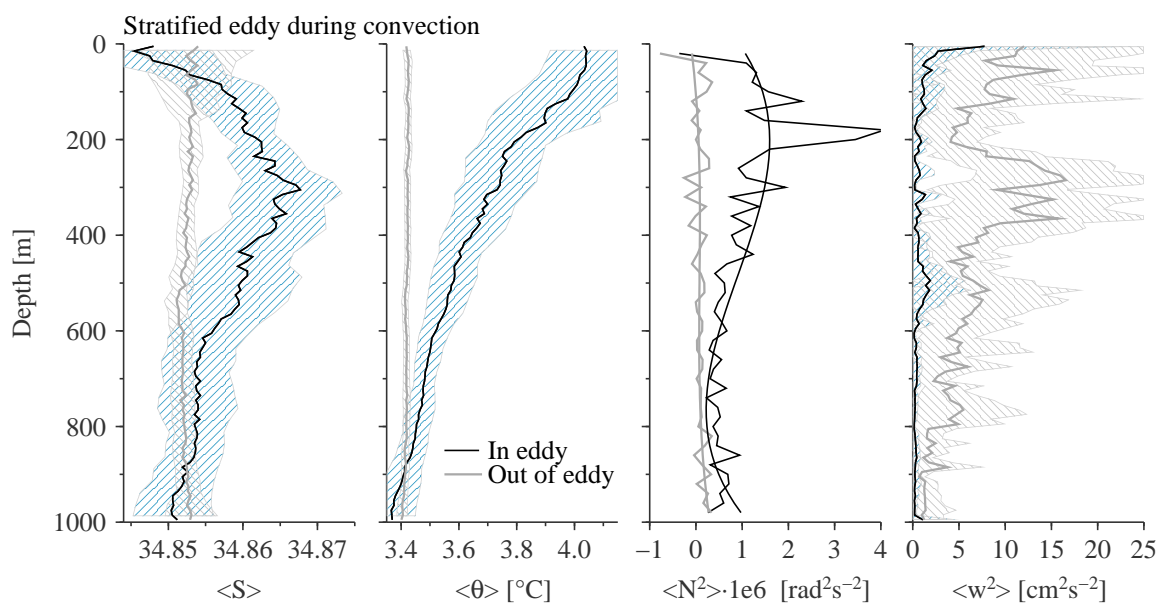


Figure 5.25: Average profiles of (a) salinity, (b) potential temperature, (c) N^2 and (d) vertical velocity during active convection in the Labrador Sea (gray) and inside the Irminger Ring (black), sg015.

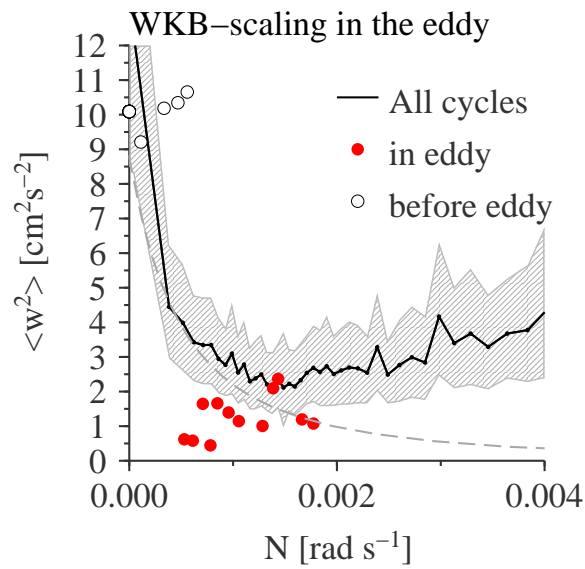


Figure 5.26: Comparing energy levels in the eddy (red) with the entire record (black line) and convective period immediately preceding the eddy (open circles). The GM model expectations (5.9) with $c_{GM} = 0.25$ are given by the thin black line. For the highly stratified region of the eddy, in the top 300 m, the vertical velocity variance is below GM, even though observations elsewhere in the record have vertical velocity variance in the highly stratified regions above the GM model.

Chapter 6

CONCLUSIONS

The Labrador Sea is a site of intense primary productivity, fueling the food web for the primarily fisheries-driven economies in the region. Seaglider data described a high resolution section through the spring and summer blooms of 2005, highlighting the importance of freshwater to enhance the early north bloom (north of 60°N). SeaWiFS satellite chlorophyll images confirmed the region as having some of the highest annual chlorophyll levels, and combined with climatologies we were able to show that surface freshwater was the primary driver of bloom timing in the region. This contrasted with the central Labrador Sea bloom which occurred later in the summer, after deep convection had ended.

Deep convection in the Labrador Sea was observed by two gliders, numbered 14 and 15, in the winter of 2004-05. These gliders transected the Labrador Sea from north-to-south in parallel, along 55 and 58°W, cutting through the distinct Arctic watermasses in the Davis Strait, and across the extension of the West Greenland Current at the 1000-3000 m isobaths in the Labrador Sea.

A new product, vertical velocities from Seagliders was used to diagnose the geography of vertical velocities in the stratified and unstratified regions in the Labrador Sea, as well as two transition regions between stratified and unstratified. In the stratified Labrador Sea, we found that rms-vertical velocities scaled with the inverse of N , in accordance with WKB scaling. Additionally, there was a slight dependence on wind so that periods with higher wind levels had a higher energy level for the same stratification than periods with lower wind levels. In the unstratified ocean, particularly during deep convection where mixed layer depths exceeded the 1000 m profile depth of Seaglider, rms-velocities were found to scale well with buoyancy and wind forcing, with r^2 values of 0.45-0.55. Decorrelation length scales in the mixed layer also scaled with mixed layer depth.

Two interesting transition regions were observed, one in the transition zone just below the surface mixed layer and the other between a stratified eddy which was surrounded by deep convection to 1000 m. In the transition zone, rms-vertical velocities were elevated above background GM lev-

els, consistent with wave trapping in the high stratification or possibly resulting from interfacial wave energy at a sharp pycnocline. In the stratified eddy, rms-vertical velocities were lower than the background GM levels, in striking contrast with vertical velocities in the surrounding deep mixed layers.

While space-time aliasing of the Seaglider posed a challenge—the 20 cm s^{-1} translational speed, 1:3 glide slope angle, and inclusion of data spanning over a thousand kilometers and 6 months—unraveling the two was aided with 2-d satellite data for relatively synoptic measurements, Argo profiles for better spatial coverage but including depth-information, and when neither were available or adequate, climatology. The space-time difficulty was highlighted by heat flux estimates from Seaglider heat content, which were significantly affected by contributions from the $u_g \cdot \nabla H$ term, yielding heat flux estimates several times that of NCEP/NCAR reanalysis heat flux estimates. High resolution observations were crucial for detailed biological structures in thin layers on the Labrador shelf, fresh eddies in the northern region, and at the Labrador shelf-break front. Multiple profiles of hydrography within the convecting regions showed that horizontal variability of watermasses during deep convection is relatively large, spanning 0.03 kg m^{-3} , equivalent to the vertical stratification from 100 to 1000 m that exists immediately following restratification.

Seaglider is a powerful tool for observing remote processes, like deep convection, when ship-board observations are expensive. The addition of vertical velocities was particularly fruitful for observing deep convection since velocities are much higher than elsewhere in the ocean, and relevant dynamics can be described in terms of vertical velocities.

BIBLIOGRAPHY

- Abbott, M. R. and Letelier, R. M. (1998). Decorrelation scales of chlorophyll as observed from bio-optical drifters in the California Current. *Deep Sea Research II*, 45:1639–1667.
- Aldredge, A. L., Cowles, T. J., MacIntyre, S., Rines, J. E. B., Donaghay, P. L., Greenlaw, C. F., Holliday, D. V., Dekshenieks, M. M., Sullivan, J. M., and Zaneveld, J. R. V. (2002). Occurrence and mechanisms of formation of a dramatic thin layer of marine snow in a shallow Pacific fjord. *Marine Ecology Progress Series*, 233:1–12.
- Allen, J. T., Brown, L., Sanders, R., Moore, C. M., Mustard, A., Fielding, S., Lucas, M., Rixen, M., Savidge, G., Henson, S., and Mayor, D. (2005). Diatom carbon export enhanced by silicate upwelling in the northeast Atlantic. *Letters to Nature*, 437:728–732.
- Avsic, T., Karstensen, J., Send, U., and Fischer, J. (2006). Interannual variability of newly formed Labrador Sea Water from 1994 to 2005. *Geophysical Research Letters*, 33.
- Bailey, D. A., Rhines, P. B., and Hakkinen, S. (2005). Formation and pathways of North Atlantic Deep Water in a coupled ice-ocean model of the Arctic-North Atlantic Oceans. *Journal of Climate*, 25:497–516.
- Behrenfeld, M. J. and Boss, E. (2003). The beam attenuation to chlorophyll ratio: an optical index of phytoplankton physiology in the surface ocean? *Deep Sea Research I*, 50:1537–1549.
- Birch, D. A., Young, W. R., and Franks, P. J. S. (2008). Thin layers of plankton: Formation by shear and death by diffusion. *Deep Sea Research I*, 55:277–295.
- Boss, E., Swift, D., Taylor, L., Brickley, P., Zaneveld, J. R. V., Riser, S., and Perry, M. J. (2008). Robotic *in situ* and satellite-based observations of pigment and particle distributions in the western North Atlantic. *Limnology and Oceanography*.
- Chapman, D. C. and Lentz, S. J. (1994). Trapping of a coastal density front by the bottom boundary layer. *Journal of Physical Oceanography*, 24:1464–1479.

- Coates, M. J., Ivey, G. N., and Taylor, J. R. (1995). Unsteady, turbulent convection into a rotating, linearly stratified fluid: Modeling deep ocean convection. *Journal of Physical Oceanography*, 25:3032–3050.
- Conover, R. J., Wilson, S., Harding, G. C. H., and Vass, W. P. (1995). Climate, copepods and cod: some thoughts on the long-range prospects for a sustainable northern cod fishery. *Climate Research*, 5:69–82.
- Cota, G. F., Harrison, W. G., Platt, T., Sathyendranath, S., and Stuart, V. (2003). Bio-optical properties of the Labrador Sea. *Journal of Geophysical Research*, 108(C7).
- Cullen, J. J. (1982). The deep chlorophyll maximum: Comparing vertical profiles of chlorophyll *a*. *Can. J. Fish. Aquat. Sci.*, 39:791–803.
- Cuny, J., Rhines, P. B., Niiler, P. P., and Bacon, S. (2002). Labrador Sea boundary currents and the fate of the Irminger Sea Water. *Journal of Physical Oceanography*, 32:627–635.
- Dekshenieks, M. M., Donaghay, P. L., Sullivan, J. M., Rines, J. E. B., Osborn, T. R., and Twardowski, M. S. (2001). Temporal and spatial occurrence of thin phytoplankton layers in relation to physical processes. *Marine Ecology Progress Series*, 223:61–71.
- Denman, K. L. and Abbott, M. R. (1994). Time scales of pattern evolution from cross-spectrum analysis of advanced very high resolution radiometer and coastal zone color scanner imagery. *Journal of Geophysical Research*, 99(C4):7433–7442.
- Desaubies, Y. and Gregg, M. C. (1981). Reversible and irreversible finestructure. *Journal of Physical Oceanography*, 11:541–556.
- Devred, E., Sathyendranath, S., and Platt, T. (2007). Delineation of ecological provinces using ocean colour radiometry. *Marine Ecology Progress Series*, 346:1–13.
- Eriksen, C. C. (1978). Measurements and models of fine-structure, internal gravity-waves, and wave breaking in deep ocean. *Journal of Geophysical Research*, 83:2989–3009.

- Eriksen, C. C., Osse, T. J., Light, R. D., Wen, T., Lehman, T. W., Sabin, P. L., Ballard, J. W., and Chiodi, A. M. (2001). Seaglider: a long-range autonomous underwater vehicle for oceanographic research. *IEEE Journal of Oceanic Engineering*, 26:424–436.
- Eriksen, C. C. and Rhines, P. (2008). Convective- to gyrescale-dynamics, the first Seaglider campaigns, 2003-2005. In Dickson, R. R., Meincke, J., and Rhines, P., editors, *Arctic-Subarctic Ocean Fluxes: Defining the Role of the Northern Seas in Climate*, pages 613–628. Springer.
- Feldman, G. C. and McClain, C. R. (2006). Ocean color web: SeaWiFs. In Kuring, N. and Bailey, S. W., editors, *NASA Goddard Space Flight Center*.
- Fennel, K. and Boss, E. (2003). Subsurface maxima of phytoplankton and chlorophyll: Steady-state solutions from a simple model. *Limnology and Oceanography*, 48:1521–1534.
- Fernando, H., Chen, R., and Boyer, D. (1991). Effects of rotation on convective turbulence. *Journal of Fluid Mechanics*, 228:513–546.
- Flierl, G. R. and Davis, C. S. (1993). Biological effects of Gulf Stream meandering. *Journal of Marine Research*, 51:529–560.
- Frajka-Williams, E. and Rhines, P. (2008). Offshore advection of freshwater and the Labrador Sea spring bloom from SeaWiFS, *submitted*. *Deep Sea Research I*.
- Frajka-Williams, E., Rhines, P., and Eriksen, C. (2009). Mesoscale variability in the Labrador Sea spring phytoplankton bloom observed by Seaglider. *Deep Sea Research I*.
- Franks, P. J. S. (1991). Thin layers of phytoplankton: a model of formation by near-inertial wave shear. *Deep Sea Research I*, 42(1):75–91.
- Franks, P. J. S. (1992). Sink or swim - accumulation of biomass at fronts. *Marine Ecology Progress Series*, 82:1–12.
- Garrett, C. J. R. and Munk, W. H. (1972). Space-time scales of internal waves. *Geophys. Fluid Dyn.*, 2:225–264.
- Garrett, C. J. R. and Munk, W. H. (1975). Space-time scales of internal waves: a progress report. *Journal of Geophysical Research*, 80:291–297.

- Garrett, C. J. R. and Munk, W. H. (1979). Internal waves in the ocean. *Annual Reviews in Fluid Mechanics*, 11:339–369.
- Gascard, J. and Clarke, R. A. (1983). The formation of Labrador Sea water. part II: Mesoscale and smaller-scale processes. *Journal of Physical Oceanography*, 13:1779–1797.
- Gregg, M. C. and Kunze, E. (1991). Shear and strain in Santa Monica Basin. *Journal of Geophysical Research*, 96(C9):16,709–16,719.
- Hakkinen, S., Hatun, H., and Rhines, P. B. (2008). Satellite evidence of change in the northern gyre. In Dickson, R. R., Meincke, J., and Rhines, P., editors, *Arctic-Subarctic Ocean Fluxes: Defining the Role of the Northern Seas in Climate*, pages 613–628. Springer.
- Hakkinen, S. and Rhines, P. B. (2004). Decline of subpolar North Atlantic circulation during the 1990s. *Science*, 304:555–559.
- Hanna, E., Huybrechts, P., Steffen, K., Cappelen, J., Huff, R., Shuman, C., Irvine-Fynn, T., Wise, S., and Griffiths, M. (2008). Increased runoff from melt from the Greenland ice sheet: A response to global warming. *Journal of Climate*, pages 331–341.
- Harcourt, R. R., Steffen, E. L., Garwood, R. W., and D’Asaro, E. A. (2002). Fully Lagrangian floats in Labrador Sea deep convection: Comparison of numerical and experimental results. *Journal of Physical Oceanography*, 32:493–510.
- Hátún, H., Eriksen, C. C., and Rhines, P. B. (2007). Buoyant eddies entering the Labrador Sea observed with gliders and altimetry. *Journal of Physical Oceanography*, 37:2838–2854.
- Head, E. J. H., Harris, L. R., and Campbell, R. W. (2000). Investigations on the ecology of *Calanus* spp. in the Labrador Sea. I: Relationship between the phytoplankton bloom and reproduction and development of *Calanus finmarchicus* in spring. *Marine Ecology Progress Series*, 193:53–73.
- Head, E. J. H., Harris, L. R., and Yashayaev, I. (2003). Distributions of *Calanus* spp. and other mesozooplankton in the Labrador Sea in relation to hydrography in spring and summer (1995–2000). *Progress in Oceanography*, 59:1–30.

- Henson, S. A., Robinson, I., Allen, J. T., and Waniek, J. J. (2006). Effect of meteorological conditions on interannual variability in timing and magnitude of the spring bloom in the Irminger Basin, North Atlantic. *Deep Sea Research I*, 53:1601–1615.
- Holland, D. M., Thomas, R. H., de Young, B., Ribergaard, M. H., and Lyberth, B. (2008). Acceleration of Jakobshavn Isbræ triggered by warm subsurface ocean waters. *Nature Geoscience*, 1:659–664.
- Holliday, N. P., Waniek, J. J., Davidson, R., Wilson, D., Brown, L., Sanders, R., Pollard, R. T., and Allen, J. T. (2006). Large-scale physical controls on phytoplankton growth in the Irminger Sea part I: Hydrographic zones, mixing and stratification. *Journal of Marine Systems*, 59:201–218.
- Hubbard, R. M. (1980). Hydrodynamics technology for an Advanced Expendable Mobile Target (AEMT). Technical Report APL-UW 8013, Applied Physics Laboratory, University of Washington.
- Jones, H. and Marshall, J. (1993). Convection with rotation in a neutral ocean: A study of open-ocean convection. *Journal of Physical Oceanography*, 23:1009–1039.
- Klein, P. and Lapeyre, G. (2009). The oceanic vertical pump induced by mesoscale and submesoscale turbulence. *Annual Reviews of Marine Science*, 1:351–375.
- Körtzinger, A., Send, U., Wallace, D. W. R., Karstensen, J., and DeGrandpre, M. (2008). Seasonal cycle of O₂ and pCO₂ in the central Labrador Sea: Atmospheric, biological and physical implications. *Global Biogeochemical Cycles*, 22(GB1014).
- Laidre, K. L., Heide-Jorgensen, M. P., and Nielsen, T. G. (2007). Role of the bowhead whale as a predator in west Greenland. *Marine Ecology Progress Series*, 346:285–297.
- Laidre, K. L., Heide-Jorgensen, M. P., Nyeland, J., Mosbech, A., and Boertmann, D. (2008). Latitudinal gradients in sea ice and primary production determine Arctic seabird colony size in Greenland. *Proceedings of the Royal Society B*, 275:2695–2702.
- Lavender, K. L., Davis, R. E., and Owens, W. B. (2002). Observations of open-ocean deep convection in the Labrador Sea from subsurface floats. *Journal of Physical Oceanography*, 32:511–526.

- Lazier, J., Hendry, R., Clarke, A., Yashayaev, I., and Rhines, P. (2002). Convection and restratification in the Labrador Sea, 1990-2000. *Deep Sea Research*, 49(10):1819–1835.
- Legg, S. and McWilliams, J. C. (2002). Sampling characteristics from isobaric floats in a convective eddy field. *Journal of Physical Oceanography*, 32:527–544.
- Lévy, M. (2003). Mesoscale variability of phytoplankton and of new production: Impact of the large-scale nutrient distribution. *Journal of Geophysical Research*, 108:3358.
- Lévy, M. (2005). Nutrients in remote mode. *Nature*, 437:628–631.
- Lilly, J. M. and Rhines, P. B. (2002). Coherent eddies in the Labrador Sea observed from a mooring. *Journal of Physical Oceanography*, 32:585–598.
- Lilly, J. M., Rhines, P. B., Schott, F., Lavender, K., Lazier, J., Send, U., and D’Asaro, E. (2003). Observations of the Labrador Sea eddy field. *Progress in Oceanography*, 59:75–176.
- Longhurst, A. R. (2007). *Ecological Geography of the Sea*. Academic Press, Amsterdam, 2nd edition.
- Lueck, R. G. (1990). Thermal inertia of conductivity cells: Theory. *Journal of Atmospheric and Oceanic Technology*, 7:741–755.
- Lueck, R. G. and Picklo, J. J. (1990). Thermal inertia of conductivity cells: Observations with a sea-bird cell. *Journal of Atmospheric and Oceanic Technology*, 7:756–768.
- Luthcke, S. B., Zwally, H. J., Abdalati, W., Rowlands, D. D., Ray, R. D., Nerem, R. S., Lemoine, F. G., McCarthy, J. J., and Chinn, D. S. (2006). Recent Greenland ice mass loss by drainage system from satellite gravity observations. *Science*, pages 1286–1289.
- Lutz, V. A., Sathyendranath, S., Head, E. J. H., and Li, W. K. W. (2003). Variability in pigment composition and optical characteristics of phytoplankton in the Labrador Sea and the central North Atlantic. *Marine Ecology Progress Series*, 260:1–18.
- Mahadevan, A., Thomas, L., and Tandon, A. (2008). Technical comment: Eddy/wind interactions stimulate extraordinary mid-ocean plankton blooms. *Nature*, 320:448.

- Marshall, J. and Schott, F. (1999). Open-ocean convection: Observations, theory and models. *Reviews of Geophysics*, 37:1–64.
- Maximenko, N. A. and Niiler, P. P. (2004). Hybrid decade-mean global sea level with mesoscale resolution. In Saxena, N., editor, *Recent Advances in Marine Science and Technology*, pages 55–59, Honolulu. PACON International.
- Maxworthy, T. and Narimousa, S. (1994). Unsteady, turbulent convection into a homogeneous, rotating fluid, with oceanographic applications. *Journal of Physical Oceanography*, 24:865–887.
- McCartney, M. S. and Talley, L. D. (1982). The subpolar mode water of the North Atlantic Ocean. *Journal of Physical Oceanography*, 12:1169–1188.
- McGillicuddy, D. J., Anderson, L. A., Doney, S. C., and Maltrud, M. E. (2003). Eddy-driven sources and sinks of nutrients in the upper ocean: results from a 0.1 degree resolution model of the North Atlantic. *Global Biogeochemical Cycles*, 12.
- McGillicuddy, Jr., D. J., Anderson, L. A., Bates, N. R., Bibby, T., Buesseler, K. O., Carlson, C. A., Davis, C. S., Ewart, C., Falkowski, P. G., Goldthwait, S. A., Hansell, D. A., Jenkins, W. J., Johnson, R., Kosnyrev, V. K., Ledwell, J. R., Li, Q. P., Siegel, D. A., and Steinberg, D. K. (2007). Eddy/wind interactions stimulate extraordinary mid-ocean plankton blooms. *Nature*, 316:1021–1026.
- McGillicuddy, Jr., D. J., Robinson, A. R., Siegel, D. A., Jannasch, H. W., Johnson, R., Dickey, T. D., McNeil, J., Michaels, A. F., and Knap, A. H. (1998). Influence of mesoscale eddies on new production in the Sargasso Sea. *Letters to Nature*, 394:263–266.
- Mertz, G., Narayanan, S., and Helbig, J. (1993). The freshwater transport of the Labrador Current. *Atmosphere-Ocean*, 31(2):281–295.
- Miller, C. B. (2004). *Biological Oceanography*. Blackwell Publishing, Malden, MA.
- Munk, W. H. (1981). Internal waves and small-scale processes. *Evolution of Physical Oceanography, Scientific Surveys in Honor of Henry Stommel*, pages 264–291.

- Nicholson, D., Emerson, S., and Eriksen, C. C. (2008). Net community production in the deep euphotic zone of the subtropical North Pacific gyre from glider surveys. *Limnology and Oceanography*, 53:2226–2236.
- Niiler, P. P., Maximenko, N. A., and McWilliams, J. C. (2003). Dynamically balanced absolute sea level of the global ocean derived from near-surface velocity observations. *Geophysical Research Letters*, 30(22):2164.
- Perry, M. J., Sackmann, B. S., Eriksen, C. C., and Lee, C. M. (2008). Seaglider observations of blooms and subsurface chlorophyll maxima off the Washington coast. *Limnology and Oceanography*, pages 2169–2179.
- Pickart, R. S., Torres, D. J., and Clarke, R. A. (2002). Hydrography of the Labrador Sea during active convection. *Journal of Physical Oceanography*, 32:428–457.
- Prater, M. D. (2002). Eddies in the Labrador Sea as observed by profiling RAFOS floats and remote sensing. *Journal of Physical Oceanography*, 32:411–427.
- Preisendorfer, R. W. and Mobley, C. D. (1988). *Principal component analysis in meteorology and oceanography*. Elsevier, New York, NY, USA.
- Renfrew, I. A., Moore, G. W. K., Guest, P. S., and Bumke, K. (2002). Comparison of surface layer and surface turbulent flux observations over the Labrador Sea with ECMWF analyses and NCEP reanalyses. *Journal of Physical Oceanography*, 32:383–400.
- Ryan, J. P., McManus, M. A., Paduan, J. D., and Chavez, F. P. (2008). Phytoplankton thin layers caused by shear in frontal zones of a coastal upwelling system. *Marine Ecology Progress Series*, 354:21–34.
- Rykova, T. (2006). Evolution of the Irminger Current Anticyclones in the Labrador Sea from hydrographic data. Master's thesis, Massachusetts Institute of Technology and Woods Hole Oceanographic Institution, Woods Hole, MA.
- Sackmann, B. S. (2007). *Remote Assessment of 4-D phytoplankton distributions off the Washington Coast*. Doctor of philosophy, University of Maine, Orono, Maine.

- Sackmann, B. S., Perry, M. J., and Eriksen, C. C. (2008). Seaglider observations of variability in daytime fluorescence quenching of chlorophyll-*a* in Northeastern Pacific coastal waters *submitted. Biogeosciences*.
- Sathiyamoorthy, S. and Moore, G. W. K. (2002). Buoyancy flux at Ocean Weather Station Bravo. *Journal of Physical Oceanography*, 32:458–474.
- Siegel, D. A., Doney, S. C., and Yoder, J. A. (2002). The North Atlantic spring phytoplankton bloom and Sverdrup's critical depth hypothesis. *Science*, 296:730–733.
- Siegel, D. A., McGillicuddy, Jr., D. J., and Fields, E. A. (1999). Mesoscale eddies, satellite altimetry and new production in the Sargasso Sea. *Journal of Geophysical Research*, 104(C6):13,359–13,379.
- Spall, S. A. and Richards, K. J. (2000). A numerical model of mesoscale frontal instabilities and plankton dynamics – I. Model formulation and initial experiments. *Deep Sea Research*, 47:1261–1301.
- Stacey, M. T., McManus, M. A., and Steinbeck, J. V. (2007). Convergences and divergences and thin layer formation and maintenance. *Limnology and Oceanography*, 52:1523–1532.
- Stearns, L. A. and Hamilton, G. S. (2007). Rapid volume loss from two East Greenland outlet glaciers quantified using repeat stereo satellite imagery. *Geophysical Research Letters*, 34.
- Steffen, E. L. and D'Asaro, E. A. (2002). Deep convection in the Labrador Sea as observed by Lagrangian floats. *Journal of Physical Oceanography*, 32:475–492.
- Straneo, F. and Saucier, F. (2008). The outflow from Hudson Strait and its contribution to the Labrador Current. *Deep Sea Research*, 55:926–946.
- Sverdrup, H. U. (1953). On conditions for the vernal blooming of phytoplankton. *J. Cons. Int. Explor.*, 18:287–295.
- Tang, C. C. L., Ross, C. K., Yao, T., Petrie, B., DeTracey, B. M., and Dunlap, E. (2004). The circulation, watermasses and sea-ice of Baffin Bay. *Progress in Oceanography*, 63:183–228.

- Townsend, D. W., Cammen, L. M., Holligan, P. M., Campbell, D. E., and Pettigrew, N. R. (1994). Causes and consequences of variability in the timing of spring phytoplankton blooms. *Deep Sea Research*, 41:747–765.
- Väge, K., Pickart, R. S., Thierry, V., Reverdin, G., Lee, C. M., Petrie, B., Agnew, T. A., Wong, A., and Ribergaard, M. H. (2009). Surprising return of deep convection to the subpolar North Atlantic Ocean in winter 2007-2008. *Nature Geoscience*, 2:67–72.
- Waniek, J. J., Holliday, N. P., Davidson, R., Brown, L., and Henson, S. A. (2005). Freshwater control of onset and species composition of Greenland shelf spring bloom. *Marine Ecology Progress Series*, 288:45–57.
- Wentz, F. and Meissner, T. (2004). AMSR-E/Aqua L2B global swath ocean products derived from Wentz algorithm V002 for 2005. *Boulder, Colorado USA: National Snow and Ice Data Center. Digital media.*
- Wu, Y., Platt, T., Tang, C. C. L., and Sathyendranath, S. (2008). Regional differences in the timing of the spring bloom in the Labrador Sea. *Marine Ecology Progress Series*, 355:9–20.
- Yashayaev, I. (2007). Hydrographic changes in the Labrador Sea, 1960-2005. *Progress in Oceanography*, 73:242–276.
- Yashayaev, I. and Loder, J. W. (2009). Enhanced production of Labrador Sea Water in 2008. *Geophysical Research Letters*, 36.
- Yu, L. and Weller, R. A. (2007). Objectively Analyzed air-sea heat Fluxes (OAFlux) for the global oceans. *Bulletin of the American Meteorological Society*, 88:527–539.